Title
Ion-Water Interactions of Solvated Multiply Charged Anions and Their Effects on the Extended Hydrogen-Bonding Network of Water Molecules

Author
DiTucci, Matthew John

Publication Date
2017

Ion-Water Interactions of Solvated Multiply Charged Anions and Their Effects on the Extended Hydrogen-Bonding Network of Water Molecules

by

Matthew John DiTucci

A dissertation submitted in partial satisfaction of the

requirements for the degree of

Doctor of Philosophy

in

Chemistry

in the

Graduate Division

of the

University of California, Berkeley

Committee in charge:

Professor Evan R. Williams, Chair
Professor Kristie A. Boering
Professor Frances Hellman

Fall 2017

Ion-Water Interactions of Solvated Multiply Charged Anions and Their Effects on the Extended Hydrogen-Bonding Network of Water Molecules

Abstract

Ion-Water Interactions of Solvated Multiply Charged Anions and Their Effects on the Extended Hydrogen-Bonding Network of Water Molecules

by

Matthew John DiTucci

Doctor of Philosophy in Chemistry

University of California, Berkeley

Professor Evan R. Williams, Chair

Ion-water interactions have a large influence on the chemical and physical behavior of water and solutes in a diverse range of environments. These interactions play a role in atmospheric aerosols, desalination methods, enzymatic active sites, and ion stability. For example, multiply charged anions (MCAs), such as sulfate and phosphate, are ubiquitous in the condensed phases, but are intrinsically unstable once desolvated due to the lack of non-covalent interactions. Aqueous ion-containing nanodroplets formed *via* electrospray ionization can be investigated using high-resolution mass spectrometry. Utilizing the ability to store ion-containing droplets in the ion cell of a Fourier transform ion cyclotron resonance (FT-ICR) mass spectrometer, an ion with a discrete number of solvating water molecules can be mass-selected and thereafter probed using blackbody, infrared, and ultraviolet photons, or thermal electrons to measure its chemical and physical properties. Studying the stabilities of hexacyanoferrates as a function of $(H_2O)_n$, we find two hydration shells are required to stabilize $Fe(CN)_6^{4-}$ from spontaneous electron ejection. Although the ability of ions to influence water molecules remotely has been debated in condensed phase experiments, we provide unambiguous evidence for ion-water interactions leading to structural perturbations into a fourth solvation shell. Furthermore, evidence for remote *dynamic* perturbations in solutions is presented using a novel broadband terahertz spectroscopy technique. Although the nanodroplet experiments are performed in a temperature-regulated ion cell, a key question in the gas phase is *to what magnitude does evaporative cooling affect the internal temperature of an ion population?* Extensive master equation modeling to fit temperature-dependent blackbody dissociation kinetics reveals that, although the effect is minimal at low temperatures, evaporative cooling can lead to disparities of $\Delta T > 100$ K when storing nanodroplets in an ion cell above room temperature. These findings can be used to more accurately relate experimental nanodroplet studies to the ambient temperatures relevant to atmospheric aerosols and condensed-phase solutions. The research presented here provides unique molecular-level insight into ion-water interactions leading to stability in MCAs as well as remote structural and dynamic perturbations that extend beyond the inner solvation shell.

For Elle — my wife and continual inspiration.

Table of Contents

Acknowledgments

This dissertation is the cumulative product of support, guidance, patience, and an entire Escher's staircase worth of ineffable kindness, extended by the many individuals who have shared their time with me throughout these last five years. First and foremost, I would like to thank and acknowledge my advisor, Evan R. Williams, whose mentorship has allowed me to reach an exceedingly greater potential as a developing scientist. He has dedicated countless hours to improving my scientific writing, presentation skills, and honing my approach to critical thinking — each a valuable facet of scientific research that will remain with me throughout the entirety of my career. I have watched several others flourish in their pursuits as a result of his genuine desire to see us succeed and have experienced nothing less while striving to accomplish my own goals. As equals in importance, I would not have had these opportunities were it not for my loving parents, John DiTucci Jr. and Cynthia Louise DiTucci, who have taught me to always follow my passions and enjoyments in life, to be a leader when the opportunity presents itself, and to learn from others when their experience surpasses my own. Their patient wisdom and thoughtful advice allowed me to gain the formative tools required for pursuing academic studies, for which I will always be grateful. To my wife, Joelle Marie DiTucci, whom without I would have followed several other less fruitful paths in life: her bright and endless love has been the driving force for my greatest pursuits. She keeps my eyes on the future — always striving to improve myself to become a better person. I owe sincere thanks to each of my colleagues, labmates, and mentors who instilled a genuine culture of friendship throughout the lab and supplemented each morning's coffee with enough support and motivation to persevere even on the hardest days. Especially to Richard J. Cooper, who I have had the pleasure of sharing several projects with throughout my graduate career. Together, we overcame the most challenging situations I have encountered during my time in scientific research. He has undoubtedly assisted in shaping me as a productive scientist and will remain a cherished friend outside of the laboratory for many years to come. Recognition is also due to several close lifelong friends who have cheered me on throughout my academic career - notably to Clint Wilson, who played a pivotal role in my decision to pursue science. In my move to California for graduate studies, his was the last familiar face that wished me well, following his support in the long journey from the Keystone to the Indian Rock. Finally, I would like to thank my committee members, Prof. Kristie Boering and Prof. Frances Hellman, for their generous time and assistance. To each of you: thank you for choosing to be a part of my life, for being a foothold throughout a difficult journey upward, and for sharing your knowledge with me — so that I can share mine here.

Chapter 1

Introduction

1.1 An Isolation-Based Approach to the Solution

1.1.1 Motivation

The fundamental properties and characteristics of macroscopic systems can often be explained by composite interactions at the molecular level. In this regard, Aristotle's *"The whole is greater than the sum of its parts"* is less philosophical than it is a scientifically accurate theorem. For indeed, the physical and chemical properties of a wide range of systems from biological cells to synthetic membranes are not dependent on only their molecular compositions, but rather the rich non-covalent chemistry that exists between atoms, molecules, and their surroundings.[1–4] Non-covalent interactions include Van der Waals, electrostatic, and, of primary interest within this collection of research, the hydrogen bond. Each of these interactions are typically weaker than covalent bonds, which are responsible for providing the intramolecular framework within molecules. However, the sum of several individual non-covalent interactions throughout a system is responsible for many of life's most basic characteristics and phenomena that are often taken for granted, such as the liquid state of water at room temperature, the formation of sedimentary rocks *via* mineral precipitation, and even the double helical structure of our genetic codes through nucleic acid pairing.

As a further example, non-covalent molecule-water, ion-water, and ion-molecule interactions can influence the tertiary structure of enzymes.[5,6] Enzyme activities are commonly optimized in aqueous solutions, where enzymes fold hydrophobic moieties into their interior and expose hydrophilic groups on the exterior, due to their ability to favorably hydrogen bond with water molecules. These structures can be significantly modified when interacting with non-aqueous solvents, which typically lead to an alteration in the lowest-energy tertiary structure of the enzyme. This can disrupt active sites and therefore impede the ability of enzymes to bind substrate molecules. For example, transesterification reactions catalyzed by the enzyme α-chymotrypsin are $\sim 10^5$ times less efficient in non-aqueous solutions as a result of conformational changes.[7] The presence of ions in solution can also drive conformational changes,[8] *e.g.*, the common use of some guanidinium salts as denaturants.[9,10]

Ions influence structural changes through either direct non-covalent interaction with the protein backbone and residues, or *via* perturbations to the hydrogen-bonding network of water.[11] The extent to which an ion can either perturb or stabilize the enzymatic structure has been ranked in the eponymously named Hofmeister series, which was conceived by ordering salts based on their propensity to precipitate egg white albumin from bulk aqueous solutions.[12] Despite its introduction in 1888, the degree to which ion-water and ion-molecule interactions contribute to the ordering in both the anionic and cationic series, as well as the intrinsic propensity for an ion to structure water molecules beyond its inner solvation shell, is still debated.[13–16] Therefore, it is important to dedicate efforts into understanding more about fundamental non-covalent interactions and how they can lead to observed physical and chemical properties. Herein, this dissertation will focus on ion-water interactions in order to understand how hydrogen bonding can influence solvated ions and likewise, how ions can influence the extended hydrogen-bonding network of water.

1.1.2 Traditional Methods

Common solution-phase techniques for elucidating ion-water interactions include neutron and x-ray diffraction,[17–22] as well as various spectroscopies including infrared,[23–27] terahertz,[28–30] nuclear magnetic resonance (NMR),[31–34] and dielectric relaxation (DRS).[35–37] Computational methods, such as *ab initio* calculations and molecular dynamics, have also provided unique molecular-level insight.[38–41] Each technique has its own unique strengths and weaknesses. For instance, diffraction methods rely on the correlation functions, $g_{OO}(r)$, $g_{OH}(r)$, and $g_{HH}(r)$, for oxygen-oxygen, oxygen-hydrogen, and hydrogen-hydrogen distances, respectively, in bulk solutions. These values provide useful information for nearest-neighbor water molecules. This is especially effective for measuring the coordination number of water molecules surrounding ions,[17,18] and for observing local structural changes during phase transitions as a function of temperature.[19] However, the hydrogen-bonding network beyond the coordination shell is less homogenous and results in a severe broadening of diffraction-based peaks corresponding to the second hydration shell and beyond. This makes probing solvation beyond *local* interactions challenging for diffraction methods, which are more suited for investigating the inner coordination shell.

Spectroscopic methods cover a wide range of techniques for probing the structure and dynamics of aqueous solutions. For example, time-resolved setups take advantage of the >100 fs time scale for dissipation and transfer of energy absorbed from an initial pulse laser. A subsequent probe laser provides temporal information regarding the relaxation dynamics of water molecules, which are highly dependent on the surrounding environment. Using femtosecond-IR, Bakker *et al.* have concluded that cations primarily influence the dipole orientation of water molecules, whereas anions perturb the available orientations of water molecule hydroxyl groups.[23] In Chapter 6, results of modern terahertz techniques are discussed and provide evidence for long-distance perturbations to water molecule dynamics by multivalent hexacyanoferrates, $Fe(CN)_6^{4-}$ and $Fe(CN)_6^{3-}$.[28] Spectroscopic techniques often require high solute concentrations ($\sim 1-6$ M) in order to measure sufficient absorption. This results in a high abundance of counterions, which complicate the ability to probe specific ion-water interactions from a single ion. Furthermore, the high solute concentrations lead to very sparse *bulk-like* water molecules remaining in solution. For instance, considering the concentration of bulk water is $\sim$55 M, an aqueous solution containing 3M of $Mg(ClO)_2$ will stoichiometrically contain three Mg^{2+} cations and six ClO^- anions for every fifty-five water molecules. If we assume an ideal solution with no ion-ion interactions, this leaves only ∼6 water molecules available for each ion. As a result, there is little opportunity for understanding how ions can influence remote water molecules in extended solvation shells with traditional spectroscopic techniques in the solution phase.

1.1.3 Ion-Containing Nanodroplets

An alternative approach to the conventional methods for investigating ion-water interactions is through the use of ion-containing nanodroplets. Isolated supramolecular ion-water complexes have the advantage of solvating a singular ion with a discrete number of water molecules, $M^{\pm}(H_2O)_n$, where M is an anion, cation, or charged ion pair and n is the number of water molecules solvating the ion. This allows for investigation of microsolvation by only a few water molecules to explore the direct coordination of sequential hydrates around the ion, or extensively hydrated droplets containing hundreds of water molecules, which can reveal remote interactions between the ion and surface up to nanometer distances. Studying ion-water interactions in droplets also removes the complication of counterions, which obfuscate the opportunity to measure discrete influences by a singular ion to remote water molecules. Because there is no defined limit to the number of water molecules that can solvate a single ion, aqueous nanodroplets can be used to study ion concentrations to a hypothetical infinite dilution. For example, a droplet consisting of fifty-five water molecules and a single monovalent ion is ∼500 mM in effective concentration, because one-hundred and ten water molecules would be required in bulk solution to generate a similar environment with an equally solvated counterion. Likewise, a trivalent ion in a five-hundred and fifty water molecule droplet has an effective concentration of ∼25 mM with respect to bulk. Accordingly, aqueous nanodroplets can overcome many of the shortcomings for studying ion-water interactions in the solution phase. These complexes provide a unique opportunity for answering challenging questions concerning the fundamental non-covalent influences with molecular level insight.

Nano-electrospray ionization (nESI) of aqueous salt solutions with concentrations in the range of $1-5$ mM can produce sub-nanometer to nanometer sized droplets containing the ions of interest, $M^{\pm}(H_2O)_n$. Individual ion-containing nanodroplets can be resolved by utilizing the mass-to-charge dependence of mass spectrometers, *e.g.* linear quadrupoles,[42,43] time-of-flight (TOF),[44,45] and Fourier transform ion cyclotron resonance (FT-ICR) instruments.[46–48] High resolution spectrometers are ideal for studying nanodroplets because nESI can generate several hundreds of hydration sizes for multiple species. For example, as we will see in Chapter 3, nESI of 5 mM potassium ferrocyanide, $K_4Fe(CN)_6$, produces more than four thousand unique nanodroplets between $\sim 50-1500$ m/z.[49] The nESI distribution includes multiple hydration sizes of $Fe(CN)_6^{4-}$, $Fe(CN)_6^{3-}$, $Fe(CN)_6^{2-}$, both protonated and potassiated ion-pairs for each of these multivalent ions, and isotopic distributions for each species. Utilizing the ability to spatially confine and trap ions for extended periods of time in an FT-ICR trap, ion-containing droplets can be probed using a variety of methods including photodissociation by blackbody photons,[50–52] infrared photons,[53–57] ultraviolet photons,[58,59] and also charge reduction by capture of thermal electrons.[60,61] A subset of these probes has led to the unique investigation of thermodynamic stability (Chapter 2), nanodroplet structure (Chapters 2, 3 & 4), and dissociation kinetics (Chapter 5).

1.2 Chemical Stability in Multiply Charged Anions

1.2.1 The Repulsive Coulomb Barrier

Despite their ubiquitous presence in nature, *small* multiply charged anions (MCAs), which can be roughly defined as less than ~7 Å in diameter, are intrinsically unstable owing to the large intramolecular electron-electron repulsions between their excess charges.[62,63] In the condensed phases, these anions can be stabilized through interactions with either counterions or solvent molecules. As an example, the sulfate dianion, SO_4^{2-}, is found widely in global seawaters, fertilizers, batteries, architectural plasters, and a wide range of other natural minerals. However, when isolated from any stabilizing non-covalent interactions, SO_4^{2-} dissociates *via* electron ejection with a calculated lifetime of only 1.6×10^{-10} s.[64] An early report in the 1990's by Compton *et al.* on the stability of gas-phase $^{-}C{-}(C)_n{-}C^{-}$ dianions as a function of chain length, n, spurred interest into further understanding the underlying chemical physics of MCAs.[65] This study found C_7^{2-} was the smallest dianionic carbon chain observed in the gas phase and concluded that the ~6.5 Å end-to-end distance in C_6^{2-} must lead to Coulombic repulsion greater than the second electron affinity. Later theoretical studies by Dreuw and Cederbaum provided valuable insight into the repulsive Coulomb barrier (RCB), which determines the energy required for electron detachment from MCAs (analogous to the barrier for emission of α particles from radioactive species).[66] The RCB emerges as a combination of potentials for long range electron-electron repulsion and short range electron-nucleus attraction and is highly dependent on both the size and charge state of the MCA. As the separation between charges increases, the height of the RCB decreases as a result of the diminished electrostatic repulsion, but the electron affinity of the system is simultaneously increased and leads to an overall greater stability.

Wang and coworkers have performed photoelectron spectroscopy (PES) measurements that resulted in an experimental probe of the RCB.[67] These measurements revealed that although the adiabatic binding energy for the second electron is ~1 eV for the citrate dianion, $C_6H_8O_7^{2-}$, absorption of 532 nm photons (2.33 eV) do not result in any observable electron detachment. They concluded that this is a direct result of the RCB height, which was subsequently calculated to be ~2.5 eV, in agreement with their experimental interpretation. Furthermore, calculations using the modeled RCB in $^{-}C{-}(C)_n{-}C^{-}$ result in an expected lifetime of 1.7×10^{-9} s for C_6^{2-}, with respect to electron loss, in agreement with its absence in previous mass spectrometry experiments, which had a detection time of ~10 µs.[65,66] This intrinsic lifetime increases significantly with respect to the chain length. For example, C_8^{2-} has a calculated lifetime of 2×10^{11} s. Accordingly, many large MCAs, such as proteins, carbohydrates, DNA, or other large molecules, are stable because of adequate separation between their excess charges,[68–71] but small MCAs require stabilization gained through non-covalent interactions with counterions or solvent molecules.[72–76]

1.2.2 Critical Cluster Sizes

Investigating the fundamental ion-water interactions that lead to MCA stabilities can increase our understanding of how solvent increases the barrier to electron detachment or charge separation. Gas-phase nanodroplets are well-suited to revealing this information because the ion-containing clusters can be studied as a function of hydration, *e.g.*, the lowest $(H_2O)_n$ hydrate measured by mass spectrometry can reveal the onset of instability. However, this was once a challenging endeavor as an ironic consequence of the intrinsic instability of bare MCAs, which prevented the use of solvent condensation methods, *i.e.*, sequential addition of water molecules to a bare anion. With the development of electrospray ionization by Fenn in the early 1980s,[77,78] ion-containing nanodroplets could be readily generated directly from aqueous solutions. Using this ionization method, numerous experiments have now been performed to elucidate solvent effects on the chemical physics of MCA stabilities. For instance, the height of the RCB in the oxalate dianion, $C_2O_4^{2-}$, was studied with PES as a function of aqueous hydration, $(H_2O)_n$.[79] Hydrates as low as $n = 3$ were observed by mass spectrometry, suggesting that a minimum of three water molecules are required for thermodynamic stability to electron loss. The height of the RCB decreases from 3.5 eV at $n = 3$ to 1.8 eV at $n = 20$, analogous to the behavior that was calculated when extending the distance between excess charges in $^{-}C{-}(C)_n{-}C^{-}$. In aqueous nanodroplets, the Coulomb repulsion is therefore reduced through strong hydrogen-bonds that form between the MCA and water molecules and also dielectric shielding afforded by solvation.[80]

A minimum number of water molecules are required to stabilize small MCAs, as observed for $C_2O_4^{2-}(H_2O)_n$ with $n = 3$.[79] A critical cluster size, n_c, defined as *"the hydrate size at which charge separation is energetically favored over the loss of one water molecule"*, has been studied extensively for the hydrated sulfate dianion, $SO_4^{2-}(H_2O)_n$.[43,80–83] Utilizing the potential to store ions for an extended period of time in an FT-ICR ion cell, a single hydration size can be isolated and allowed to slowly dissociate *via* absorption of low energy blackbody photons originating from the instrument walls. This technique is commonly referred to as blackbody infrared radiative dissociation, or BIRD.[50] Water molecule loss is the only available dissociation pathway for $SO_4^{2-}(H_2O)_n$ with $n \geq 7$.[82] However, BIRD of $n = 3-6$ results in charge separation to form $HSO_4^{-}(H_2O)_{n-k-1}$ and $OH^{-}(H_2O)_k$ in addition to the water loss dissociation channel. Water molecule loss makes up >90 % of dissociation products from $n = 6$, but is much less favorable at <10 % from $n = 5$. Therefore, the critical cluster size for SO_4^{2-} is $n_c = 5$. Although no hydrates below $n = 3$ were observed in these experiments, Blades and Kebarle have reported formation of $n = 2$ by collisional dissociation of larger SO_4^{2-} hydrates.[84] These results illustrate that the observed dissociation channels are dependent on the energy imparted by the excitation method and that higher energy techniques can form lower n products as a result of the entropically favored loss of a water molecule. In Chapters 2 & 3, we will discuss the stabilities of tri- and tetravalent hexacyanoferrate anions, $Fe(CN)_6^{3-}$ and $Fe(CN)_6^{4-}$, which are the smallest, highest charge density anions that have been successfully observed in the gas phase by mass spectrometry.[49,85] These MCAs require solvation by $n > 8$ and $n > 40$, respectively, for thermodynamic stability to electron ejection. From these data, we show solvation beyond the inner coordination shell is required for stability in $\mathrm{Fe(CN)}_6^{4-}$, which provides direct evidence for *remote* ion-water interactions required for sufficient electron delocalization and shielding of the excess charges.

1.3 Probing the Structure of Aqueous Solvation

1.3.1 Infrared Photodissociation

Whereas the human eye is adept in visible spectroscopy, we rely on the absorption of infrared photons through vibrational excitation to "visualize" the structure of molecules and their surrounding environments. There are numerous challenges to probing the structure of gas-phase ions with spectroscopic methods.[86,87] Most prominently, traditional condensed-phase techniques rely on beam attenuation as expressed by the Beer-Lambert Law:

$$I(\nu) = I_0(\nu) \cdot e^{-\sigma \cdot n \cdot l} \qquad \text{(Equation 1.1)}$$

where $I_0(\nu)$ is the intensity of the beam in vacuum and $I(\nu)$ is the intensity of the beam after passing through a sample with absorption cross section, σ, and number density, n, across a beam-sample interaction length, l. Attainable number densities using mass spectrometric methods are $\sim 10^8$ ions/cm^3 as a result of the space charge effects between ions.[88] Using expected values for σ, n, and l in gas-phase experiments leads to an attenuation, $1 - I(\nu)/I_0(\nu)$, of only $\sim 10^{-9}$ and therefore, this method is not suitable for measuring the absorption of infrared photons by aqueous nanodroplets. A considerable increase in the value of l, and therefore the overall attenuation, can be achieved using cavity ringdown spectroscopy.[89,90] This method entails measuring a decay constant for the intensity of radiation passing through highly reflective mirrors ($R \simeq 0.9999$), which induce multiple photon passes through the sample. Alternatively, an infrared photodissociation (IRPD) approach can be employed for gas-phase ions, whereby the absorption of tunable infrared photons results in measurable dissociation of a mass-selected precursor ion. A first-order frequency dependent rate constant can be derived using abundances of the precursor and product ions after irradiation. Photodissociation rates, k_{IRPD}, are corrected for frequency dependent variations in laser power, $P(\nu)$, along with the rate of dissociation due to blackbody photons, k_{BIRD}, as expressed below:

$$k_{IRPD}(\nu) = -ln\left[\frac{A_{Prec,t}}{A_{Prec,t} + (\sum_{i=1}^{n} A_{Prod,i,t})}\right] \cdot \frac{1}{t \cdot P(\nu)} - k_{BIRD} \qquad \text{(Equation 1.2)}$$

where $A_{Prec,t}$ is the abundance of the precursor after total irradiation time, t, and $A_{Prod,i,t}$ is the abundance of the i^{th} product from a total number of products, n. This method has the unique advantage of being independent of variability in precursor signal from scan to scan because the rates are measured using a relative relationship of the abundances. Depletion of the precursor is proportional to both the cross-section of absorption and intensity of the beam for a given wavelength. Therefore, a gas-phase infrared spectrum in the vibrational region of interest can be generated by plotting k_{IRPD} as a function of wavelength.[91]

The relation of k_{IRPD} to beam intensity naturally requires a radiation source that can produce sufficient power output to induce dissociation above background depletion due to BIRD. The lack of accessible high-powered lasers at the onset of studies utilizing IRPD for the region between ∼2800 − 4000 cm^{-1}, corresponding to N–H, C–H, and O–H stretches, led to the use of "tagging" cold ions with messenger species, including H_2, He, and Ar, which have low thresholds for dissociation from the complex.[92] These methods take advantage of intramolecular vibrational redistribution (IVR), whereby the energy absorbed from an excited oscillator is partitioned throughout the complex until a reactive mode is found, *e.g.*, the non-covalently bound tags. In this way, absorption originating from the molecule of interest can be observed as photodissociation of the tagging atom or molecule. Limitations in power output have since been overcome by the construction of free electron laser user facilities, including the Free Electron Laser for Infrared eXperiments (FELIX) and Centre Infrarouge Laser Orsay (CLIO), and more recently, the availability and affordability of tunable bench top infrared systems. A neodymium-doped yttrium aluminum garnet (Nd:YAG) pumped laser outputting 1064 nm photons can be coupled with commercial optimal parametric oscillator and amplifier systems (OPO/OPA) that generate tunable infrared radiation between ∼2800 − 4000 cm^{-1}. These systems are capable of generating power outputs of ∼10 − 50 mW, which is sufficient for inducing facile evaporation of water molecules from aqueous nanodroplets well above background dissociation due to BIRD and have been implemented in several laboratories worldwide. Since its introduction as a valuable tool for elucidating structure, IRPD has been used to investigate a broad range of species, including small organic molecules,[93,94] metal complexes,[95,96] amino acids,[46,97] peptides,[98,99] and of most interest to the collection of work presented here, ion-containing nanodroplets.[42–44,46–49,53,54,57,85,88,91,100–104]

1.3.2 Microsolvation Studies

One of the most widespread uses of IRPD for solvated ions in the gas phase has been investigating microsolvated structures ($n \leq \sim 25$) using the region between ∼2800 − 4000 cm^{-1}, which includes photon absorption by the O–H oscillators of solvating water molecules. The vibrational frequencies of water molecules are extremely sensitive to their surrounding environments, *e.g.*, increased hydrogen bonding partners generally lead to a red shift in the frequency of the O–H vibration. Consequently, it is possible to resolve the absorption by a water molecule that accepts one and donates one hydrogen bond (**AD** bonding motif, where **A** = *acceptor* and **D** = *donor*) versus a separate water molecule that accepts an additional hydrogen bond (**AAD**). Microsolvation studies are often coupled with *ab initio* calculations for comparing the harmonic spectra of potential low-energy isomers to measured IRPD spectra. For example, Lisy *et al.* have studied the competition between forming ion-water or water-water hydrogen bonds with hydrated monovalent ions, $M^+(H_2O)_n$ where M = Li, Na, K, and Cs between $n = 2 - 5$.[42] The IRPD spectra for $n = 2$ indicate that there are no hydrogen-bonded O–H stretches and therefore, each of the water molecules interact only with the metal ion. With $n = 3$, a strong band near ∼3520 cm^{-1} from a bonded O–H indicates water-water interactions between water molecules in the first solvation shell are favored over only interactions with Cs^+, which has the largest radius and lowest charge density compared to Li^+, Na^+, and K^+. The water-water hydrogen bonding motif is consistent with calculated harmonic spectra for the lowest energy $Cs^+(H_2O)_3$ isomer. These results illustrate how probing small microsolvated clusters can provide detailed, molecular-level structural information, which is exceedingly more difficult to measure in bulk solutions as a result of counterion influences. Other microsolvation studies have investigated the first shell coordination number of various ions,[105,106] preferred water molecule binding sites in amino acids,[97] formation of cage-like clathrate structures around small ions,[107–109] and insight into the denaturing mechanism of the guanidinium ion.[100,101] In Chapter 2, we will discuss the microsolvation of $Fe(CN)_6^{3-}(H_2O)_8$ in order to reveal structural motifs leading to thermodynamic stability of the trianion with respect to spontaneous electron ejection.[85] In comparison with calculated structures, we conclude that all eight water molecules reside in the first solvation shell of $Fe(CN)_6^{3-}$. Furthermore, structures that maximize the number of hydrogen bonds to cyano ligands are the lowest energy isomers and have calculated vibrational frequencies that are in agreement with the experimentally measured IRPD spectra.

1.3.3 Long Distance Interactions

IRPD in the O–H oscillator region between $\sim 2800 - 4000$ cm^{-1} is capable of revealing surface-sensitive information for aqueous nanodroplets, analogous to the use of vibrational sum frequency generation (SFG) spectroscopy to probe condensed-phase surfaces.[110–112] Although surface information is lost using non-SFG methods in the condensed phase, due to the scant number of water molecules at the surface with respect to bulk, the ratio of surface area to volume in nanometer-sized nanodroplets is significantly larger than in solution. This allows for adequate sensitivity between absorption from water molecules at the surface versus the interior. For instance, water molecules at the surface of nanodroplets with at least one "free" O–H, which face outward and away from the droplet and do not participate in hydrogen bonding (**AA**, **AD** or **AAD**), have a unique infrared absorption near ∼3700 cm^{-1}. Conversely, interior water molecules donating both hydrogen atoms to either adjacent water molecules or directly to the solvated ion (**DD**, **ADD**, or **AADD**), absorb photons between $\sim 2800 - 3650$ cm^{-1}. Both neutral and cation-containing droplets have a measurable free O–H band beginning at the onset of solvation. In anion-containing droplets, however, water molecules in the first coordination shell form optimal ion-water hydrogen bonds and orient with their partially positive-charged hydrogen atoms toward the negative charge of the anion. As a result, a persisting free O–H band in anionic droplets is absent until sufficient shielding by additional water molecules can overcome the strong Coulombic interaction so that water molecules at the surface can orient as they would most favorably in neutral and cationic droplets. The appearance of the free O–H band for anionic nanodroplets can therefore be used as an indication for the onset of diminished ion-water interactions. Using the density of water to approximate the radius of a discrete hydration size, the distal extent of ion-water interactions between the solvated anion and surface can be calculated.

IRPD measurements of $SO_4^{2-}(H_2O)_n$ between $n = 36 - 80$ do not contain a free O–H until $n > 43$, where a band begins to emerge at ∼3710 cm^{-1}.[104] This corresponds to an ion-water interaction distance of ∼0.68 nm, where structural perturbations at the surface resulting from the anionic charge begin to subside. Evidence for structural interactions to even further distances has been presented by comparing the bonded O–H regions of $SO_4^{2-}(H_2O)_n$ and $Ca^{2+}(H_2O)_n$ with $n = 250$.[113] Markedly different absorptions in the region between ∼2800 − 3650 cm^{-1} for the two ion-containing nanodroplets suggest that structural differences, as a result of effects originating from the solvated ions, are still present well beyond the second solvation shell. Long distance perturbations have also been observed through freezing point depression of nanodroplets containing La^{3+}, which offsets the transition of amorphous or "liquid-like" hydrogen bonding to tetragonally oriented crystalline ice by ∼100 water molecules with respect to neutral droplets.[114,115] In Chapters 2, 3, & 4, we explore the extent of water molecule patterning by $Fe(CN)_6^{3-}$ and $Fe(CN)_6^{4-}$, and also introduce temperature-dependent experiments for patterning by SO_4^{2-}.[49,85] Despite condensed-phase experiments that have suggested ions pattern water molecules only locally,[116] we conclude that $Fe(CN)_6^{4-}$ patterns water molecules to at least ∼1 nm from the anion into a fourth solvation shell. Furthermore, we find structural orientation of water molecules at the surface of $SO_4^{2-}(H_2O)_n$ with $n = 30$ can persist up to temperatures relevant to atmospheric aerosols. Moreover, these results provide useful insight into the molecular origins of Hofmeister effects.

1.4 Ion Temperatures at the Zero-Pressure Limit

The low-pressure conditions commonly used for storing and investigating non-covalent complexes in the gas phase result in rapid evaporative cooling of thermal ion distributions, which complicates the ability to determine ion effective temperatures. This introduces considerable uncertainty to the interpretation of temperature-dependent data and therefore, necessitates a means for calculating the internal energies of these ions. To elaborate, vacuum chambers with pressures below ∼10^{-8} Torr, referred to as the *zero-pressure limit*, have a low concentration of background gas and consequently, slow ion-neutral collision rates with respect to radiative emission events, *i.e.*, $k_{coll,-1} \ll k_{rad,-1}$ (where $k_{coll,-1}$ is the rate of energy loss through collisions and $k_{rad,-1}$ is the rate of photon emission). Therefore, collisions with background gas contribute negligibly to the overall thermal energy transfer between ion populations.[117] Instead, ions in the zero-pressure limit primarily gain and lose energy through interaction with the blackbody field originating from the instrument walls. For large complexes of mass ∼1.6 kDa and greater, ions can rapidly exchange energy through radiative processes to maintain thermal equilibrium with their surroundings,[51] *i.e.*, $k_d \ll k_{rad,-1}$, where k_d is the rate of dissociation. Therefore, large ion complexes stored at the zero-pressure limit in an instrument chamber at 200 K will result in a thermal distribution of ions with an effective temperature of 200 K. However, small complexes ($\leq$ 100 degrees of freedom) and intermediate complexes between the two size regimes with sufficient internal energies can dissociate on a timescale faster than thermalization *via* radiative processes.

For small ions, zero-pressure conditions leads to a “sudden death” kinetic limit, where ions with sufficient energy above the threshold for dissociation are trapped in a reactive state and quickly dissociate due to the absence of any competitive alternate pathway for relaxing their internal energies, *i.e.*, $k_d \gg k_{rad,-1}$. This results in a depletion of the high-energy tail and an overall shift of the ion distribution to lower energies, consequently resulting in a lower effective ion temperature. The resulting population distribution of small ions can be adequately modeled using the Truncated Boltzmann approximation.[50,118,119] In its simplest implementation, a Boltzmann distribution is calculated for the ion complex at the surrounding instrumental temperature and all populated states above $E \geq E_0 - 1/2 \cdot \langle h\nu \rangle_{abs}$ are set to zero as a first-order approximation for depletion, where $\langle h\nu \rangle_{abs}$ is the average energy of photons absorbed and is dependent on the surrounding blackbody field. This approximation does not hold for intermediate-sized ion complexes, where radiative processes occur on the same timescale as depletion, *i.e.*, $k_d \simeq k_{rad,-1}$. This size regime includes the ion-containing nanodroplets studied in Chapters 2, 3, & 4.

To model the internal energies of intermediate-sized ions as a function of time, the microcanonical rate constants for photon absorption, $k_{rad,1}$, photon emission, $k_{rad,-1}$, and dissociation, k_d, must each be accounted for throughout the timescale of the experiment. This is accomplished through incorporation of master equation modeling, whereby an initial Boltzmann distribution at $t = 0$ for the ion complex at the temperature of the surroundings is partitioned into several energy bins of fixed width.[120] The population of the i^{th} energy bin with respect to time is calculated *via* a set of first-order differential equations:

$$\frac{dN_i}{dt} = \sum_{i \neq j} [k_{rad,1}(\Delta E_{j \to i}) \cdot N_j - k_{rad,1}(\Delta E_{i \to j}) \cdot N_i] - k_d(E_i) \cdot N_i \qquad \text{(Equation 1.3)}$$

where N_i is the population of the i^{th} energy bin. The set of equations is commonly implemented in a matrix formalism,[52] where elements from Equation 1.3 are organized into a transport or J matrix, which allows for the unimolecular rate constant, k_{uni}, to be solved as the least negative eigenvalue. This approach has been successful for modeling the depletion of ion distributions for several non-covalent complexes, including amino acids,[52,121] nucleotides,[122] peptides,[51] proteins,[123] and small water clusters.[120,124] Although master equation modeling has traditionally been used in the zero-pressure limit, an appendage to the expression in Equation 1.3 could be included to incorporate rates of collisions for pressures above $\sim 10^{-8}$ Torr. This would be particularly useful for investigating the population depletion of systems where the rate of energy loss *via* collisions, $k_{coll,-1}$, is also comparable to $k_{rad,-1}$ and k_d, such that collisions do not effectively thermalize the population, but lie between the two extremes for pressure regimes. In Chapter 5, we implement master equation modeling of $SO_4^{2-}(H_2O)_n$ with $n = 30 - 45$ in order to quantify the effective temperature of these nanodroplets once they have reached a steady state with the surrounding blackbody field. These calculations complement the IRPD experiments in Chapter 4 and reveal that rapid evaporative cooling of $SO_4^{2-}(H_2O)_{30}$ stored in an ion trap at 340 K leads to an effective temperature of ∼180 K, or an offset of $\Delta T = 160$ K.

1.5 The Terahertz Dance of Liquid Water

The electromagnetic region corresponding to sub-millimeter wavelengths with $\sim 10^{12}$ Hz frequencies has been commonly referred to as the "terahertz gap". This term is a result of the incomplete convergence between low-frequency electronics technologies utilized for microwave production and the high-frequency optical generation *via* lasing media for infrared photons.[125] Absorption of radiation in the terahertz (THz) regime by aqueous solutions corresponds to the collective reconfiguration of hydrogen bonding partners between water molecules (∼6 THz, or 200 cm^{-1}) as well as their collective librational motions (≥9 THz, or 300 cm^{-1}).[126,127] These dynamic, intermolecular motions of liquid water can be investigated as a function of solute concentration to observe the ionic influence on the collective absorptive behavior of water molecules. As a result, spectroscopic studies in the THz region can provide a useful complement to the long distance structural perturbations observed in aqueous ion-containing nanodroplets (Chapters 2, 3, & 4). One of the largest challenges for applying THz to aqueous systems has been producing accessible systems capable of high-power output that can traverse a sample of strongly absorbing water molecules. Considerable advancements for producing THz radiation have emerged in the last few decades,[128] such as the production of synchrotron radiation from the Angströmquelle Karlsruhe (ANKA), located in southwest Germany. Furthermore, the advancement of compact systems, which are more adequate for individual laboratory use, have emerged as a result of advances in quantum cascade lasers,[129,130] *p*-germanium-based lasers,[131,132] time-domain setups,[133,134] and also commercial Fourier transform terahertz systems (FT-THz).[28,29] Current commercial FT-THz table top systems are capable of measuring continuous THz spectra between ∼1 − 15 THz (30 − 500 cm^{-1}) of aqueous samples in liquid cells of ∼25 µm thickness. As a result of their availability and wide spectral range, experiments utilizing FT-THz have recently become an effective means with which to examine the dynamic structure of water molecules in solution.

Unlike the more commonly adopted spectroscopic methods utilizing infrared, ultraviolet, and visible wavelengths, terahertz spectroscopy is still an emerging frontier for probing aqueous solutions. Therefore, the development of proper analytical methodologies with which to interpret spectral absorptions in this region are required. Considerable efforts by Havenith *et al.* have resulted in the investigation of glycine,[135] alkyl hydroxides,[136] and mono-,[137] di-,[30,138] and trivalent cationic salts.[29,139] A broadband THz spectrum for the effective ionic contributions to absorption, $\alpha_{ion}^{eff}(\widetilde{\nu})$, is generated by subtracting a scaled spectrum of pure bulk water, $\alpha_{H_2O,f}(\widetilde{\nu})$, from the raw solution spectrum, $\alpha_{solution}(\widetilde{\nu})$, as expressed below:

$$\alpha_{ion}^{eff}(\widetilde{\nu}) = \alpha_{solution}(\widetilde{\nu}) - \left(\frac{c_{H_2O,solution}}{55.409 \text{ mol L}^{-1}}\right) \cdot \alpha_{H_2O,f}(\widetilde{\nu}) \qquad \text{(Equation 1.4)}$$

where $c_{H_2O,solution}$ is the measured concentration of water for a given solution. This method inherently overcompensates for the amount of *bulk-like* water in solution during the scaled subtraction of $\alpha_{H_2O,f}(\widetilde{\nu})$, *i.e.*, the subtraction assumes an idealistic solution in which every water molecule behaves like pure bulk water and is not perturbed in the vicinity of solutes. If this case were true, the only absorption observed in $\alpha_{ion}^{eff}(\widetilde{\nu})$ would be from low-frequency intramolecular stretches. More realistically, the presence of ions in solution results in a shift of the THz absorption for water molecules with perturbed dynamics, *e.g.*, direct coordination or extended solvation shells. However, this method is advantageous in that the overcompensation is directly proportional to the amount of water molecules with perturbed dynamics, with respect to bulk water. For instance, if 25% of the water molecules have shifted absorption due to interaction with ions, subtracting the scaled $\alpha_{H_2O,f}(\widetilde{\nu})$ as in Equation 1.4 will result in a *negative* contribution to $\alpha_{ion}^{eff}(\widetilde{\nu})$ equal to 25% of the total water concentration. By fitting each component of $\alpha_{ion}^{eff}(\widetilde{\nu})$ with damped harmonic lineshapes, the negative contribution can be deconvolved and used to report the extent of *dynamic* ion-water interactions in solution.[29] In Chapter 6, we discuss the THz spectra of $\mathrm{Fe(CN)}_6^{4-}$ and $\mathrm{Fe(CN)}_6^{3-}$ salts and conclude that the hexacyanoferrates dynamically pattern water molecules beyond the first solvation shell.[28] These studies provide an essential counterpart to the *structural* patterning observed in ion-containing nanodroplets and illustrate that the extended interactions measured in the gas phase are indeed relevant to solutions under ambient conditions.

1.6 References

[1] Ouyang, J.; Garner, E.; Hallet, A.; Nguyen, H. D.; Rickman, K. A.; Gill, G.; Smogorzewska, A.; Zou, L. *Mol. Cell* **2015**, *57*, 108–122.

[2] Dopfer, O.; Fujii, M. *Chem. Rev.* **2016**, *116*, 5432–5463.

[3] Gugliuzza, A.; Politano, A.; Drioli, E. *Curr. Opin. Chem. Eng.* **2017**, *16*, 78–85.

[4] Sneddon, G.; Greenaway, A.; Yiu, H. *Adv. Energy Mater.* **2014**, *4*, 1301873.

[5] Fersht, A. *Structure and Mechanism in Protein Science: A Guide to Enzyme Catalysis and Protein Folding*; W. H. Freeman and Company, New York, 1999.

[6] Schulze, B.; Klibanov, A. M. *Biotechnol. Bioeng.* **1991**, *38*, 1001–1006.

[7] Zaks, A.; Klibanov, A. M. *J. Biol. Chem.* **1988**, *263*, 3194–3201.

[8] Marcus, Y. *Chem. Rev.* **2009**, *109*, 1346–1370.

[9] Heyda, J.; Kožíšek, M.; Bednárova, L.; Thompson, G.; Konvalinka, J.; Vondrášek, J.; Jungwirth, P. *J. Phys. Chem. B* **2011**, *115*, 8910–8924.

[10] Makhatadze, G. I. *J. Phys. Chem. B* **1999**, *103*, 4781–4785.

[11] Song, J.; Kang, T. H.; Kim, M. W.; Han, S. *Phys. Chem. Chem. Phys.* **2015**, *17*, 8306–8322.

[12] Hofmeister, F. *Arch. Exp. Pathol. Pharmacol.* **1888**, *24*, 247–260.

[13] Okur, H. I.; Hladílková, J.; Rembert, K. B.; Cho, Y.; Heyda, J.; Dzubiella, J.; Cremer, P. S.; Jungwirth, P. *J. Phys. Chem. B* **2017**, *121*, 1997–2014.

[14] Jungwirth, P.; Cremer, P. S. *Nat. Chem.* **2014**, *6*, 261–263.

[15] Nostro, P. L.; Ninham, B. W. *Chem. Rev.* **2012**, *112*, 2286–2322.

[16] Zhang, Y.; Cremer, P. S. *Curr. Opin. Chem. Biol.* **2006**, *10*, 1–6.

[17] Amaan-Winkel, K.; Bellissent-Funel, M. C.; Bove, L. E.; Loerting, T.; Nilsson, A.; Paciaroni, A.; Schlesinger, D.; Skinner, L. *Chem. Rev.* **2016**, *116*, 7570–7589.

[18] Skipper, N. T.; Neilson, G. W. *J. Phys.: Condens. Matter* **1989**, *1*, 4141–4154.

[19] Huang, C. et al. *Proc. Natl. Acad. Sci. USA* **2009**, *106*, 15214–15218.

[20] Bouazizi, S.; Nasr, S.; Jaîdane, N.; Bellissent-Funel, M. C. *J. Phys. Chem. B* **2006**, *110*, 23515–23523.

[21] Mancinelli, R.; Botti, A.; Bruni, F.; Ricci, M. A.; Soper, A. K. *Phys. Chem. Chem. Phys.* **2007**, *9*, 2959–2967.

[22] Mason, P. E.; Cruickshank, J. M.; Neilson, G. W.; Buchanan, P. *Phys. Chem. Chem. Phys.* **2003**, *5*, 4686–4690.

[23] Van der Post, S. T.; Tielrooij, K.; Hunger, J.; Backus, E. H.; Bakker, H. J. *Faraday Discuss.* **2013**, *160*, 171–189.

[24] Fournier, J. A.; Carpenter, W.; Marco, L. D.; Tokmakoff, A. *J. Am. Chem. Soc.* **2016**, *138*, 9634–9645.

[25] Moilanen, D. E.; Wong, D.; Rosenfeld, D. E.; Fenn, E. E.; Fayer, M. D. *Proc. Natl. Acad. Sci. USA* **2009**, *106*, 375–380.

[26] Bergström, P.-Å.; Lindgren, J. *J. Phys. Chem.* **1991**, *95*, 7650–7655.

[27] Stangret, J.; Gampe, T. *J. Phys. Chem. A* **2002**, *106*, 5393–5402.

[28] DiTucci, M. J.; Böhm, F.; Schwaab, G.; Williams, E. R.; Havenith, M. *Phys. Chem. Chem. Phys.* **2017**, *19*, 7297–7306.

[29] Böhm, F.; Sharma, V.; Schwaab, G.; Havenith, M. *Phys. Chem. Chem. Phys.* **2015**, *17*, 19582–19591.

[30] Sharma, V.; Böhm, F.; Schwaab, G.; Havenith, M. *Phys. Chem. Chem. Phys.* **2014**, *16*, 25101–25110.

[31] Chizhik, V. I. *Mol. Phys.* **1997**, *90*, 653–659.

[32] Bleuzen, A.; Foglia, F.; Furet, E.; Helm, L.; Merbach, A. E.; Weber, J. *J. Am. Chem. Soc.* **1996**, *118*, 12777–12787.

[33] Chizhik, V. I.; Egorov, A. V.; Komolkin, A. V.; Vorontsova, A. A. *J. Mol. Liq.* **2002**, *98*, 173–182.

[34] Vovk, M. A.; Pavlova, M. S.; Chizhik, V. I.; Vorontsova, A. A. *Russ. J. Phys. Chem. A* **2011**, *85*, 1597–1602.

[35] Jia, G.-Z.; Liu, S.; Liu, F.-H.; Liu, J.-C. *J. Dispersion Sci. Technol.* **2016**, 1–5.

[36] Eiberweiser, A.; Nazet, A.; Hefter, G.; Buchner, R. *J. Phys. Chem. B* **2015**, *119*, 5270 – 5281.

[37] Buchner, R. *Pure Appl. Chem.* **2008**, *80*, 1239–1252.

[38] Pluharová, E.; Laage, D.; Jungwirth, P. *Phys. Chem. Lett.* **2017**, *8*, 2031–2035.

[39] Hou, G. L.; Liu, C. W.; Li, R. Z.; Xu, H. G.; Gao, Y. Q.; Zheng, W. J. *Phys. Chem. Lett.* **2017**, *8*, 13–20.

[40] Du, H.; Rasaiah, J. C.; Miller, J. D. *J. Phys. Chem. B* **2007**, *111*, 209–217.

[41] Bucher, D.; Guidoni, L.; Carlioni, P.; Rothlisberger, U. *Biophys. J.* **2010**, *98*, 47–49.

[42] Miller, D. J.; Lisy, J. M. *J. Am. Chem. Soc.* **2008**, *130*, 15381–15392.

[43] Zhou, J.; Ssantambrogio, G.; Brümmer, M.; Moore, D. T.; Wöste, L.; Meijer, G.; Neumark, D. M.; Asmis, K. R. *J. Chem. Phys.* **2006**, *125*, 111102.

[44] Walters, R. S.; Pillai, E. D.; Duncan, M. A. *J. Am. Chem. Soc.* **2005**, *127*, 16599–16610.

[45] Wang, X. B.; Sergeeva, A. P.; Xing, X. P.; Massaouti, M.; Karpuschkin, T.; Hampe, O.; Boldyrev, A. I.; Kappes, M. M.; Wang, L. S. *J. Am. Chem. Soc.* **2009**, *131*, 9836–9842.

[46] Bush, M. F.; O'Brien, J. T.; Prell, J. S.; Saykally, R. J.; Williams, E. R. *J. Am. Chem. Soc.* **2007**, *129*, 1612–1622.

[47] Fournier, J. A.; Johnson, C. J.; Wolke, C. T.; Weddle, G. H.; Wolk, A. B.; Johnson, M. A. *Science* **2014**, *344*, 1009–1012.

[48] Lee, S.-W.; Cox, H.; Goddard, W. A.; Beauchamp, J. L. *J. Am. Chem. Soc.* **2000**, *122*, 9201–9205.

[49] DiTucci, M. J.; Williams, E. R. *Chem. Sci.* **2017**, *8*, 1391–1399.

[50] Dunbar, R. C. *Mass Spectrom. Rev.* **2004**, *23*, 127 – 158.

[51] Price, W. D.; Williams, E. R. *J. Phys. Chem. A* **1997**, *101*, 8844–8852.

[52] Price, W. D.; Schnier, P. D.; Williams, E. R. *J. Phys. Chem. B* **1997**, *101*, 664–673.

[53] Headrick, J. M.; Diken, E. G.; Walters, R. S.; Hammer, N. I.; Christie, R. A.; Cui, J.; Myshakin, E. M.; Duncan, M. A.; Johnson, M. A.; Jordan, K. D. *Science* **2005**, *308*, 1765–1769.

[54] Diken, E. G.; Hammer, N. I.; Johnson, M. A.; Christie, R. A.; Jordan, K. D. *J. Chem. Phys.* **2005**, *123*, 164309.

[55] Lee, S.-W.; Freivogel, P.; Schindler, T.; Beauchamp, J. L. *J. Am. Chem. Soc.* **1998**, *120*, 11758–11765.

[56] Hammer, N. I.; Roscioli, J. R.; Bopp, J. C.; Headrick, J. M.; Johnson, M. A. *J. Chem. Phys.* **2005**, *123*, 244311.

[57] Bush, M. F.; Saykally, R. J.; Williams, E. R. *J. Am. Chem. Soc.* **2007**, *129*, 2220–2221.

[58] Heiles, S.; Cooper, R. J.; DiTucci, M. J.; Williams, E. R. *Chem. Sci.* **2017**, *8*, 2973–2982.

[59] Donald, W. A.; Leib, R. D.; Demireva, M.; Williams, E. R. *J. Am. Chem. Soc.* **2011**, *133*, 18940–18949.

[60] Donald, W. A.; Williams, E. R. *Pure Appl. Chem.* **2011**, *83*, 2129–2151.

[61] A., D. W.; Williams, E. R. In *Electroanalytical Chemistry: A Series of Advances - Chapter 1: Measuring Absolute Single Half-Cell Reduction Potentials with Mass Spectrometry*; J., B. A., G., Z. C., Eds.; CRC Press: Boca Raton, 2014; Vol. 25.

[62] Schröder, D.; Schwarz, H. *J. Phys. Chem. A* **1999**, *103*, 7358–7394.

[63] Boldyrev, A. I.; Simons, J. *J. Phys. Chem.* **1994**, *98*, 2298–2300.

[64] Whitehead, A.; Barrios, R.; Simons, J. *J. Chem. Phys.* **2002**, *116*, 2848–2851.

[65] Schauer, S. N.; Williams, P.; Compton, R. N. *Phys. Rev. Lett.* **1990**, *65*, 625–628.

[66] Dreuw, A.; Cederbaum, L. S. *Phys. Rev. A* **2000**, *63*, 012501.

[67] Wang, X. B.; Ding, C. F.; Wang, L. S. *Phys. Rev. Lett.* **1998**, *81*, 3351–3354.

[68] Hampe, O.; Neumaier, M.; Blom, M. N.; Kappes, M. M. *Chem. Phys. Lett.* **2002**, *354*, 303–309.

[69] Petrie, S.; Wang, J.; Böhme, D. K. *Chem. Phys. Lett.* **1993**, *204*, 473–480.

[70] Williams, E. R. *J. Mass Spectrom.* **1996**, *31*, 831–842.

[71] Yoo, H. J.; Wang, N.; Zhuang, S.; Song, H.; Håkansson, K. *J. Am. Chem. Soc.* **2011**, *133*, 16790–16793.

[72] Boxford, W. E.; Dessent, C. E. H. *Phys. Chem. Chem. Phys.* **2006**, *8*, 5151–5165.

[73] Danell, A. S.; Parks, J. H. *J. Am. Soc. Mass Spectrom.* **2003**, *14*, 1330–1339.

[74] Arnold, K.; Balaban, T. S.; Blom, M. N.; Ehrler, O. T.; Gilb, S.; Hampe, O.; Lier, J. E.; Weber, J. M.; Kappes, M. M. *J. Phys. Chem. A* **2003**, *107*, 794–803.

[75] Wang, X. B.; Nicholas, J. B.; Wang, L. S. *J. Chem. Phys.* **2000**, *113*, 10837–10840.

[76] Wang, L. S.; Ding, C. F.; Wang, X. B.; Nicholas, J. B. *Phys. Rev. Lett.* **1998**, *81*, 2667–2670.

[77] Yamashita, M.; Fenn, J. B. *J. Phys. Chem.* **1984**, *88*, 4451–4459.

[78] Fenn, J. B.; Mann, M.; Meng, C. K.; Wong, S. F. *Mass Spectrom. Rev.* **1990**, *9*, 37–70.

[79] Wang, X. B.; Yang, X.; Nicholas, J. B.; Wang, L. S. *J. Chem. Phys.* **2003**, *119*, 3631–3640.

[80] Xin, Y.; Wang, X. B.; Wang, L. S. *J. Phys. Chem. A* **2002**, *106*, 7607–7616.

[81] Cooper, T. E.; Armentrout, P. B. *J. Phys. Chem. A* **2009**, *113*, 13742–13751.

[82] Wong, R. L.; Williams, E. R. *J. Phys. Chem. A* **2003**, *107*, 10976–10983.

[83] Gao, B.; Liu, Z. *J. Chem. Phys.* **2005**, *123*, 224302.

[84] Blades, A. T.; Kebarle, P. *J. Am. Chem. Soc.* **1994**, *116*, 10761–10766.

[85] DiTucci, M. J.; Heiles, S.; Williams, E. R. *J. Am. Chem. Soc.* **2015**, *137*, 1650 – 1657.

[86] Polfer, N. C. *Chem. Soc. Rev.* **2011**, *40*, 2211–2221.

[87] Eyler, J. R. *Mass Spectrom. Rev.* **2009**, *28*, 448–467.

[88] Asmis, K. R.; Neumark, D. M. *Acc. Chem. Res.* **2012**, *45*, 43–52.

[89] Paul, J. B.; Provencal, R. A.; Saykally, R. J. *J. Phys. Chem. A* **1998**, *102*, 3279–3283.

[90] Provencal, R. A.; Casaes, R. N.; Roth, K.; Paul, J. B.; Chapo, C. N.; Tschumper, G. S.; Schaefer, H. F.; Saykally, R. J. *J. Phys. Chem. A* **2000**, *104*, 1423–1429.

[91] Prell, J. S.; O'Brien, J. T.; Williams, E. R. *J. Am. Soc. Mass Spectrom.* **2010**, *21*, 800–809.

[92] Okumura, M.; Yeh, L. I.; Myers, J. D.; Lee, Y. T. *J. Chem. Phys.* **1986**, *85*, 2328–2329.

[93] Garand, E.; Kamrath, M. Z.; Jordan, P. A.; Wolk, A. B.; Leavitt, C. M.; McCoy, A. B.; Miller, S. J.; Johnson, M. A. *Science* **2012**, *335*.

[94] Oomens, J.; Morton, T. H. *Angew. Chem. Int. Ed.* **2008**, *47*, 2106–2108.

[95] Dunbar, R. C.; Steill, J. D.; Oomens, J. *Int. J. Mass. Spectrom.* **2010**, *297*, 107–115.

[96] Nieto, P.; Günther, A.; Berden, G.; Oomens, J.; Dopfer, O. *J. Phys. Chem. A* **2016**, *120*, 8297–8308.

[97] Kamariotis, A.; Boyarkin, O. V.; Mercier, S. R.; Beck, R. D.; Bush, M. F.; Williams, E. R.; Rizzo, T. R. *J. Am. Chem. Soc.* **2006**, *128*, 905–916.

[98] Balaj, O. P.; Kapota, C.; Lemaire, J.; Ohanessian, G. *Int. J. Mass. Spectrom.* **2008**, *269*, 196–209.

[99] Fukui, K.; Takada, Y.; Sumiyoshi, T.; Imai, T.; Takahashi, K. *J. Phys. Chem. B* **2006**, *110*, 16111–16116.

[100] Cooper, R. J.; Heiles, S.; DiTucci, M. J.; Williams, E. R. *J. Phys. Chem. A* **2014**, *118*, 5657–5666.

[101] Heiles, S.; Cooper, R. J.; DiTucci, M. J.; Williams, E. R. *Chem. Sci.* **2015**, *6*, 3420–3429.

[102] Demireva, M.; O'Brien, J. T.; Williams, E. R. *J. Am. Chem. Soc.* **2012**, *134*, 11216–11224.

[103] Wende, T.; Wanko, M.; Jiang, L.; Meijer, G.; Asmis, K. R.; Rubio, A. *Angew. Chem. Int. Ed.* **2011**, *50*, 3807–3810.

[104] O'Brien, J. T.; Prell, J. S.; Bush, M. F.; Williams, E. R. *J. Am. Chem. Soc.* **2010**, *132*, 8248–8249.

[105] O'Brien, J. T.; Williams, E. R. *J. Phys. Chem. A* **2011**, *115*, 14612–14619.

[106] Thaunay, F.; Clavaguéra, C.; Ohanessian, G. *Phys. Chem. Chem. Phys.* **2015**, *17*, 25935–25945.

[107] Cooper, R. J.; Chang, T. M.; Williams, E. R. *J. Phys. Chem. A* **2013**, *117*, 6571–6579.

[108] Chang, T. M.; Cooper, R. J.; Williams, E. R. *J. Am. Chem. Soc.* **2013**, *135*, 14821–14830.

[109] Chakrabarty, S.; Williams, E. R. *Phys. Chem. Chem. Phys.* **2016**, *18*, 25483–25490.

[110] Nihonyanagi, S.; Yamaguchi, S.; Tahara, T. *Chem. Rev.* **2017**, *117*, 10665–10693.

[111] Kundu, A.; Tanaka, S.; Ishiyama, T.; Ahmed, M.; Inoue, K.; Nihonyangi, S.; Sawai, H.; Yamaguchi, S.; Morita, A.; Tahara, T. *Phys. Chem. Lett.* **2016**, *7*, 2597–2601.

[112] Engelhardt, K.; Peukert, W.; Braunschweig, B. *Curr. Opin. Colloid Interface Sci.* **2014**, *19*, 207–215.

[113] O'Brien, J. T.; Williams, E. R. *J. Am. Chem. Soc.* **2012**, *134*, 10228–10236.

[114] Cooper, R. J.; DiTucci, M. J.; Chang, T. M.; Williams, E. R. *J. Am. Chem. Soc.* **2016**, *138*, 96–99.

[115] Pradzynski, C. C.; Forck, R. M.; Zeuch, T.; Slaviček, P.; Buck, U. *Science* **2012**, *337*, 1529 – 1532.

[116] Omta, A. W.; Kropman, M. F.; Woutersen, S.; Bakker, H. J. *Science* **2003**, *301*, 347–349.

[117] Thölmann, D.; Tonner, D. S.; McMahon, T. B. *J. Phys. Chem.* **1994**, *98*, 2002–2004.

[118] Dunbar, R. C. *J. Phys. Chem.* **1994**, *98*, 8705–8712.

[119] Dunbar, R. C. *J. Chem. Phys.* **1991**, *95*, 2537–2548.

[120] Dunbar, R. C.; McMahon, T. B.; Thölmann, D.; Tonner, D. S.; Salahub, D. R.; Wei, D. *J. Am. Chem. Soc.* **1995**, *117*, 12819–12825.

[121] Jockush, R. A.; Williams, E. R. *J. Phys. Chem. A* **1998**, *102*, 4543–4550.

[122] Strittmatter, E. F.; Schnier, P. D.; Klassen, J. S.; Williams, E. R. *J. Am. Soc. Mass Spectrom.* **1999**, *10*, 1095–1104.

[123] Schnier, P. D.; Price, W. D.; Strittmatter, E. F.; Williams, E. R. *J. Am. Soc. Mass Spectrom.* **1997**, *8*, 771–780.

[124] Wong, R. L.; Paech, K.; Williams, E. R. *Int. J. Mass. Spectrom.* **2004**, *232*, 59–66.

[125] Sirtori, C. *Nature* **2002**, *417*, 132–133.

[126] Bertie, J. E.; Lan, Z. *Appl. Spectrosc.* **1996**, *50*, 1047–1057.

[127] Heyden, M.; Sun, J.; Funkner, S.; Mathias, G.; Forbert, H.; Havenith, M.; Marx, D. *Proc. Natl. Acad. Sci. USA* **2010**, *107*, 12068–12073.

[128] Schmuttenmaer, C. A. *Chem. Rev.* **2004**, *104*, 1759–1779.

[129] Köhler, R.; Tredicucci, A.; Beltram, F.; Beere, H. E.; Linfield, E. H.; Davies, A. G.; Ritchie, D. A.; Lotti, R. C.; Rossi, F. *Nature* **2002**, *417*, 156–159.

[130] Williams, B. S. *Nat. Photonics* **2007**, *1*, 517–525.

[131] Bründermann, E.; Born, B.; Funkner, S.; Krüger, M.; Havenith, M. *Proc. SPIE* **2009**, *7215*, 72150E.

[132] Plusquellic, D. V.; Siegrist, K.; Heilweil, E. J.; Esenturk, O. *ChemPhysChem* **2007**, *8*, 2412–2431.

[133] Kim, S. J.; Born, B.; Havenith, M.; Gruebele, M. *Angew. Chem. Int. Ed.* **2008**, *47*, 6486–6489.

[134] Sebastiani, F.; Wolf, S. L. P.; Born, B.; Luong, T. Q.; Cölfen, H.; Gebauer, D.; Havenith, M. *Angew. Chem. Int. Ed.* **2017**, *56*, 490–495.

[135] Sun, J.; Niehues, G.; Forbert, H.; Decka, D.; Schwaab, G.; Marx, D.; Havenith, M. *J. Am. Chem. Soc.* **2014**, *136*, 5031–5038.

[136] Böhm, F.; Schwaab, G.; Havenith, M. *Angew. Chem. Int. Ed.* **2017**, *56*, 9981–9985.

[137] Schmidt, D. A.; Birer, Ö.; Funkner, S.; Born, B. P.; Gnanasekaran, R.; Schwaab, G. W.; Leitner, D. M.; Havenith, M. *J. Am. Chem. Soc.* **2009**, *131*, 18512–18517.

[138] Funkner, S.; Niehues, G.; Schmidt, D. A.; Heyden, M.; Schwaab, G.; Callahan, K. M.; Tobias, D. J.; Havenith, M. *J. Am. Chem. Soc.* **2012**, *134*, 1030–1035.

[139] Sharma, V.; Böhm, F.; Seitz, M.; Schwaab, G.; Havenith, M. *Phys. Chem. Chem. Phys.* **2013**, *15*, 8383–8391.

Chapter 2

Role of Water in Stabilizing Ferricyanide Trianion and Ion-Induced Effects to the Hydrogen Bonding Water Network at Long Distance

This chapter is reproduced with permission from:
Matthew J. DiTucci, Sven Heiles, and Evan R. Williams
"Role of Water in Stabilizing Ferricyanide Trianion and Ion-Induced Effects to the Hydrogen Bonding Water Network at Long Distance",
J. Am. Chem. Soc. **2015**, *137*, 1650–1657.

2.1 Introduction

High valency ions are common in solution, where surrounding water or other solvent molecules can stabilize the charge.[1] Large, multiply charged molecules, such as those produced by electrospray ionization of proteins, DNA, carbohydrates, or other large molecules, can be very stable, even without solvent, owing to high intrinsic charge affinities and to the typically large separation distances between charges.[2–5] Much smaller, multiply charged species, such as multivalent atomic ions or those formed from small molecules, are much more reactive owing to significant Coulomb energy in the bare ions.[6–30] In the gas phase, these ions often either spontaneously dissociate in charge-separation reactions[7–11,21–26,29] or transfer charge to other molecules in collisions, *e.g.*, proton transfer.[12]

The reactivities of highly charged small molecular and atomic ions have been extensively investigated.[6–41] Schwarz and coworkers found that the product ions, $Cu^+ + X^+$ ($X = H_2O$, NH_3) formed by charge-separation of $Cu(X)^{2+}$ ($X = H_2O$, NH_3), are thermodynamically more stable but $Cu(X)^{2+}$ is metastable because of a Coulomb barrier.[35] A Coulomb barrier in the charge-separation reactions of multiply charged ions, both positive and negative, arises from the combined potentials for short-range binding interactions and long-range charge-charge repulsion.[3,4,18,30,31] The stabilities of highly charged ions can be enhanced by solvation. For example, isolated SO_4^{2-} is unstable with respect to electron loss with a calculated lifetime of 1.6×10^{-10} s.[34] However, this ion can be stabilized by water molecules and can be observed in the form of hydrated clusters, $SO_4^{2-}(H_2O)_n$. Wang and coworkers showed through photoelectron spectroscopy (PES) studies that each additional water molecule increases the barrier for electron loss.[39,41] Extrapolation of these PES data to smaller cluster sizes indicated that clusters with $n = 1$ and 2 are electronically unstable by -0.9 and -0.2 eV, respectively, in excellent agreement with computed values.[27] From these results, Wang and coworkers concluded that three water molecules are necessary to stabilize SO_4^{2-}. Blades and Kebarle reported formation of $SO_4^{2-}(H_2O)_2$, indicating that this species has a sufficient lifetime to be observed in a mass spectrometer.[25]

For bare multivalent cations, charge-separation to form protonated water or protonated water clusters can occur upon the sequential addition of water molecules.[14–17] Addition of a water molecule to $Ca^{2+}(H_2O)$ results in the formation of $CaOH^+$ and H_3O^+, a reaction that can occur through a $M^{2+}{-}OH^-{-}H_3O^+$ salt-bridge intermediate structure.[16] For this reason, large hydrated clusters of many multivalent ions cannot be formed by condensing water molecules sequentially onto the bare ion.

Extensively hydrated multiply charged ions can be readily formed by electron ionization of singly charged clusters[32,33] or by electrospray ionization,[10,42,43] and these methods provide an excellent means by which to investigate the role of water in stabilizing multivalent ions. Evaporation of water molecules from large clusters can result in charge-separation reactions at smaller cluster size. For multivalent anions, charge-separation can occur either by electron loss or by loss of OH^- or $OH^-(H_2O)_n$.[24–26] The cluster size at which charge separation competes with the loss of a water molecule depends on the internal energy of the cluster and the identity of the ion. For example, blackbody infrared dissociation (BIRD) of $SO_4^{2-}(H_2O)_n$ at 21 °C results predominantly in loss of a water molecule for $n \geq 6$, but predominantly in charge separation for $n = 5$.[24] However, loss of a water molecule is entropically favored,[24] and smaller clusters of SO_4^{2-} can be produced by using more energetic activation conditions.

The smallest cluster for which a multivalent ion is observed has often been referred to as the critical size, n_c, and a number of values for different ions have been reported. Critical cluster sizes for the dications, such as Zn^{2+}, Co^{2+}, Be^{2+}, and Cu^{2+}, range from ∼2 to 7,[8,9,29] and for trivalent cations, such as Ce^{3+}, La^{3+}, Tb^{3+}, and Lu^{3+}, from ∼15 to 18.[10,11] Significantly more water molecules are required to stabilize the higher charge density on trivalent monoatomic ions compared to that of the divalent monoatomic ions. Because the observed cluster size of hydrated multivalent ions depends on the internal energy that is deposited into larger clusters as well as the lifetime of the ion, a more consistent definition of critical size as *the cluster size at which charge separation is energetically favored over the loss of one water molecule* has been proposed.[29]

Here, the dissociation pathways of hydrated clusters of the small trianion ferricyanide, $Fe(CN)_6^{3-}(H_2O)_n$, are investigated using BIRD, infrared photodissociation (IRPD), spectroscopy, and computational chemistry. Although $Fe(CN)_6^{3-}(H_2O)_8$ is the smallest cluster observed in electrospray ionization mass spectra under a wide variety of conditions, clusters with seven water molecules are stable when large clusters are activated with photons generated by an IR laser, and evidence for clusters with six water molecules is presented. For these small clusters, charge separation occurs via electron loss. Although both bare $P_3O_9^{3-}$

and $Co(NO_2)_6^{3-}$ have been reported previously,[44] these ions are not formed under identical conditions for successfully generating $Fe(CN)_6^{3-}(H_2O)_n$. We find that $P_3O_9^{3-}$ is only observed with six or more water molecules attached, and this ion undergoes charge separation to form $HP_3O_9^{2-}(H_2O)_5$+ OH^-. This is the first report of a critical cluster size for small trianions, and these are the smallest trianions (highest charge density) that have been observed in the gas phase.

2.2 Experimental Methods

2.2.1 Mass Spectra

All experimental data were obtained using a home-built Fourier transform ion cyclotron resonance (FT-ICR) mass spectrometer that is described elsewhere[45] and has been upgraded to incorporate a 7 T magnet. Hydrated ions are formed by nanoelectrospray ionization (nESI) of 5 mM aqueous solutions of potassium ferricyanide (Matheson Coleman & Bell, Norwood, OH) using a Milli-Q purified water system (Millipore, Billerica, MA). Solutions are loaded into borosilicate capillaries that have tips pulled to an inner diameter of ∼1 µm. A platinum wire that is in contact with the solution is held at a constant potential of ∼700 V with respect to a heated metal capillary at the entrance of the instrument. Ions are guided *via* electrostatic lenses through five stages of differential pumping into the ion cell, which is enclosed by a copper jacket and is temperature controlled by a regulated flow of liquid nitrogen to 133 K for at least 8 h prior to data acquisition.[46] A pulse of dry nitrogen gas is introduced into the instrument for ∼6 s, bringing the pressure of the vacuum chamber containing the ion cell to $\sim 2 \times 10^{-6}$ Torr, which helps to both trap and thermalize the ions. After an ∼8 s pump down period following the pulse gas, the pressure in the chamber decreases to $\sim 2 \times 10^{-9}$ Torr. Precursor ions of interest are subsequently isolated using a notched stored waveform inverse Fourier transform (SWIFT) excitation.

2.2.2 Infrared Photodissociation

IRPD spectra between 2900 and 3800 cm^{-1} are measured using infrared photons from a tunable OPO/OPA system (LaserVision, Bellevue, WA) pumped by the 1064 nm fundamental of a Nd:YAG laser (Continuum Surelight I-10, Santa Clara, CA) operating at a 10 Hz repetition rate. Ions are irradiated for between ∼0.5 and 3.0 s in order to produce substantial, but not complete, dissociation of the precursor. A first-order rate constant is derived from the relative abundances of precursor and product ions after photodissociation. BIRD rate constants are obtained from the dissociation of the precursor in the absence of laser irradiation for 0.1 - 5 s. The IRPD rate constants from laser irradiation are corrected for frequency dependent variations in laser power as well as dissociation due to BIRD.[47]

For double resonance experiments, a single-frequency excitation matching the cyclotron frequency of the ion to be ejected is continuously applied to the cell after isolation of the precursor and is sustained until just before ion detection. Ions were photodissociated for 2.5 s at 3521 cm^{-1} to produce significant abundances of fragment ions.

2.2.3 Calculations

Structures of $Fe(CN)_6^{3-}(H_2O)_8$ were generated by initially positioning water molecules around the ion in Macromodel 9.1 (Schrödinger, Inc., Portland, OR). The structures were geometry optimized using Q-Chem 4.0[48] (Q-Chem, Inc., Pittsburgh, PA) at B3LYP/LACVP++** level of theory prior to vibrational frequency and intensity calculations at the same level of theory. Vibrational frequencies were scaled by 0.955 and convolved with a 60 and 15 cm^{-1} fwhm Gaussian for the $3000 - 3650$ cm^{-1} and $3650 - 3800$ cm^{-1} regions, respectively.[49] Zero-point energies, enthalpy, and entropy corrections at 133 K were calculated for these structures using unscaled B3LYP/LACVP++** harmonic oscillator vibrational frequencies. Additional optimizations were performed at the MP2 level with the VTZ basis set, and zero point energies, enthalpy, and entropy corrections were obtained using frequencies and thermochemical parameters from B3LYP/LACVP++**.

2.3 Results and Discussion

2.3.1 Hydrated Ion Formation

Mass spectra obtained by nESI of 5 mM aqueous solutions of $K_3Fe(CN)_6$ (Figure 2.1) show abundant hydrated ferricyanide trianions, $Fe(CN)_6^{3-}(H_2O)_n$, with n between 8 and ∼350 water molecules. The distribution of hydrated ions can be shifted from smaller (Figure 2.1a) to larger (Figure 2.1b) cluster sizes by decreasing the temperature of the entrance capillary, reducing electrostatic potentials applied to source optics, and modifying the excitation waveforms to optimize ion detection in the m/z range of interest. Cluster sizes with $n > 350$ can be formed using even softer conditions. Other ions present in Figure 2.1a include $Fe(CN)_6^{2-}(H_2O)_n$ with $n = 0 - 8$, $HFe(CN)_6^{2-}(H_2O)_n$ with $n = 0 - 22$, $KFe(CN)_6^{2-}(H_2O)_n$ with $n = 0 - 24$, $Fe(CN)_5^{2-}$, $Fe(CN)_4^{2-}$ and $Fe(CN)_3^{-}$.

Formation of the bare gaseous trianions, trimetaphosphate ($P_3O_9^{3-}$) and hexanitrocobaltate ($Co(NO_2)_6^{3-}$), has been reported previously.[44] Under the same conditions used to form the hydrated ferricyanide trianions (Figure 2.1), these other two trianions are not formed as bare species. nESI of a 5 mM aqueous solution of $Na_3P_3O_9$ results in the formation of the trianions, $P_3O_9^{3-}(H_2O)_n$ with $n \geq 6$ (Figure A.1). Isolation of the $P_3O_9^{3-}(H_2O)_9$ cluster (Figure A.2a) and IRPD at 3438 cm^{-1} for 60 s results in fragments corresponding to sequential water molecule loss to $P_3O_9^{3-}(H_2O)_6$ followed by a charge-separation reaction to form $HP_3O_9^{2-}(H_2O)_5$ and subsequent sequential water molecule loss to form $HP_3O_9^{2-}(H_2O)_{1-4}$ (Figure A.2b). Although there is a peak in the nESI spectrum at $m/z = 78.96$, which corresponds to that of the bare trianion, the isotope distribution shows that this ion is the dianionic species, $P_2O_6^{2-}$.

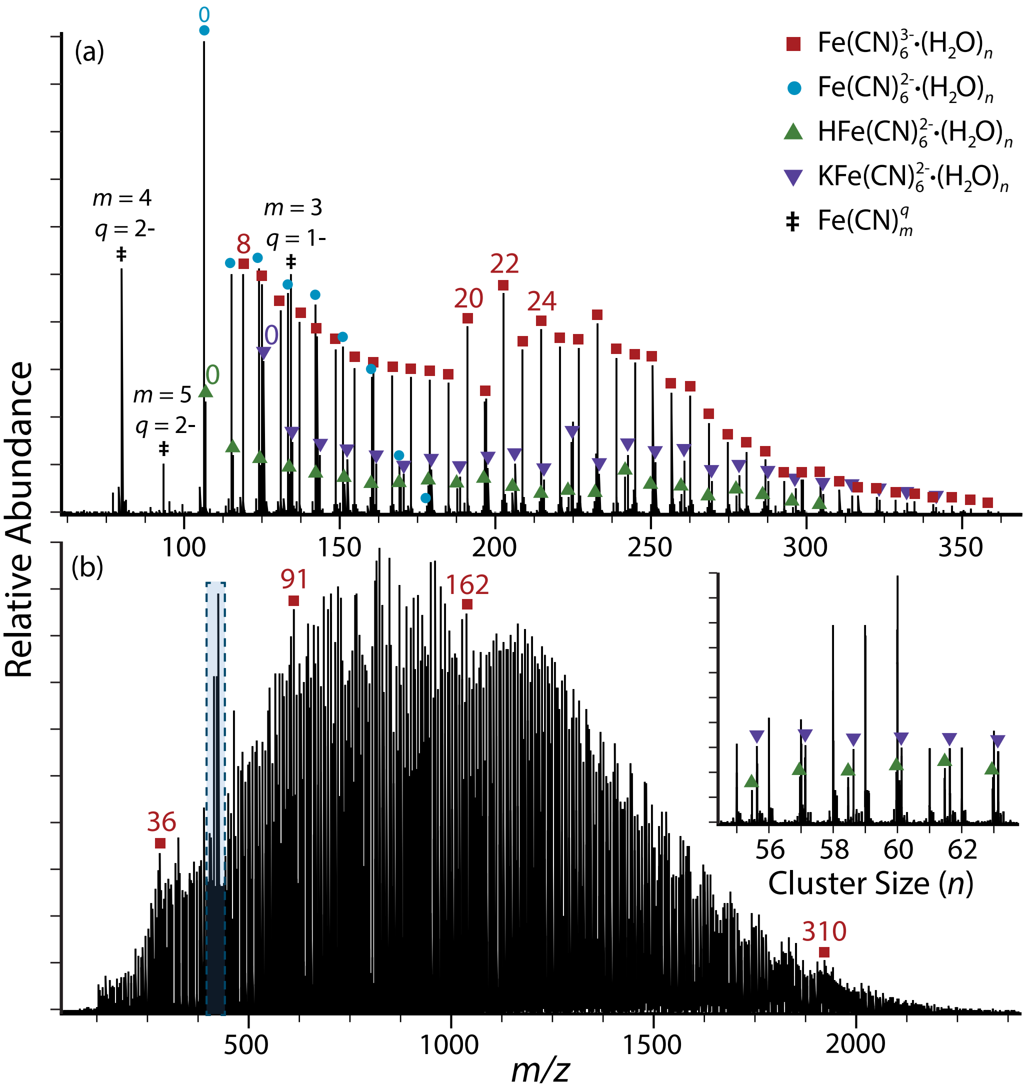

Figure 2.1: nESI mass spectra obtained from 5 mM aqueous solution of $K_3Fe(CN)_6$ showing formation of $Fe(CN)_6^{3-}\cdot(H_2O)_n$, with n between 8 and ~350 under (a) more energetic instrumental conditions to form smaller cluster sizes and (b) soft instrumental conditions to form larger cluster sizes. Inset shows magic number clusters corresponding to $Fe(CN)_6^{3-}\cdot(H_2O)_{58-60}$.

These experiments provide compelling evidence that $P_3O_9^{3-}$ is not stable in the gas phase as an isolated ion and likely only exists as a long-lived stable ion with ~6 or more water molecules attached. Similarly, nESI of a 5 mM aqueous solution of $Na_3Co(NO_2)_6$ results in formation of $Co(NO_2)_3^{1-}(H_2O)_n$, $NO_3^{1-}(H_2O)_n$, and $NO_2^{1-}(H_2O)_n$ (Figure A.3). We conclude from these experiments that $Fe(CN)_6^{3-}(H_2O)_n$ and $P_3O_9^{3-}(H_2O)_n$ with $n \geq 6$ are the smallest, most highly charged trianions that have been observed to date.

2.3.2 Dissociation Pathways

$Fe(CN)_6^{3-}(H_2O)_8$ is the smallest trianion cluster in the nESI mass spectra obtained using a variety of instrumental conditions. BIRD of $Fe(CN)_6^{3-}(H_2O)_8$ at 133 K for 60 s does not result in observable water loss from the precursor to form $Fe(CN)_6^{3-}(H_2O)_7$ (Figure 2.2). Instead, there is a product ion corresponding to loss of an electron, $Fe(CN)_6^{2-}(H_2O)_8$ (Reaction 2.1):

$$Fe(CN)_6^{3-}(H_2O)_8 \longrightarrow Fe(CN)_6^{2-}(H_2O)_8 + e^- \qquad \text{(Reaction 2.1)}$$

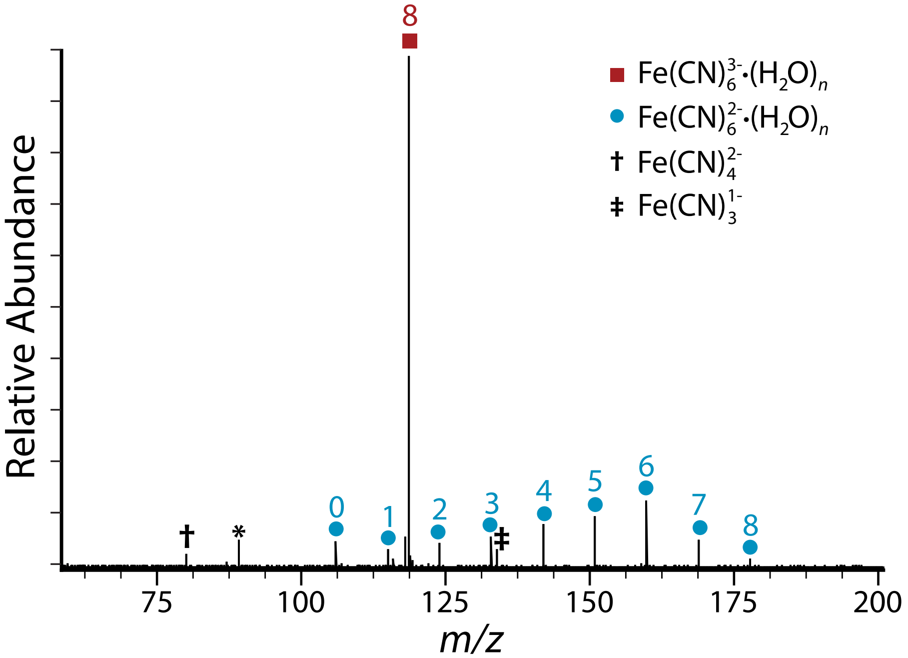

Figure 2.2: Blackbody infrared radiative dissociation mass spectrum of $Fe(CN)_6^{3-}\cdot(H_2O)_8$ at 133 K for 60 s. Frequency noise is labeled with an asterisk (∗).

Auto-detachment of an electron was also reported for the following ions: the 3− and 4− charge states of oligonucleotides,[21] sulfonated pyrene trianion,[22] metal phthalocyanine-tetrasulfonate tetraanions,[23] and C_{70}^{2-}.[2] $Fe(CN)_6^{2-}(H_2O)_n$ with $n = 0 - 7$ and ions corresponding to ligand loss, $Fe(CN)_4^{2-}$ and $Fe(CN)_3^-$, are also formed by BIRD (Figure 2.2). Because these complexes are not hydrated, it is likely that the instability of the bare dianion leads to further dissociation through consecutive cyano ligand loss (Reactions 2.2a and 2.2b). Although $Fe(CN)_5^{2-}$ is not observed with BIRD of $Fe(CN)_6^{3-}(H_2O)_8$, it appears in the electrospray mass spectrum (Figure 2.1a) but in significantly lower abundance than the other two complexes. This indicates that this ion is not very stable or that $Fe(CN)_6^{2-}$ dissociates primarily by loss of $(CN)_2$ to form $Fe(CN)_4^{2-}$, which may occur due to the high enthalpy of formation for $(CN)_2$.[50] $Fe(CN)_4^{2-}$ undergoes a charge-separation reaction to produce $Fe(CN)_3^-$ and CN^- (Reaction 2c). The high electron affinity of CN (3.862 eV)[51] likely accounts for the facile formation of CN^-.

$$Fe(CN)_6^{2-} \longrightarrow Fe(CN)_5^{2-} + \ CN \qquad \text{(Reaction 2.2a)}$$

$$Fe(CN)_5^{2-} \longrightarrow Fe(CN)_4^{2-} + \ CN \qquad \text{(Reaction 2.2b)}$$

$$Fe(CN)_4^{2-} \longrightarrow Fe(CN)_3^{1-} + \ CN^- \qquad \text{(Reaction 2.2c)}$$

In order to further elucidate the dissociation pathways of small hydrated trianion ferricyanide, double resonance experiments were performed for $Fe(CN)_6^{3-}(H_2O)_{10}$ (Figure 2.3). In these experiments, IRPD at 3521 cm^{-1}, which corresponds to a hydrogen-bonded absorption, is used to vibrationally excite the ions, during which time a single radio frequency excitation at the resonant cyclotron frequency of a possible intermediate in the reaction pathway is applied. Any product ions originating from the continuously ejected ion should not be observed in the mass spectrum if the time scale for formation is longer than the ~10 µs ejection time.

IRPD of isolated $Fe(CN)_6^{3-}(H_2O)_{10}$ for 2.5 s (Figure 2.3a) results in formation of $Fe(CN)_6^{3-}(H_2O)_{7-9}$ and $Fe(CN)_6^{2-}(H_2O)_{3-7}$ (Figure 2.3b). The appearance of $Fe(CN)_6^{3-}(H_2O)_7$ with IRPD, which is not observed in the lower energy BIRD experiment, indicates that the loss of one water molecule from $Fe(CN)_6^{3-}(H_2O)_8$ is entropically favored over loss of an electron.

Results from a double resonance experiment in which $Fe(CN)_6^{2-}(H_2O)_6$ is continuously ejected is shown in Figure 2.3c. Both this ion and all the smaller dianions are absent. This demonstrates that $Fe(CN)_6^{2-}(H_2O)_{3-5}$ are formed by sequential water loss from $Fe(CN)_6^{2-}(H_2O)_6$ (Reaction 2.3):

$$Fe(CN)_6^{2-}(H_2O)_n \longrightarrow Fe(CN)_6^{2-}(H_2O)_{n-1} + H_2O \qquad \text{(Reaction 2.3)}$$

Continuous ejection of $Fe(CN)_6^{3-}(H_2O)_7$ (Figure 2.3d) results in the elimination of all dianion products. This suggests that loss of an electron from $Fe(CN)_6^{3-}(H_2O)_n$ with $n > 7$ contributes negligibly to the formation of hydrated dianions under these more energetic dissociation conditions.

When $Fe(CN)_6^{2-}(H_2O)_7$ is continuously ejected from the cell, some $Fe(CN)_6^{2-}(H_2O)_{3-6}$ still remain (Figure 2.3e). This indicates that there is a second dissociation pathway for $Fe(CN)_6^{3-}(H_2O)_7$. To form the $n = 6$ dianion without water loss from the $n = 7$ dianion, electron ejection must occur from $Fe(CN)_6^{3-}(H_2O)_6$, which must have a lifetime that is shorter than the time required for detection in these experiments. These results indicate that the smallest observed hydrate of ferricyanide, $Fe(CN)_6^{3-}(H_2O)_7$, can dissociate *via* two pathways, either by loss of a neutral water molecule (Reaction 2.4a) or by loss of an electron (Reaction 2.4b):

$$Fe(CN)_6^{3-}(H_2O)_7 \longrightarrow Fe(CN)_6^{3-}(H_2O)_6 + H_2O \qquad \text{(Reaction 2.4a)}$$

$$Fe(CN)_6^{3-}(H_2O)_7 \longrightarrow Fe(CN)_6^{2-}(H_2O)_7 + e^- \qquad \text{(Reaction 2.4b)}$$

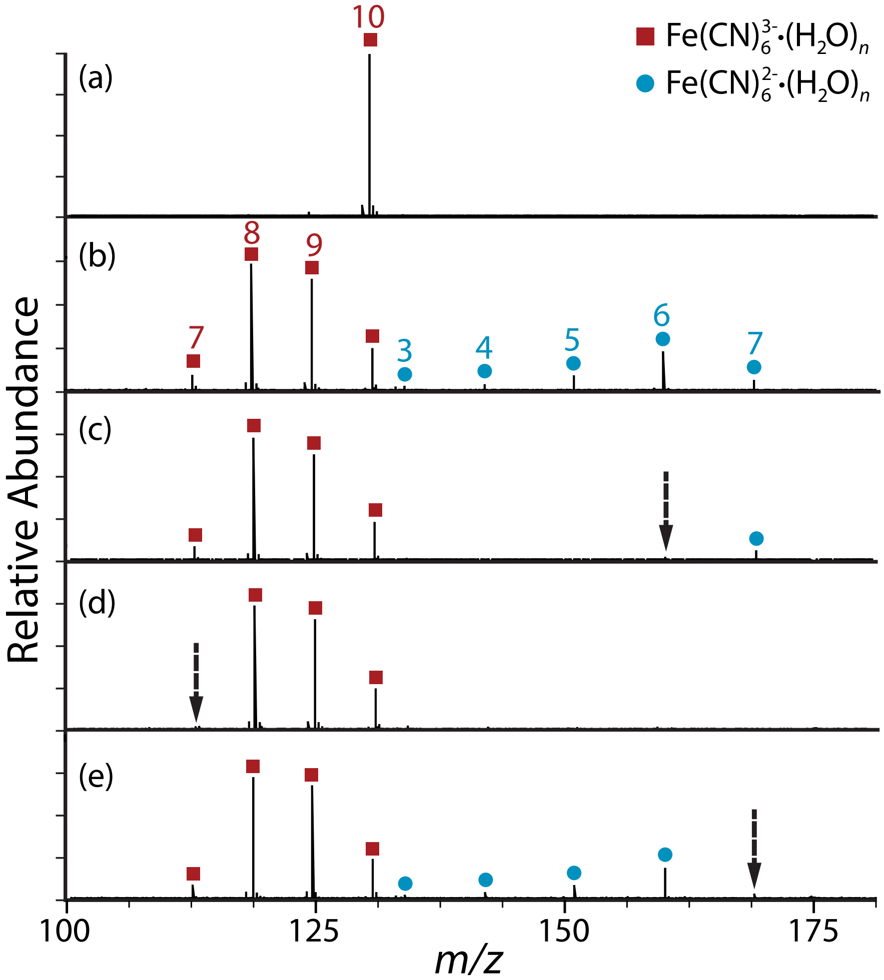

Figure 2.3: IRPD dissociation and double resonance data on $Fe(CN)_6^{3-}\cdot(H_2O)_{10}$ showing (a) isolated precursor, $Fe(CN)_6^{3-}\cdot(H_2O)_{10}$, (b) IRPD of $Fe(CN)_6^{3-}\cdot(H_2O)_{10}$ at 3521 cm^{-1} for 2.5 s with double resonance ejection of possible intermediates corresponding to (c) $Fe(CN)_6^{2-}\cdot(H_2O)_6$, (d) $Fe(CN)_6^{3-}\cdot(H_2O)_7$, and (e) $Fe(CN)_6^{2-}\cdot(H_2O)_7$. Dotted arrows indicate the m/z corresponding to the frequency excited during the experiment.

$Fe(CN)_6^{3-}(H_2O)_8$ is the smallest cluster observed in the nESI mass spectra. The absence of $Fe(CN)_6^{3-}(H_2O)_7$ in the BIRD spectrum of $Fe(CN)_6^{3-}(H_2O)_8$ indicates that the lowest energy dissociation process for this ion is loss of an electron. Sequential loss of water molecules as well as electron loss from the smaller clusters occurs with the higher energy activation conditions of the IRPD experiments. This indicates that although smaller trianion clusters may be formed under even higher energy activation conditions, $n = 8$ is the “critical” size where charge separation occurs and appears to be energetically favored over the loss of a water molecule.

2.3.3 Infrared Photodissociation Spectroscopy of $\mathbf{Fe(CN)_6^{3-}(H_2O)_8}$

In order to gain insight into the structure of $Fe(CN)_6^{3-}(H_2O)_8$, the smallest trianion formed directly by nESI, an IRPD spectrum in the hydrogen oscillator region from $3100 - 3800$ cm^{-1} was obtained (Figure 2.4a). The vibrational modes for the O–H stretch of water are sensitive to the local hydrogen-bonding environment and can provide information about how water molecules organize around the ion.

The IRPD spectrum of $Fe(CN)_6^{3-}(H_2O)_8$ (Figure 2.4a) has a broad band that appears to be comprised of at least two separate absorption bands centered at 3471 and 3505 cm^{-1}. Two low intensity absorptions at 3150 and 3270 cm^{-1} are within baseline noise in this region of the spectrum, where both the laser power and photon energy are lower. This region of the spectrum corresponds to bonded O–H stretches indicative of water molecules that donate a hydrogen bond to another atom. There is no peak in the free O–H region, which indicates that both of the hydrogen atoms for all eight water molecules are hydrogen-bonded either to $Fe(CN)_6^{3-}$ or to other water molecules.

Calculated low energy structures and corresponding IR spectra for $Fe(CN)_6^{3-}(H_2O)_8$ are shown in Figure 2.4 (**4b** - **4g**). The lowest energy structure, **4b**, has four pairs of water molecules that bridge between three cyano ligands. One water molecule in the pair hydrogen bonds to a cyano group and to the oxygen atom of an adjacent water molecule (double donor, or DD, water molecule). This adjacent water molecule hydrogen bonds directly to two cyano groups and accepts one hydrogen bond from the paired water molecule (acceptor-donor-donor, or ADD, water molecule). Structure **4b** contains four of these pairs of water molecules, whereas structure **4c** (+9.6/+4.9 kJ/mol with B3LYP/MP2 energies, respectively) has three of these pairs and two water molecules that bond to two cyano groups (DD). The spectra for **4b** and **4c** have bonded O–H stretches between $\sim 3350 - 3650$ cm^{-1}, which match well with the experimental spectrum.

Structures **4d** and **4e** are higher energy structures that share the same structural motif in that each water molecule donates two hydrogen bonds to nitrogen atoms of adjacent cyano ligands. These structures have no water-water hydrogen bonds. The calculated spectra have two bonded O–H bands corresponding to symmetric/asymmetric vibrations at 3527/3625 and 3541/3606 cm^{-1} for **4d** and **4e**, respectively. These stretches are blue-shifted from those in the experimental spectrum. In addition, these structures are > 18 kJ/mol higher in energy (structure **4d** converged to a different structure at the MP2/VTZ level, **4h** (Figure A.4), which has a free O–H stretch and is 14.3 kJ/mol higher in energy), indicating that these isomers are not present.

Some CN ligands in structure **4f** ($>+10.1$ kJ/mol) are involved in a single hydrogen bond to just one water molecule, and two water molecules have a free O–H stretch. There is no free O–H stretch in the IRPD spectrum, although this is not calculated to be an intense feature. A structure in which water forms two rings, **4g**, is not energetically favorable ($>+50$ kJ/mol) and should have a free O–H stretch band at 3697 cm^{-1} that is not observed experimentally. Based on comparisons between the calculated spectra and the measured IRPD spectrum

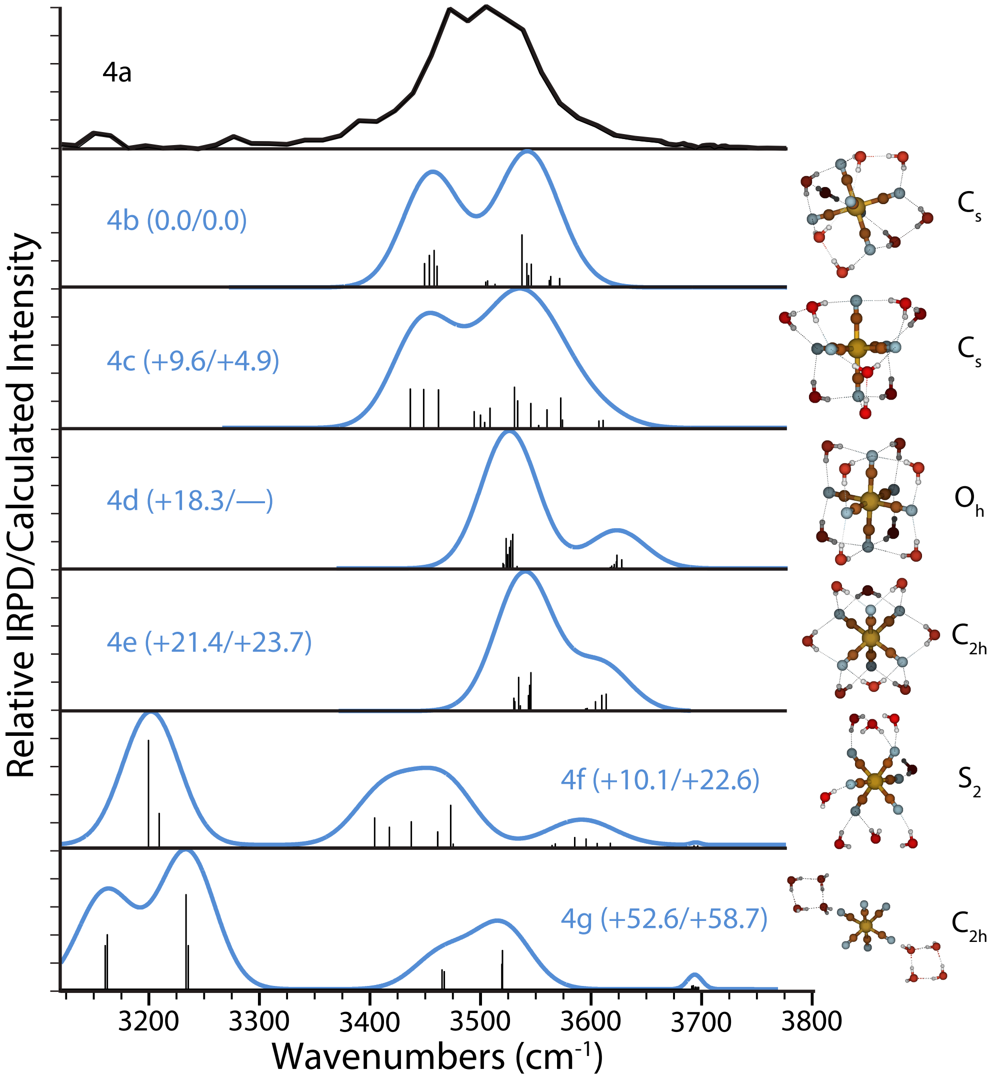

Figure 2.4: Spectra of $Fe(CN)_6^{3-}\cdot(H_2O)_8$. (a) IRPD spectrum and (b–g) calculated spectra and corresponding optimized structures calculated at the B3LYP/LACVP++** level. Gibbs free energies (in kJ/mol at 133 K) relative to the lowest-energy structure **4b** are inset with values from B3LYP/MP2. Point groups for calculated structures are provided on the right.

as well as the computed energies, structures **4b** and **4c** are likely to be the predominant structures in these experiments.

The CN ligands in both structures **4b** and **4c** each interact with at least two water molecules. Removal of a single water molecule from either structure results in a CN ligand that accepts a hydrogen bond from just one water molecule. Such a structure is not energetically favorable to form under the low energy conditions of nESI or dissociation by BIRD, but can be formed by more energetic activation of larger clusters.

2.3.4 Magic Number Clusters

The abundance of a cluster depends on its stability as well as the stabilities of larger clusters. Clusters with anomalously high abundances are commonly referred to as magic number clusters. For $Fe(CN)_6^{3-}(H_2O)_n$, n between 58 and 60 are magic number clusters (Figure 2.1b) and, to a lesser extent, $n = 20$ and 22 also are as well (Figure 2.1a).

To determine if the high abundances of the larger magic number clusters are associated with high ion stabilities or exceptional instability in the $n+1$ clusters, BIRD dissociation constants were measured for $n = 56 - 62$. The BIRD rate constant for $n = 60$ ($k_{BIRD} = 0.088s^{-1}$) is significantly lower than that for $n = 61$ ($k_{BIRD} = 0.36s^{-1}$) or $n = 62$ ($k_{BIRD} = 0.49s^{-1}$). This suggests a stable core structure is established for $n = 60$, and that additional water molecules do not bind strongly to or disturb this core structure. Magic number clusters around this size have also been reported for $(H_2O)_n^-$ and $H^+(H_2O)_n$ for alternating cluster sizes,[43,52–54] whereas ferricyanide has three successive clusters with higher abundance.

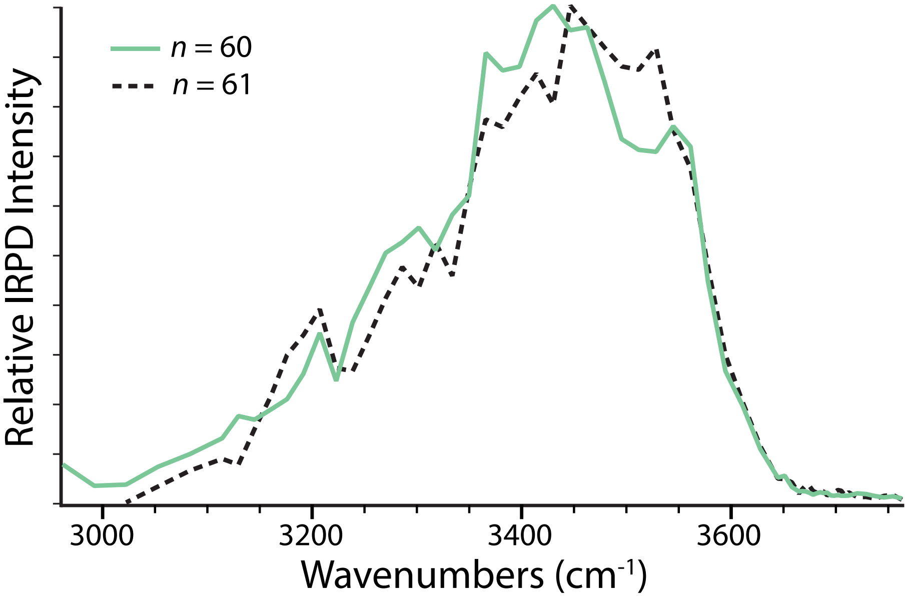

Figure 2.5: IRPD spectra of $Fe(CN)_6^{3-}\cdot(H_2O)_n$ $n = 60$ (solid green) and 61 (dotted black).

In order to gain further insight into the unusual stabilities of these ions, an IRPD spectrum of $Fe(CN)_6^{3-}(H_2O)_{60}$ was compared to that of the significantly less stable $Fe(CN)_6^{3-}$-$(H_2O)_{61}$ (Figure 2.5). The bonded O–H region of the $n = 60$ cluster has a broad peak centered at 3438 cm^{-1} with an apparent shoulder at ~3550 cm^{-1}. The maximum of this absorption is at a slightly higher frequency for the $n = 61$ cluster. The red shift in the spectrum for the $n = 60$ cluster is indicative of stronger, more optimal hydrogen bonding and is consistent with the higher stability of this cluster. The shoulder at ~3550 cm^{-1} has previously been attributed to three-coordinate ADD water molecules for some clusters.[55–59] There is a strong ADD stretch in the spectra of $Cs^+(H_2O)_{20}$ and some other alkali metal ions that is indicative of clathrate structures.[58,60] This band in $Fe(CN)_6^{3-}(H_2O)_{60}$ may indicate the possibility of similar complex cage-like structures. Remarkably, there is not a free O–H band in the IRPD spectra of either cluster indicating that the hydrogen atoms in essentially all of the water molecules participate in hydrogen bonding for these two clusters.

2.3.5 Patterning of Water Molecules at Long Distances

A free O–H band is commonly observed in the spectra of hydrated ions. For cations, a free O–H band is observed from the onset of hydration, whereas for anions, this band is often only seen in the spectra of larger clusters as a result of the orientation of water molecules that interact directly with the anion. To investigate the extent to which the ferricyanide trianion affects the hydrogen-bonding network of water molecules at larger cluster size, IRPD spectra of $Fe(CN)_6^{3-}(H_2O)_n$ with n between 20 and 120 water molecules were measured at select cluster sizes (Figure 2.6). There is a broad band in the spectra between ~3200 and 3600 cm^{-1}, with a maximum that blue shifts from 3521 cm^{-1} for $n = 20$ to 3422 cm^{-1} for $n = 120$. The absorption band of liquid water is centered at ~3400 cm^{-1}.[61] This suggests that the fully hydrogen-bonded water molecules in the larger ferricyanide trianion-containing clusters are in an environment similar to that in liquid water or amorphous ice.

There is no band in the free O–H region in the smaller clusters of $Fe(CN)_6^{3-}(H_2O)_n$, indicating that all the hydrogen atoms of water are involved in hydrogen bonds. At $n = 70$, a feature at 3707 cm^{-1} emerges, indicating the presence of water molecules with a free O–H. The intensity of this band increases with cluster size, indicating the presence of additional water molecules that have a free O–H. The frequency of this band corresponds to water molecules that are at the surface of the cluster and accept two hydrogen bonds and donate a single hydrogen bond (acceptor-acceptor-donor, or AAD, water molecules).[57–60,62–64] This frequency depends on the charge state of the ion, the cluster size, and to a lesser extent, the size of the ion in the cluster. Results for 1− to 3+ charge state ions at $n \simeq 36$, and for 2− to 3+ ions at $n \simeq 250$, indicate that the frequency of this stretch is affected by the electric field at the nanodrop surface, *i.e.*, a Stark shift, that is induced both by the charge of the ion in the cluster and by the surface potential that is caused by the net orientation of water molecules at the surface of the cluster.[65,66] This frequency also depends on the orientation of the free O–H of the water molecules at the surface.

There is a free O–H stretch for $I^-(H_2O)_n$ clusters that persists for $n > 5$.[67] In contrast, a free O–H band does not appear in the spectrum of $(H_2O)_n^-$ until $n \geq 15$[68] and until $n > 43$ for $SO_4^{2-}(H_2O)_n$.[69] The appearance of the free O–H stretch at much larger cluster sizes for SO_4^{2-} is consistent with a stronger orientation of water molecules induced by these ions as a result of the higher charge state and the formation of hydrogen bonds directly to the ion or to both the ion and to other water molecules.[70] The absence of a free O–H stretch until $n > 43$ indicates that the ion-induced effect on water orientation in the first solvation shell

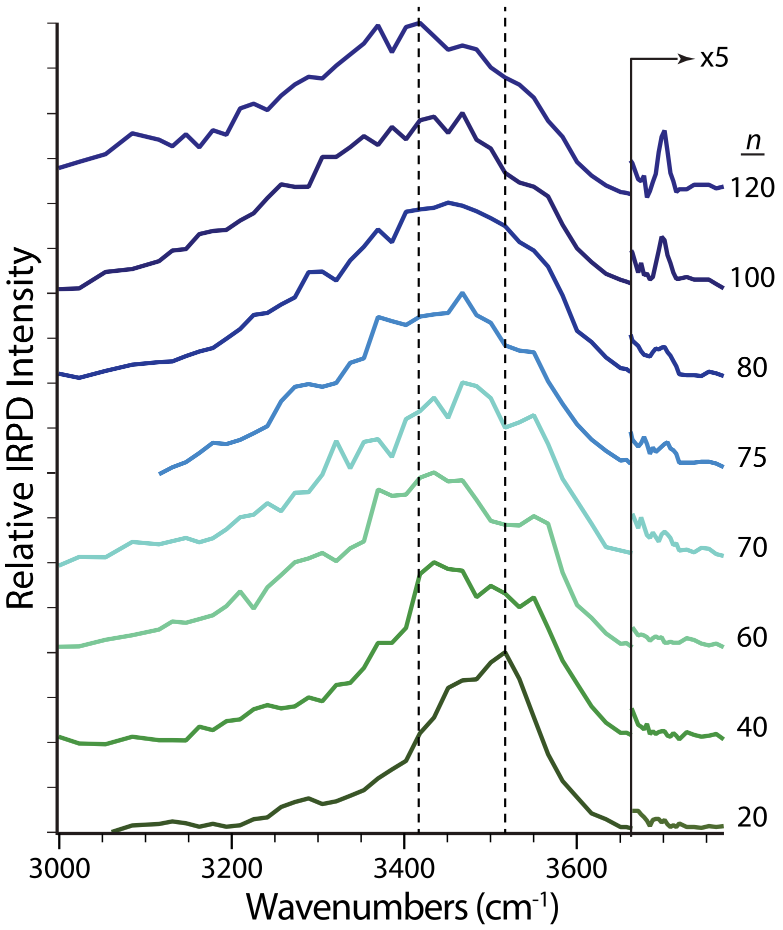

Figure 2.6: IRPD spectra of $\mathrm{Fe(CN)}_6^{3-}\cdot(\mathrm{H_2O})_n$ with n between 20 and 120. The free O–H region has been expanded by 5× to more clearly show the band at $\sim$3700 cm^{-1} corresponding to acceptor-acceptor-donor water molecules at the surface of these clusters.

propagates outwards into the second and even third solvation shells. This is consistent with IRPD spectroscopy of even larger SO_4^{2-} clusters that show differences in hydrogen bonding of fully hydrogen bonded water molecules even for clusters with $n \simeq 250$.[66] For $\mathrm{Fe(CN)}_6^{3-}$, the absence of the free O–H stretch for clusters with $n < 70$ shows that this ion can orient water molecules even more strongly than SO_4^{2-} and can affect the hydrogen bonding network of water molecules as far as the fourth solvation shell.

2.4 Conclusions

Formation of small hydrated trianions, $\mathrm{Fe(CN)}_6^{3-}(\mathrm{H_2O})_n$ with $n \geq 8$, direcly by nESI is demonstrated. $\mathrm{Fe(CN)}_6^{3-}$ is the smallest, highest charge density trianion that has been observed in the gas phase, and information about the structures and reactivities of these ions provide new insights into the role of water in stabilizing small multivalent anions. $Fe(CN)_6^{3-}(H_2O)_8$ dissociates by loss of an electron with BIRD. No $Fe(CN)_6^{3-}(H_2O)_7$ is observed, consistent with the absence of this and smaller hydrated trianions in the nESI mass spectra. In contrast, $Fe(CN)_6^{3-}(H_2O)_7$ is formed under the higher energy activation conditions of IRPD, and this ion dissociates by two pathways corresponding to either loss of a water molecule or loss of an electron. The IRPD spectrum of $Fe(CN)_6^{3-}(H_2O)_8$ is consistent with computed structures in which pairs of water molecules form two hydrogen bonds directly to the ion or form one hydrogen bond to the ion and one to the other water molecule.

There are magic number clusters at $n = 58 - 60$ and the IRPD spectrum of the $n = 60$ cluster shows that the hydrogen atoms of all the water molecules are involved in hydrogen bonds and that these hydrogen bonds are, on average, stronger than those in the $n = 61$ cluster, which is significantly less stable. Remarkably, the IRPD spectra of these ions do not have a feature corresponding to a free O–H stretch indicating that the hydrogen atoms of all the water molecules, even those at the surface of the cluster, are involved in hydrogen bonds. IRPD spectra measured for clusters with up to 120 water molecules indicate the onset of a free O–H stretch of an acceptor-acceptor-donor water molecule at the surface of the cluster occurs at $n \simeq 70$, which corresponds to a droplet radius of $\sim$0.8 nm. These results provide compelling evidence that this trivalent ion orients water and patterns the hydrogen-bonding network of the water molecules all the way to the surface of the clusters, even for water molecules that are surrounded by other water molecules and that are not on the surface nor directly interact with the ion. These clusters are cold (133 K), and the thermal motion of water molecules is much lower than that at room temperature. Consequently, the water orientation effects of the ion will be less in liquid water. However, the forces that cause the patterning of water at low temperature still exist at higher temperature and must still influence the hydrogen bonding network of liquid water to some extent. These forces extend well past the first solvation shell and may play a role in Hofmeister and other ion-related phenomenon.

Charge separation by loss of an electron from these trianions may also provide insight into why charging of many proteins and other macromolecules is less for anions than it is for cations in electrospray ionization. Loss of electrons may also occur for much larger charged droplets as solvent evaporation causes the droplets to approach the Rayleigh limit. Ejection of cationic species through an ion evaporation mechanism can occur from positively charged droplets as can loss of anionic species from anionic droplets, and these ion evaporation processes may affect charging of macromolecules.[71] Although many factors contribute to charging of macromolecules in electrospray ionization, electron loss, which would only occur significantly for anionic droplets, could result in a slightly lower charge density at the surface of anionic drops than cationic drops, and may contribute to the lower charging of many macromolecules formed as anions in ESI.

2.5 References

[1] Boldyrev, A. I.; Gutowski, M.; Simons, J. *Acc. Chem. Res.* **1996**, *29*, 497–502.

[2] Hampe, O.; Neumaier, M.; Blom, M. N.; Kappes, M. M. *Chem. Phys. Lett.* **2002**, *354*, 303–309.

[3] Petrie, S.; Wang, J.; Böhme, D. K. *Chem. Phys. Lett.* **1993**, *204*, 473–480.

[4] Williams, E. R. *J. Mass Spectrom.* **1996**, *31*, 831–842.

[5] Yoo, H. J.; Wang, N.; Zhuang, S.; Song, H.; Håkansson, K. *J. Am. Chem. Soc.* **2011**, *133*, 16790–16793.

[6] Wang, X. B.; Wang, L. S. *Annu. Rev. Phys. Chem.* **2009**, *60*, 105–126.

[7] Puškar, L.; Tomlins, K.; Duncombe, B.; Cox, H.; Stace, A. J. *J. Am. Chem. Soc.* **2005**, *127*, 7559–7569.

[8] Blades, A. T.; Jayaweera, P.; Ikonomou, M. G.; Kebarle, P. *Int. J. Mass. Spectrom. Ion Processes* **1990**, *102*, 251–267.

[9] Shvartsburg, A. A.; Siu, K. W. M. *J. Am. Chem. Soc.* **2001**, *123*, 10071–10075.

[10] Bush, M. F.; Saykally, R. J.; Williams, E. R. *Int. J. Mass. Spectrom.* **2006**, *253*, 256–262.

[11] McQuinn, K.; Hof, F.; McIndoe, J. S. *Chem. Commun.* **2007**, *40*, 4099–4101.

[12] Gross, D. S.; Rodriguez-Cruz, S. E.; Bock, S.; Williams, E. R. *J. Phys. Chem.* **1995**, *99*, 4034–4038.

[13] Feil, S.; Koyanagi, G. K.; Böhme, D. K. *Int. J. Mass. Spectrom.* **2009**, *280*, 38–41.

[14] Spears, K. G.; Fehsenfeld, F. C. *J. Chem. Phys.* **1972**, *56*, 5698–5705.

[15] Spears, K. G.; Fehsenfeld, G. C.; McFarland, M.; Ferguson, E. E. *J. Chem. Phys.* **1972**, *56*, 2562–2566.

[16] Beyer, M.; Williams, E. R.; Bondybey, V. E. *J. Am. Chem. Soc.* **1999**, *121*, 1565–1573.

[17] Stace, A. J. *J. Phys. Chem. A* **2002**, *106*, 7993–8005.

[18] Roithová, J.; Schwarz, H.; Schröder, D. *Chem. Eur. J.* **2009**, *15*, 9995–9999.

[19] Schröder, D.; Schwarz, H. *J. Phys. Chem. A* **1999**, *103*, 7358–7394.

[20] Boxford, W. E.; Dessent, C. E. H. *Phys. Chem. Chem. Phys.* **2006**, *8*, 5151–5165.

[21] Danell, A. S.; Parks, J. H. *J. Am. Soc. Mass Spectrom.* **2003**, *14*, 1330–1339.

[22] Wang, X. B.; Sergeeva, A. P.; Xing, X. P.; Massaouti, M.; Karpuschkin, T.; Hampe, O.; Boldyrev, A. I.; Kappes, M. M.; Wang, L. S. *J. Am. Chem. Soc.* **2009**, *131*, 9836–9842.

[23] Arnold, K.; Balaban, T. S.; Blom, M. N.; Ehrler, O. T.; Gilb, S.; Hampe, O.; Lier, J. E.; Weber, J. M.; Kappes, M. M. *J. Phys. Chem. A* **2003**, *107*, 794–803.

[24] Wong, R. L.; Williams, E. R. *J. Phys. Chem. A* **2003**, *107*, 10976–10983.

[25] Blades, A. T.; Kebarle, P. *J. Am. Chem. Soc.* **1994**, *116*, 10761–10766.

[26] Gao, B.; Liu, Z. *J. Chem. Phys.* **2005**, *123*, 224302.

[27] Wang, X. B.; Nicholas, J. B.; Wang, L. S. *J. Chem. Phys.* **2000**, *113*, 10837–10840.

[28] Schauer, S. N.; Williams, P.; Compton, R. N. *Phys. Rev. Lett.* **1990**, *65*, 625–628.

[29] Cooper, T. E.; Armentrout, P. B. *J. Phys. Chem. A* **2009**, *113*, 13742–13751.

[30] Wang, L. S.; Ding, C. F.; Wang, X. B.; Nicholas, J. B. *Phys. Rev. Lett.* **1998**, *81*, 2667–2670.

[31] Blom, M. N.; Hampe, O.; Gilb, S.; Weis, P.; Kappes, M. M. *J. Chem. Phys.* **2001**, *115*, 3690–3697.

[32] Cox, H.; Akibo-Betts, G.; Wright, R.; Walker, N.; Curtis, S.; Duncombe, B.; Stace, A. J. *J. Am. Chem. Soc.* **2003**, *125*, 233–242.

[33] Wright, R.; Walker, N.; Firth, S.; Stace, A. J. *J. Phys. Chem. A* **2001**, *105*, 54–64.

[34] Whitehead, A.; Barrios, R.; Simons, J. *J. Chem. Phys.* **2002**, *116*, 2848–2851.

[35] Schröder, D.; Schwarz, H.; Wu, J.; Wesdemiotis, C. *Chem. Phys. Lett.* **2001**, *343*, 258–264.

[36] Böhme, D. K. *Phys. Chem. Chem. Phys.* **2011**, *13*, 18253–18263.

[37] Kordel, M.; Schooss, D.; Gilb, S.; Blom, M. N.; Hampe, O.; Kappes, M. M. *J. Phys. Chem. A* **2004**, *108*, 4830–4837.

[38] Dau, P. D.; Liu, H. T.; Yang, J. P.; Winghart, M. O.; Wolf, T. J. A.; Unterreiner, A. N.; Weis, P.; Miao, Y. R.; Ning, C. G.; Kappes, M. M.; Wang, L. S. *Phys. Rev. A* **2012**, *85*, 064503.

[39] Wang, X. B.; Yang, X.; Nicholas, J. B.; Wang, L. S. *Science* **2001**, *294*, 1322–1325.

[40] Žabka, J.; Ricketts, C. L.; Schröder, D.; Roithová, J.; Schwarz, H.; Thissen, R.; Dutuit, O.; Price, S. D.; Herman, Z. *J. Phys. Chem. A* **2010**, *114*, 6463–6471.

[41] Xin, Y.; Wang, X. B.; Wang, L. S. *J. Phys. Chem. A* **2002**, *106*, 7607–7616.

[42] Rodrigez-Cruz, S. E.; Klassen, J. S.; Williams, E. R. *J. Am. Soc. Mass Spectrom.* **1999**, *10*, 958–968.

[43] Lee, S.-W.; Freivogel, P.; Schindler, T.; Beauchamp, J. L. *J. Am. Chem. Soc.* **1998**, *120*, 11758–11765.

[44] Zhang, X.; Wanigasekara, E.; Breitbach, Z. S.; Dodbiba, E.; Armstrong, D. W. *Rapid Commun. Mass Spectrom.* **2010**, *24*, 1113–1123.

[45] Bush, M. F.; O'Brien, J. T.; Prell, J. S.; Saykally, R. J.; Williams, E. R. *J. Am. Chem. Soc.* **2007**, *129*, 1612–1622.

[46] Wong, R. L.; Paech, K.; Williams, E. R. *Int. J. Mass. Spectrom.* **2004**, *232*, 59–66.

[47] Prell, J. S.; O'Brien, J. T.; Williams, E. R. *J. Am. Soc. Mass Spectrom.* **2010**, *21*, 800–809.

[48] Shao, Y.; Molnar, L. F.; Jung, Y.; Kussmann, J.; Ochsenfeld, C.; Brown, S. T.; Gilbert, A. T. B.; Slipchenko, L. V.; et al., *Phys. Chem. Chem. Phys.* **2006**, *8*, 3172–3191.

[49] Chang, T. M.; Prell, J. S.; Warrick, E. R.; Williams, E. R. *J. Am. Chem. Soc.* **2012**, *134*, 15805–15813.

[50] Davis, D. D.; Okabe, H. *J. Chem. Phys.* **1968**, *49*, 5526–5531.

[51] Bradforth, S. E.; Kim, E. H.; Arnold, D. W.; Neumark, D. M. *J. Chem. Phys.* **1993**, *98*, 800–810.

[52] Ma, L.; Majer, K.; Chirot, F.; Issendorff, B. v. *J. Chem. Phys.* **2009**, *131*, 144303.

[53] Knapp, M.; Echt, O.; Kreisle, D.; Recknagel, E. *J. Phys. Chem.* **1987**, *91*, 2601–2607.

[54] Kondow, T.; Nagata, T.; Kuchitsu, K. *Z. Phys. D: At., Mol. and Clusters* **1989**, *12*, 291–292.

[55] Gruenloh, C. J.; Carney, J. R.; Arrington, C. A.; Zwier, T. S.; Fredericks, S. Y.; Jordan, K. D. *Science* **1997**, *276*, 1678–1681.

[56] Miyazaki, M.; Fujii, A.; Ebata, T.; Mikami, N. *Science* **2004**, *304*, 1134–1137.

[57] Shin, J. W.; Hammer, N. I.; Diken, E. G.; Johnson, M. A.; Walters, R. S.; Jaeger, T. D.; Duncan, M. A.; Christie, R. A.; Jordan, K. D. *Science* **2004**, *304*, 1137–1140.

[58] Cooper, R. J.; Chang, T. M.; Williams, E. R. *J. Phys. Chem. A* **2013**, *117*, 6571–6579.

[59] Fournier, J. A.; Johnson, C. J.; Wolke, C. T.; Weddle, G. H.; Wolk, A. B.; Johnson, M. A. *Science* **2014**, *344*, 1009–1012.

[60] Fournier, J. A.; Wolke, C. T.; Johnson, C. J.; Johnson, M. A.; Heine, N.; Gewinner, S.; Schöllkopf, W.; Esser, T. K.; Fagiani, M. R.; Knorke, H.; Asmis, K. R. *Proc. Natl. Acad. Sci. USA* **2014**,

[61] Freda, M.; Piluso, A.; Santucci, A.; Sassi, P. *Appl. Spectrosc.* **2005**, *59*, 1155–1159.

[62] Headrick, J. M.; Diken, E. G.; Walters, R. S.; Hammer, N. I.; Christie, R. A.; Cui, J.; Myshakin, E. M.; Duncan, M. A.; Johnson, M. A.; Jordan, K. D. *Science* **2005**, *308*, 1765–1769.

[63] Diken, E. G.; Hammer, N. I.; Johnson, M. A.; Christie, R. A.; Jordan, K. D. *J. Chem. Phys.* **2005**, *123*, 164309.

[64] Walters, R. S.; Pillai, E. D.; Duncan, M. A. *J. Am. Chem. Soc.* **2005**, *127*, 16599–16610.

[65] Prell, J. S.; O'Brien, J. T.; Williams, E. R. *J. Am. Chem. Soc.* **2011**, *133*, 4810–4818.

[66] O'Brien, J. T.; Williams, E. R. *J. Am. Chem. Soc.* **2012**, *134*, 10228–10236.

[67] Ayotte, P.; Bailey, C. G.; Weddle, G. H.; Johnson, M. A. *J. Phys. Chem. A* **1998**, *102*, 2067–3071.

[68] Hammer, N. I.; Roscioli, J. R.; Bopp, J. C.; Headrick, J. M.; Johnson, M. A. *J. Chem. Phys.* **2005**, *123*, 244311.

[69] O'Brien, J. T.; Prell, J. S.; Bush, M. F.; Williams, E. R. *J. Am. Chem. Soc.* **2010**, *132*, 8248–8249.

[70] Bush, M. F.; Saykally, R. J.; Williams, E. R. *J. Am. Chem. Soc.* **2007**, *129*, 2220–2221.

[71] Hogan, C. J.; Carroll, J. A.; Rohrs, H. W.; Biswas, P.; Gross, M. L. *Anal. Chem.* **2009**, *81*, 369–377.

Chapter 3

Nanometer Patterning of Water by Tetraanionic Ferrocyanide Stabilized in Aqueous Nanodrops

This chapter is reproduced with permission from:
Matthew J. DiTucci and Evan R. Williams
"Nanometer Patterning of Water by Tetraanionic Ferrocyanide Stabilized in Aqueous Nanodrops", *Chem. Sci.* **2017**, *8*, 1391–1399.

3.1 Introduction

Multiply charged anions (MCAs) are ubiquitous in the condensed phases where they play important roles in the chemistry of materials and biology. Without stabilizing interactions with other molecules, such as solvents or counterions, small, highly charged anions can be unstable in isolation owing to strong Coulombic repulsion between charges.[1,2] For example, the sulfate dianion constitutes 7.7% of dissolved inorganics in global seawaters and is found in many natural minerals, such as barite ($BaSO_4$), celestine ($SrSO_4$) and anglesite ($PbSO_4$).[3,4] It plays an important role in the anaerobic respiration of sulfate-reducing bacteria, such as *Desulfovibrio gigas*, and in the atmospheric chemistry of aerosol radiative forcing, which has an impact on global climate changes.[5,6] Similarly, the phosphate trianion is stable in basic aqueous solutions and its dianionic conjugate acid acts as a buffer in eukaryotic cells.[7] However, isolated SO_4^{2-} and PO_4^{3-} are metastable and decay by electron ejection with calculated lifetimes of 1.6×10^{-10} s and 1.2×10^{-14} s, respectively.[8,9]

The stabilities of MCAs within a given charge state generally increase with molecular size due to a greater separation between charges. Excess electrons in MCAs can be bound by a repulsive coulomb barrier, which manifests as a result of the constructive potentials from short-range electron-nucleus attraction and long-range electron-electron repulsion.[10–12] For dicarboxylate dianions, $^{-}O_2C(CH_2)_xCO_2^{-}$, the electron affinity lessens with decreasing x due to an increase in the repulsive electron-electron potential.[13] The electron affinity is negative for $x \leq 2$ (~5.2 Å). As a result, many large MCAs, such as fullerenes,[14,15] peptides,[16] proteins,[17] and DNA[18,19] are stable as isolated ions, whereas many small MCAs are not.

Small MCAs can be stabilized by interactions with solvent molecules.[20] High-valency anions in solvated clusters can be generated via electrospray ionization,[20–22] which provides a useful method for studying the role of solvation in the stabilities of MCAs as well as the distal extent of ion-water interactions. Wang and co-workers used photoelectron spectroscopy to investigate hydrated sulfate, $SO_4^{2-}(H_2O)_n$, and oxalate, $C_2O_4^{2-}(H_2O)_n$, clusters, which both require solvation by at least three water molecules to be thermodynamically stable.[23,24] Extrapolation of experimental data suggests $SO_4^{2-}(H_2O)_n$ with $n = 1,2$ are unstable by -0.9 and -0.2 eV, respectively.[20] However, formation of $SO_4^{2-}(H_2O)_2$ via collisionally-induced dissociation from $n = 4$ has been reported by Blades and Kebarle suggesting the cluster has a sufficient lifetime to be observed using mass spectrometry.[25]

The primary dissociative pathway for ion-containing clusters depends on the identity of the solvated ion, the cluster size and the internal energy of the cluster. For example, blackbody infrared radiative dissociation (BIRD) of $SO_4^{2-}(H_2O)_n$ at 21 °C with $n \leq 5$ predominately results in charge separation to form $OH^-(H_2O)_k$ and $HSO_4^-(H_2O)_{n-k-1}$ product ions.[26] However, loss of a water molecule is entropically favored, and as a result, $SO_4^{2-}(H_2O)_n$ clusters with $n < 5$ become dominant products under higher energy activation conditions. For this reason, a critical cluster size, n_c, has been defined as the size at which charge separation becomes energetically favored over the loss of a water molecule.[27] Recent results show hydrates of the ferricyanide trianion, $Fe(CN)_6^{3-}(H_2O)_n$, are unstable to electron ejection with a critical cluster size of $n_c = 8$, which IRPD spectroscopy and theory show is still within the first solvation shell of the ion.[21] Although isolated $P_3O_9^{3-}$ and $Co(NO_2)_6^{3-}$ have been reported previously,[28] subsequent experiments show $n_c = 6$ is required to stabilize $P_3O_9^{3-}$ with respect to charge separation and no evidence for isolated $Co(NO_2)_6^{3-}$ was found under identical experimental conditions for forming $P_3O_9^{3-}(H_2O)_n$ and $Fe(CN)_6^{3-}(H_2O)_n$.[21] Therefore, $Fe(CN)_6^{3-}$ and $P_3O_9^{3-}$ are the only small, high-charge density trianions that have been observed in gas phase aqueous clusters and at minimum require first-shell hydration for thermodynamic stability.

The distance to which ion-induced solvent orientation can extend has been studied in solution using multiple techniques, including diffraction,[29,30] spectroscopy[31–33] and theory.[34,35] Although ion-induced structuring of water molecules within the coordination shell is unambiguous, there have been conflicting interpretations amongst these results as to whether ion-water interactions can extend beyond the first solvation shell. For example, recent dielectric relaxation studies on hydrated phosphates indicate interactions extend into a full second solvation shell.[33] Although previous neutron diffraction studies have revealed extended ion-water interactions,[36] experiments with hydrated phosphate salts show no evidence for ionic influences beyond direct coordination to the ion.[30] The dynamic nature of water molecules makes probing weak ion-induced structural effects beyond a rigid inner shell a challenging endeavor. Measurements of MCAs in aqueous solution contain contributions from several counterions, which complicates the ability to assign interactions between water molecules and a single ion. Furthermore, many condensed phase techniques rapidly lose sensitivity with decreasing concentration such that uncoordinated water molecules are scarce and long-distance orientation effects from a single ion cannot be inferred.

The structure of size-selected $(H_2O)_n$ aqueous clusters in the gas phase can be studied using vibrational spectroscopy in the O–H stretching region. Water molecules at the surface of neutral clusters are free to orient with non-bonded hydrogens facing away from the cluster, which has been observed experimentally by the unique absorption band at ∼3700 cm^{-1}.[37,38] Using IRPD spectroscopy of mass-selected, ion-containing water clusters, orientation effects on water by a single solvated ion free of any counterion contributions can be measured.[21,39,40] The sensitivity of this technique is not limited by the ratio of water molecules to ions. As a result, ion-water interactions can be measured to a hypothetical infinite dilution. IRPD spectra for SO_4^{2-} and $Fe(CN)_6^{3-}$ show that the non-bonded O–H stretch is absent with droplet radii up to ∼0.7 and 0.8 nm, respectively, as a result of long-distance orientation effects by the MCAs.[21,39]

The tetraanion ferrocyanide, $Fe(CN)_6^{4-}$, is stable in aqueous solution, where it is commonly used as a probe for monitoring intracellular redox events in living cells.[41] It is also a precursor to the pigment Prussian blue, $Fe_4[Fe(CN)_6]_3$, which is used as a medical treatment for internal radioactive Cs^+ and Tl^+ poisoning and is being considered for clean-up of chemically-polluted natural waters caused by nuclear contamination.[42–44] Experiments on this ion in water have revealed a distinct inner solvation shell around ferrocyanide, but no information has been reported about how this anion influences the structure of water beyond the first solvation shell.[45–48] The direct measurement of extended ion-water interactions by an individual tetraanionic species is not feasible in the condensed phase due to the low concentrations necessary for hydration shells to exist unperturbed by counterions. However, the stability afforded by aqueous gas phase clusters and the sensitivity of IRPD spectroscopy to the orientation of surface water molecules provide a well-suited method for studying this high charge density tetraanion.

Here, the dissociation pathways and ion-solvent interactions in hydrated clusters of $Fe(CN)_6^{4-}$ are investigated using BIRD, IRPD spectroscopy and molecular modeling. Remarkably, $Fe(CN)_6^{4-}(H_2O)_n$ with $n = 41$ is required for thermodynamic stability, although metastable clusters as small as $n = 37$, which dissociate via electron ejection, are observed. These findings illustrate that stability to electron ejection is achieved only through solvation with a nearly complete second hydration shell and therefore provides a direct observation of long-distance interactions between the ion and solvent. The spectroscopic signatures in the O–H oscillator region show ion-induced patterning of the hydrogen-bonding network can extend beyond a nanometer distance from the ion, corresponding to the fourth solvation shell. From ion-solvent interactions in lower valency anions, a minimum Coulomb potential required for orienting surface water molecules in clusters can be determined. This is the first report of a critical cluster size for a small hydrated tetraanion and is the smallest, highest charge density tetraanion that has been formed in the gas phase.

3.2 Experimental Methods

3.2.1 Mass Spectra

All experimental data were obtained using a home-built 7.0 T Fourier transform ion cyclotron resonance (FT-ICR) mass spectrometer based on an instrument described elsewhere,[49] which has been upgraded to incorporate a 7 T magnet. Hydrated ions are formed by nanoelectrospray ionization (nESI) of 10 mM aqueous solutions of potassium hexacyanoferrate(II) trihydrate (Sigma Aldrich, St. Louis, MO) with purified water from a Milli-Q system (Millipore, Billerica, MA). Solutions are loaded into borosilicate capillaries with tips that have been pulled to an inner diameter of ∼1 µm. A platinum wire in contact with the solution is held at a constant potential of ∼700 V with respect to a heated metal capillary at the entrance of the mass spectrometer. Ions are guided via electrostatic lenses through five stages of differential pumping into the ion cell, which is enclosed by a copper jacket that is temperature-controlled to 133 K by a flow of liquid nitrogen and is thermalized for at least 8 h prior to data acquisition.[50] A pulse of dry nitrogen gas is introduced to bring the pressure of the vacuum chamber containing the ion cell to $\sim 2 \times 10^{-6}$ Torr, which helps to both trap and thermalize the ions. After an ∼8 s pump down period following the pulse gas, the pressure in the chamber decreases to $\sim 2 \times 10^{-9}$ Torr. Precursor ions of interest are subsequently isolated using a notched stored waveform inverse Fourier transform excitation.

3.2.2 Infrared Photodissociation

IRPD spectra between 2800 and 3800 cm^{-1} are measured with infrared photons from a tunable OPO/OPA system (LaserVision, Bellevue, WA) pumped by the 1064 nm fundamental of a Nd:YAG laser (Continuum Surelight I-10, Santa Clara, CA) operating at a 10 Hz repetition rate. Mass-selected precursor ions isolated in the ion cell are irradiated for between ∼0.25 – 1.0 s in order to produce substantial, but not complete, dissociation of the isolated aqueous cluster. A first-order rate constant is obtained from the relative abundances of precursor and product ions after photodissociation. The IRPD rate constants from laser irradiation are corrected for frequency dependent variations in laser power as well as dissociation due to BIRD.[51]

3.2.3 Calculations

Molecular dynamics trajectories were obtained using Desmond 3.1 (Schrödinger, Inc., Portland, OR). The isolated ferrocyanide complex was first optimized using Q-Chem 4.0[52] (Q-Chem, Inc., Pittsburgh, PA) at the B3LYP/LACVP++** level of theory. This optimization uses a confined electronic structure that does not permit electron ejection. Water molecules were added thereafter with the optimized ferrocyanide complex in the center to model $\text{Fe(CN)}_6^{4-}(\text{H}_2\text{O})_{160}$. During the simulation, the Fe–C force constants were increased in order to avoid cyano ligand loss, which does not occur experimentally for nanodrops of this size, but has been observed previously in QM/MM simulations.[48] The ion was not confined to the center of the aqueous cluster during the dynamics trajectories. An initial geometry relaxation was performed followed by equilibration with a 1 ns stochastic dynamics trajectory at 133 K using the OPLS 2005 force field with 1.0 fs time steps. In order to increase the conformational space explored in these trajectories, a series of annealing cycles were used to generate low-energy conformers. The upper temperature was chosen such that evaporation does not occur and water molecules can readily exchange between hydration shells. Each cycle consists of 200 ps at 195 K followed by gradual linear cooling over 300 ps to 135 K. The system is then equilibrated at 135 K for 1 ns followed by an additional 1 ns trajectory, from which five structures are taken in regular intervals. A comparison of the radial distribution functions for individual structures along the simulation shows that the hydrogen-bonding network of $\mathrm{Fe(CN)_6^{4-}(H_2O)_{160}}$ is not static within the final 1 ns of an annealing cycle at 133 K (Figure A.5). This procedure is repeated 20 times in order to generate 100 low-energy structures for $\mathrm{Fe(CN)_6^{4-}(H_2O)_{160}}$. The atomic coordinates from these structures are used to measure radial distribution functions, dipole orientations and estimate the ion-surface distance for $\mathrm{Fe(CN)_6^{4-}(H_2O)_{160}}$. The same procedure for simulated annealing molecular dynamics was also used to generate 100 low-energy structures for $\mathrm{(H_2O)_{165}}$, which are used to measure water molecule dipole orientations in neutral clusters.

3.3 Results and Discussion

3.3.1 Hydrated Ion Formation

Several different hydrated ions are observed in the nESI mass spectra of 10 mM aqueous solutions of $\mathrm{K_4Fe(CN)_6}$ (Figure 3.1), including the tetraanion ferrocyanide, $\mathrm{Fe(CN)_6^{4-}(H_2O)_n}$. The smallest ferrocyanide cluster produced under a range of instrumental conditions is $n = 38$, but clusters with $n > 320$ can be readily formed by reducing voltages to source optics, decreasing the temperature of the entrance capillary, and by optimizing the excitation waveform to enhance detection of larger clusters. Expanded regions of the mass spectra tuned for both small and large cluster sizes show the onset of ferrocyanide clusters at $n = 38$ and the presence of protonated and potassiated adducts (Figure A.6). Three isolated species without hydrate distributions are observed, $\mathrm{Fe(CN)_5^{2-}}$ ($m/z = 92.9$), $\mathrm{Fe(CN)_4^{2-}}$ ($m/z = 79.9$) and $\mathrm{Fe(CN)_3^{-}}$ ($m/z = 133.9$), which are formed via sequential ligand loss from the ferricyanide dianion.[21] A summary of all hydrated species formed by nESI is given in Table 3.1 and the isolated distributions of each hydrated ion are shown in Figure 3.2.

The smallest $\mathrm{Fe(CN)_6^{4-}(H_2O)_n}$ cluster formed by nESI is $n = 38$, whereas the largest $\mathrm{Fe(CN)_6^{3-}(H_2O)_n}$ is $n = 40$. Similarly, the smallest $\mathrm{Fe(CN)_6^{3-}(H_2O)_n}$ cluster is $n = 8$ and the largest $\mathrm{Fe(CN)_6^{2-}(H_2O)_n}$ is $n = 7$. This is consistent with the previous results for $\mathrm{Fe(CN)_6^{3-}(H_2O)_n}$, which show that electron ejection occurs for $n \leq 8$.[21] The absence of dianionic $\mathrm{Fe(CN)_6^{2-}(H_2O)_n}$ clusters with $n > 8$ indicates this species is not present in solution, but is instead formed via gas phase dissociation of $\mathrm{Fe(CN)_6^{3-}(H_2O)_n}$ with $n \geq 8$.

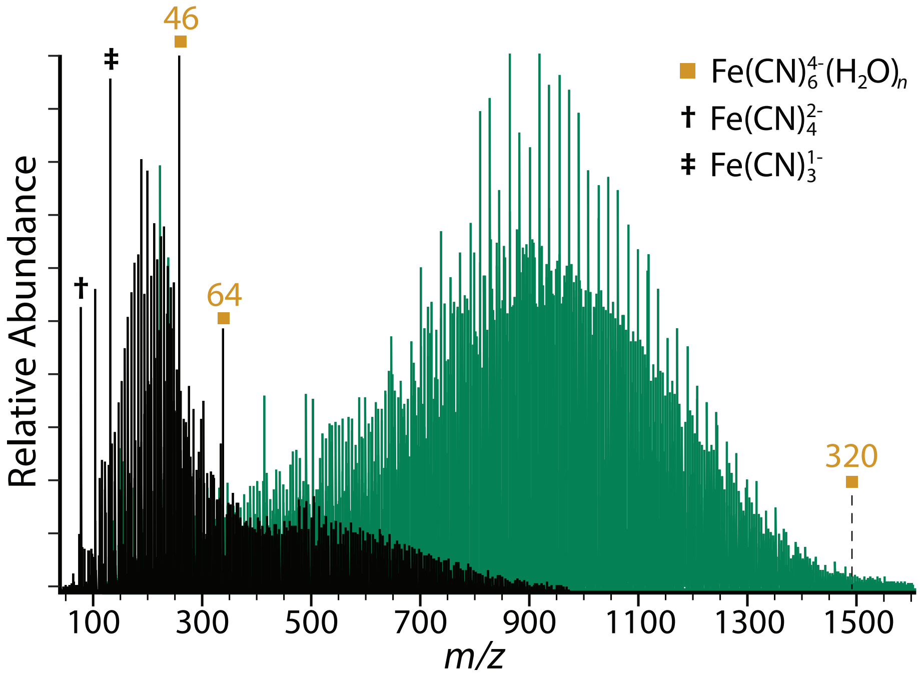

Figure 3.1: Nanoelectrospray ionization mass spectra obtained from 10 mM aqueous solutions of $K_4Fe(CN)_6$ with instrumental conditions tuned for small (black) and large clusters (green). Magic number clusters for $Fe(CN)_6^{4-}(H_2O)_n$ are observed at $n = 46$ and 64. Bare species with no hydrates include $Fe(CN)_4^{2-}$ (†) and $Fe(CN)_3^-$ (‡).

Similarly, the $Fe(CN)_6^{3-}(H_2O)_n$ distribution from $n = 8 - 40$ likely originates via electron ejection from larger unstable tetraanion ferrocyanide clusters. There is a similar correlation between charge states for the adducted species. Based on the distributions, electron ejection likely occurs from $HFe(CN)_6^{3-}(H_2O)_n$ near $n \simeq 17$ and for $KFe(CN)_6^{3-}(H_2O)_n$ with $n \simeq 19$. The cluster size distributions indicate that the lower charge state species are formed in evaporating electrospray droplets through dissociative pathways and are not abundant in aqueous solutions of $K_4Fe(CN)_6$, which primarily contain the ferrocyanide tetraanion and trianionic ion pairs formed by protonation and potassiation of $Fe(CN)_6^{4-}$.

The smallest cluster sizes formed by nESI are smaller for $HFe(CN)_6^{3-}$ ($n = 17$) and $KFe(CN)_6^{3-}$ ($n = 18$) ion-paired species than $Fe(CN)_6^{4-}$. The greater stability associated with proton adduction compared to potassium ion adduction is likely due to more favorable interactions with the higher charge density of H^+ with respect to K^+. These clusters are larger than the smallest clusters of $Fe(CN)_6^{3-}$ ($n = 8$), which indicates that the ferricyanide trianion is intrinsically more stable than the trianions resulting from cation adduction to $Fe(CN)_6^{4-}$. Similarly, we see electron ejection from $HFe(CN)_6^{3-}$ and $KFe(CN)_6^{3-}$ results in dianionic species that are stable as bare ions as a result of the stability gained through ion-pairing. Therefore, the stability gained by cation adduction decreases the onset of dis-

Table 3.1: Hydrated Species Formed by nESI of 10 mM $K_4Fe(CN)_6$

Species Formula	Smallest n	Largest n
$Fe(CN)_6^{4-}(H_2O)_n$	38	>320
$Fe(CN)_6^{3-}(H_2O)_n$	8	40
$Fe(CN)_6^{2-}(H_2O)_n$	0	7
$H_2Fe(CN)_6^{2-}(H_2O)_n$	0	>150
$HFe(CN)_6^{3-}(H_2O)_n$	17	>240
$HFe(CN)_6^{2-}(H_2O)_n$	0	17
$K_2Fe(CN)_6^{2-}(H_2O)_n$	0	>150
$KFe(CN)_6^{3-}(H_2O)_n$	18	>240
$KFe(CN)_6^{2-}(H_2O)_n$	0	19

sociation and the critical cluster size for MCAs.

There are two magic number clusters for ferrocyanide at $n = 46$ and 64. Although peak overlap occurs for $Fe(CN)_6^{4-}$ with $HFe(CN)_6^{3-}$ and $H_2Fe(CN)_6^{2-}$ (Figure A.6), which are isobaric to within 0.01 and 0.03 *m/z* for specific cluster sizes, these magic number clusters are confirmed to originate from the tetraanion based on the isotope spacing. Although the structural origin of the magic number cluster stabilities is unknown, infrared photodissociation studies have suggested that complex clathrate structures may form for clusters of this size, which optimize hydrogen bonding and ultimately lead to enhanced stability.[21,53,54]

3.3.2 Critical Cluster Size and Dissociation Pathways

The smallest $Fe(CN)_6^{4-}(H_2O)_n$ cluster that is formed directly by nESI using a variety of source conditions is $n = 38$. In order to determine the dissociation pathways for this cluster, the isolated precursor $Fe(CN)_6^{4-}(H_2O)_{41}$ (Figure 3.3a) was dissociated using BIRD at 133 K (Figure 3.3b-e). This cluster size was chosen in order to both maximize signal abundance and to avoid signal overlap caused by the clusters containing $HFe(CN)_6^{3-}$ and $H_2Fe(CN)_6^{2-}$ (Figure A.6). Dissociation from $Fe(CN)_6^{4-}(H_2O)_{41}$ occurs exclusively through loss of a single water molecule (reaction 3.1):

$$Fe(CN)_6^{4-}(H_2O)_n \longrightarrow Fe(CN)_6^{4-}(H_2O)_{n-1} + H_2O \qquad \text{(Reaction 3.1)}$$

After 0.5 seconds (Figure 3.3b), a low abundance peak corresponding to $Fe(CN)_6^{3-}(H_2O)_{40}$ is observed. This product cannot come directly from $Fe(CN)_6^{4-}(H_2O)_{41}$ by direct loss of H_2O^- because the electron affinity of a single water molecule is negative. Therefore, this product is formed via electron ejection from $Fe(CN)_6^{4-}(H_2O)_{40}$ (reaction 3.2):

$$Fe(CN)_6^{4-}(H_2O)_n \longrightarrow Fe(CN)_6^{3-}(H_2O)_n + e^- \qquad \text{(Reaction 3.2)}$$

After 1.5 seconds (Figure 3.3c), $Fe(CN)_6^{3-}(H_2O)_{39}$, which can be formed either through loss of a water molecule from $Fe(CN)_6^{3-}(H_2O)_{40}$ or electron ejection from $Fe(CN)_6^{4-}(H_2O)_{39}$,

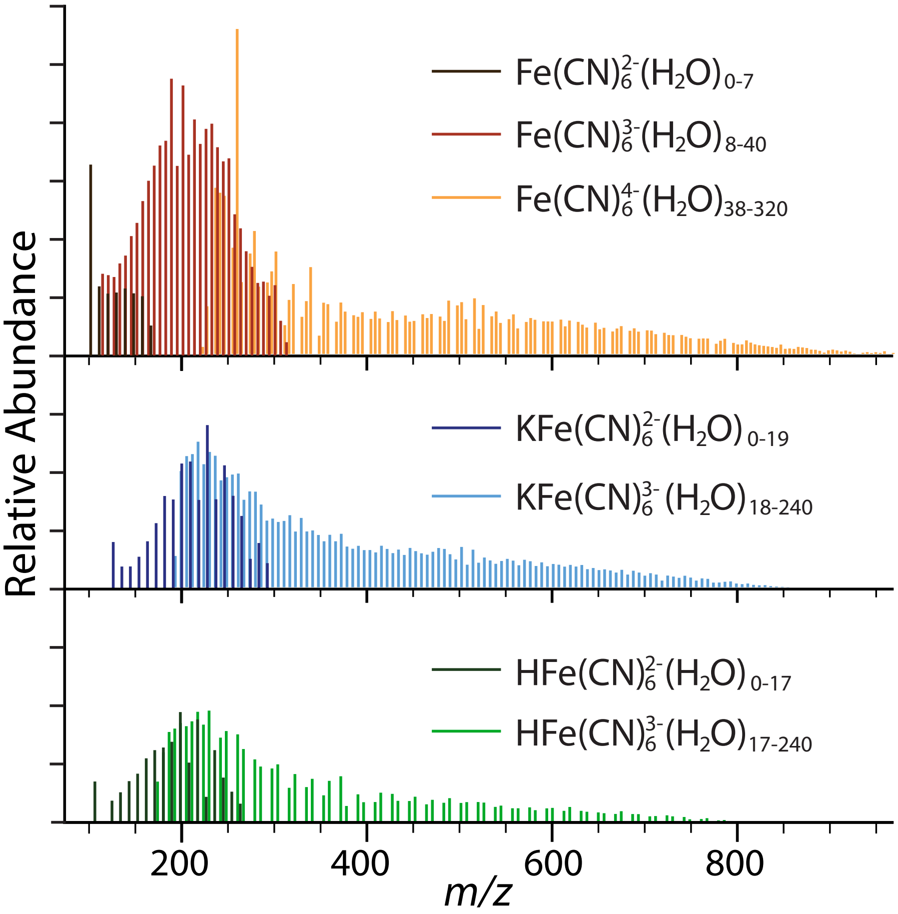

Figure 3.2: Hydrated ion distributions in nanoelectrospray ionization mass spectrum obtained from 10 mM aqueous solution of $K_4Fe(CN)_6$ with instrumental conditions tuned for small clusters. The most abundant ions are obtained from the mass spectral data and are plotted separately. Peaks from overlapping clusters are not included in these isolated spectra and account for gaps in the distributions for $Fe(CN)_6^{4-}$ and $HFe(CN)_6^{3-}$.

starts to appear. $Fe(CN)_6^{4-}(H_2O)_{40}$ also dissociates via water loss to form $Fe(CN)_6^{4-}(H_2O)_{39}$. Thus, $Fe(CN)_6^{4-}(H_2O)_{40}$ dissociates via two pathways – either through loss of a single water molecule (reaction 3.1) or electron ejection (reaction 3.2).

The abundance of $Fe(CN)_6^{3-}(H_2O)_{40}$ is less than that of $Fe(CN)_6^{3-}(H_2O)_{39}$ after 2.0 s (Figure 3.3d). This inversion occurs as a result of only a single precursor dissociating to the former whereas the latter is produced by two dissociative pathways. $Fe(CN)_6^{3-}(H_2O)_{38}$ begins to appear at 2.0 s and it can also be formed by two precursors. The smallest tetraanion observed from BIRD, $Fe(CN)_6^{4-}(H_2O)_{38}$, appears after 7.5 s (Figure 3.3e) and it exclusively dissociates via electron ejection. Therefore, the trianion clusters $Fe(CN)_6^{3-}(H_2O)_n$ with $n \leq 37$ are only formed by sequential water loss from the electron ejection products under low

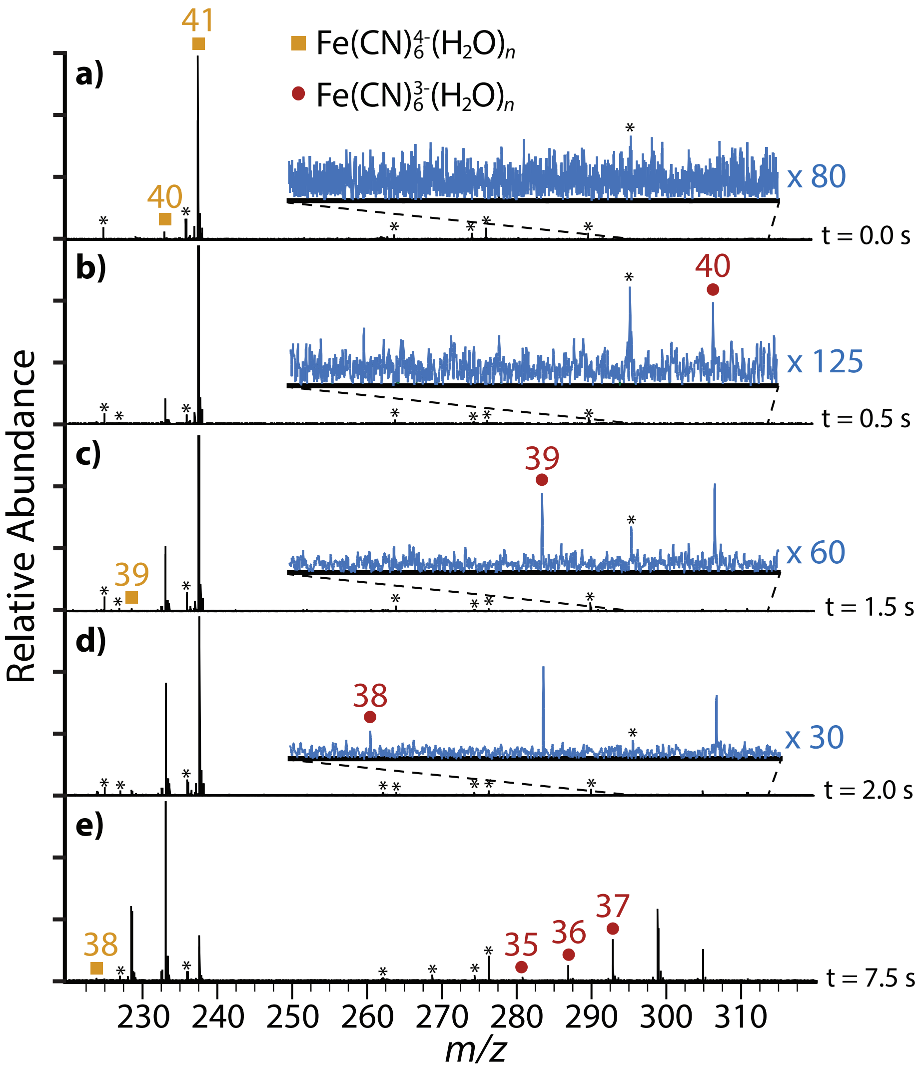

Figure 3.3: BIRD spectra of (a) $Fe(CN)_6^{4-}(H_2O)_{41}$ showing product ions after (b) 0.5 s, (c) 1.5 s, (d) 2.0 s, (e) 7.5 s. Frequency noise is labeled with an asterisk ($*$).

energy ambient blackbody radiation conditions.

The droplet radius for $Fe(CN)_6^{4-}(H_2O)_{41}$ is ∼0.67 nm, which suggests that valence electrons must delocalize beyond the inner solvation shell for thermodynamic stability. Added stability from a subsequent shell can be due to either the added dielectric shielding by the solvent or an extended delocalization of the electron density into the second solvation shell. Evidence for the latter has been reported for the microsolvated fluoride anion, $F^-(H_2O)_6$.[55] Calculations by Canuto et al. indicate that the six valence electrons of fluoride are distributed over the entire cluster. Dyson orbitals corresponding to $F^-(H_2O)_6$ vertical electron detachment energies (VEDE) suggest that the majority of the valence orbital density is delocalized over the water molecules with a maximum of 45% localized on fluorine, which occurs only for a high-energy VEDE.[55] Therefore, it is possible that delocalization of the orbital density for valence electrons in $\mathrm{Fe(CN)_6^{4-}(H_2O)}_n$ is required to extend beyond the coordinating hydration shell before the system is stable to electron ejection, which can explain the necessity of $n \geq 41$ water molecules required in order to fully stabilize $\mathrm{Fe(CN)_6^{4-}}$.

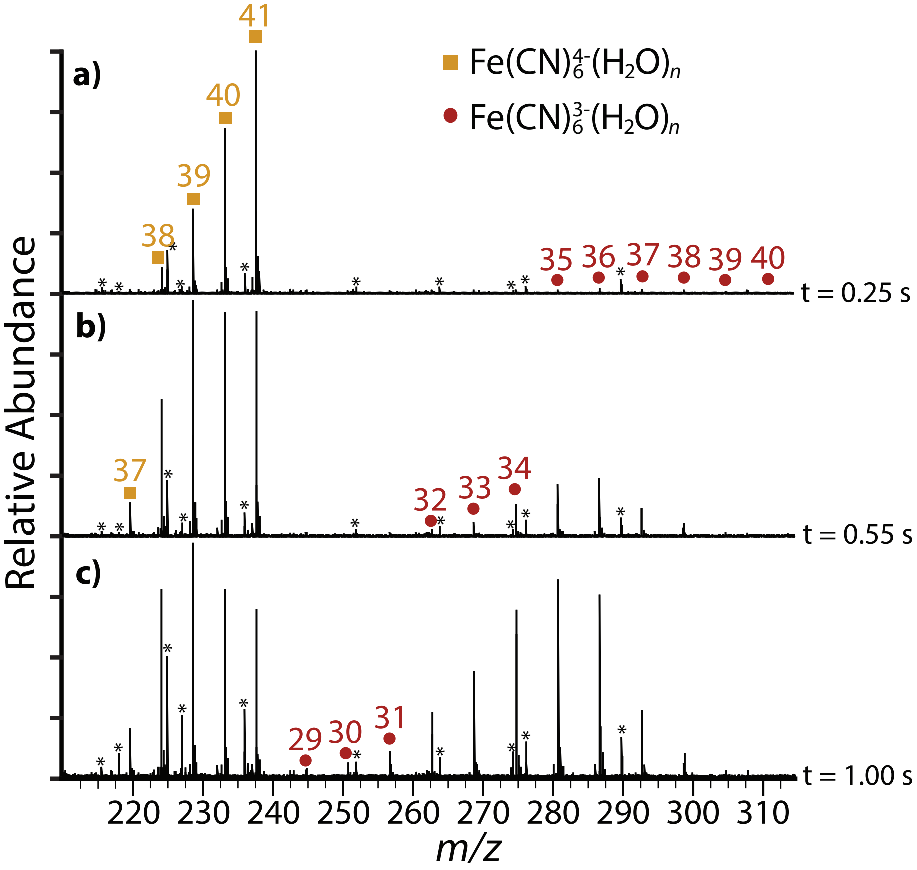

Figure 3.4: IRPD spectra of $\mathrm{Fe(CN)_6^{4-}(H_2O)_{41}}$ at 3521 $\mathrm{cm^{-1}}$ showing product ions after (a) 0.25 s, (b) 0.55 s, (c) 1.00 s. Frequency noise is labeled with an asterisk ($*$).

Although $\mathrm{Fe(CN)_6^{3-}(H_2O)_8}$ exclusively dissociates via electron ejection under low energy BIRD conditions, water loss to form the $n = 7$ cluster is entropically favored and becomes the major product under higher energy excitation conditions.[21] To investigate whether the same is true for $\mathrm{Fe(CN)_6^{4-}(H_2O)}_n$, infrared photons from a tunable laser at 3521 $\mathrm{cm^{-1}}$, corresponding to the hydrogen-bonded region, were used to dissociate $\mathrm{Fe(CN)_6^{4-}(H_2O)_{41}}$ for various times (Figure 3.4). Sequential water loss to form $\mathrm{Fe(CN)_6^{4-}(H_2O)_{38}}$, the smallest tetraanion observed using BIRD, is visible after only 0.25 s (Figure 3.4a). Electron ejection products, $\mathrm{Fe(CN)_6^{3-}(H_2O)}_n$, are also observed for $n = 35 - 40$. There is no evidence for electron ejection from $\mathrm{Fe(CN)_6^{4-}(H_2O)_{41}}$, which continues to dissociate exclusively through water loss with higher energy dissociation. After 0.55 s (Figure 3.4b) water loss from $Fe(CN)_6^{4-}(H_2O)_{38}$ occurs to form $Fe(CN)_6^{4-}(H_2O)_{37}$, which is the smallest tetraanion observed in these experiments. Longer dissociation times up to 1.00 s (Figure 3.4c) result only in further sequential water loss from $Fe(CN)_6^{3-}(H_2O)_n$. Therefore, water loss is entropically-favored for $Fe(CN)_6^{4-}(H_2O)_{38}$ and it occurs only under higher energy excitation conditions.

3.3.3 Patterning of Water at Long Distances by $Fe(CN)_6^{4-}$

To investigate the effect $Fe(CN)_6^{4-}$ has on the structure of the hydrogen-bonding network of water molecules located remotely from the ion, IRPD spectra of $Fe(CN)_6^{4-}(H_2O)_n$ at select sizes between $n = 102 - 218$ were measured (Figure 3.5). There is a broad feature in the spectral region between ~2800 – 3600 cm^{-1} that is observed for all cluster sizes. Intensity within this frequency range corresponds to water molecules that donate two hydrogen bonds either to the solvated ion or to adjacent water molecules. These oscillators include three- or four-coordinate water molecules in the bulk of the cluster that accept one (**ADD**, or acceptor-donor-donor) or two (**AADD**, or acceptor-acceptor-donor-donor) hydrogen bonds, or two-coordinate water molecules at the surface of the cluster that do not accept any hydrogen bonds (**DD**, or donor-donor). The maximum of this feature in the bonded O–H region for $Fe(CN)_6^{4-}(H_2O)_n$ red shifts from 3438 cm^{-1} ($n = 102$) to 3389 cm^{-1} ($n = 218$), which is indicative of more optimal, stronger hydrogen bonding between water molecules in the larger clusters.

For hydrated clusters with $n = 102$ and 142, intensity in the region between 3600 – 3800 cm^{-1} is fully attributable to the tail of the fully hydrogen-bonded feature. A band near ~3700 cm^{-1} is due to water molecules that donate only one hydrogen bond, leaving the second O–H oscillator, commonly referred to as a "free O–H", at the surface facing outward and away from the cluster. Absence of unique spectral features near ~3700 cm^{-1} indicates that all water molecules on the surface of the cluster are donating two hydrogen bonds. The spectra for clusters with $n \geq 162$ have a feature centered at ~3704 cm^{-1} characteristic of three-coordinate **AAD** (acceptor-acceptor-donor) water molecules.[53,54,56–60] The frequency of these oscillators depends on the charge state of the hydrated ion, the extent of hydration and to a lesser extent, the size of the ion.[61,62] The intensity of this band increases for $n =$ 182 and 218, indicating that the surface of these clusters is populated with an increasing number of **AAD** water molecules.

For cations, the **AAD** oscillators are observable at the onset of hydration and increase in intensity for larger clusters, whereas for higher valency anions, this stretch is absent until there are a sufficient number of water molecules to effectively shield the ionic potential from water molecules at the cluster surface. The effect of the ion on the hydrogen-bonding network of water molecules in these clusters depends both on the orientation of water molecules directly coordinated to the ion and the electrostatic interaction of the solvated ion with the water dipole, which orients inwards toward the ion for anionic hydrated clusters. As a result, the initial presence of this free O–H stretch for an anionic cluster size indicates the

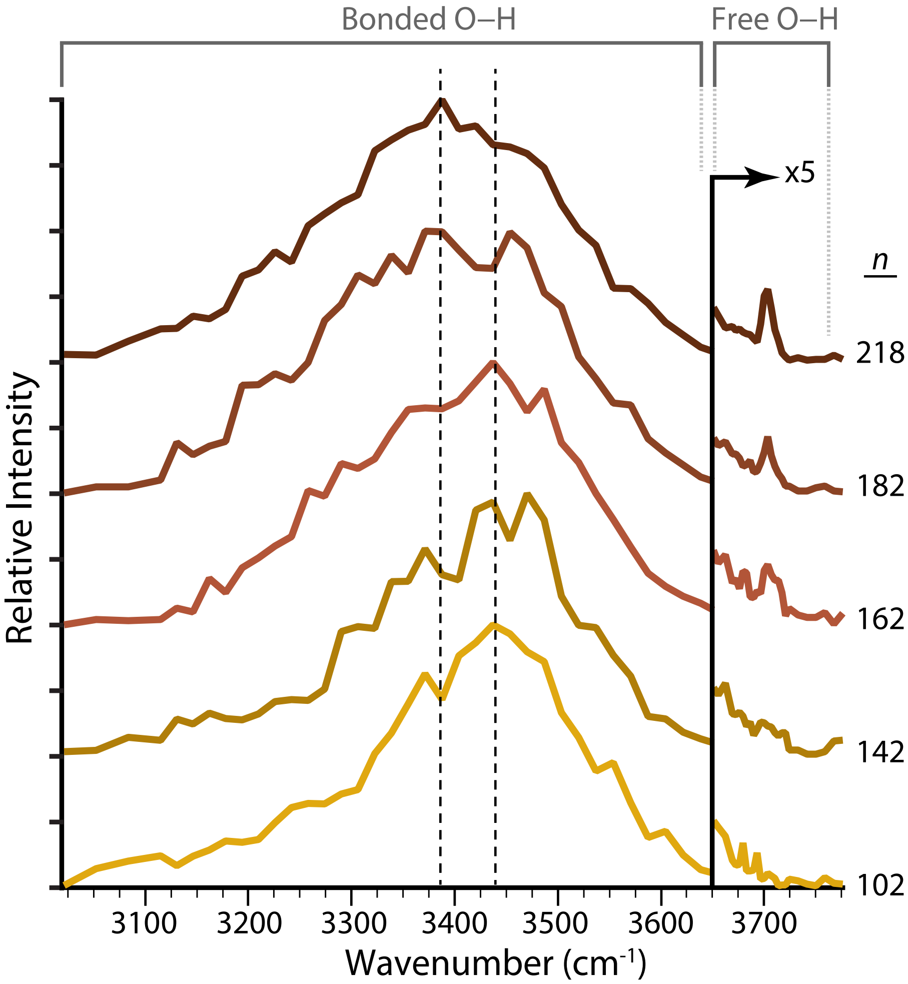

Figure 3.5: Infrared photodissociation spectra of $\mathrm{Fe(CN)_6^{4-}(H_2O)}_n$ with n between 102 and 218. The spectra have been expanded by 5× above 3650 $\mathrm{cm^{-1}}$ in order to more clearly show the free O–H region, where acceptor-acceptor-donor (**ADD**) water molecules begin to appear for $n = 162$ at 3704 $\mathrm{cm^{-1}}$.

extent of water patterning by the solvated ion. Although a free O–H stretch may appear for select microsolvated cluster sizes as a consequence of the available bonding motifs, i.e., water molecules in a small cluster with no hydrogen-bonding partner accessible, there are no consistent free O–H stretches in the IRPD spectra of $\mathrm{(H_2O)}_n^-$ until $n \geq 15$,[63] for $\mathrm{SO_4^{2-}(H_2O)}_n$ until $n > 43$,[39] and for $\mathrm{Fe(CN)_6^{3-}(H_2O)}_n$ until $n \geq 70$.[21] While the exact location of the electron in $\mathrm{(H_2O)}_n$ has not yet been resolved, it is evident that all water molecule hydrogen atoms interact with the diffuse electron cloud until $n \geq 15$.[63] In contrast, the higher charge state anions are expected to be located closer to the center of the cluster to maximize the stabilizing effects of solvation.

In order to ascertain the relationship between ionic charge state and patterning distance, the radii of clusters for which **AAD** water molecules begin to appear as a function of the anionic charge state is shown in Figure 3.6. The four anionic charge states follow a linear trend with distance. This is the behavior expected from a Coulombic potential, $V_{Coulomb}$, produced by a point charge, Q (equation 3.1):

$$r = \frac{Q}{4\pi\varepsilon V_{Coulomb}} \qquad \text{(Equation 3.1)}$$

where r is the radius of the hydrated cluster and ε is the permittivity of water. Because r is proportional to Q, the potential, $V_{Coulomb}$, is expected to be roughly constant across the four anionic charge states for the cluster size where **AAD** water molecules appear. Using the permittivity of ice extrapolated to 133 K, this potential is calculated to be $(2.4 \pm 0.6) \times 10^{-13}$ J/C. This is the minimum potential required in order to orient the water molecules inward and prevent the emergence of free O–H oscillators at the cluster surface.

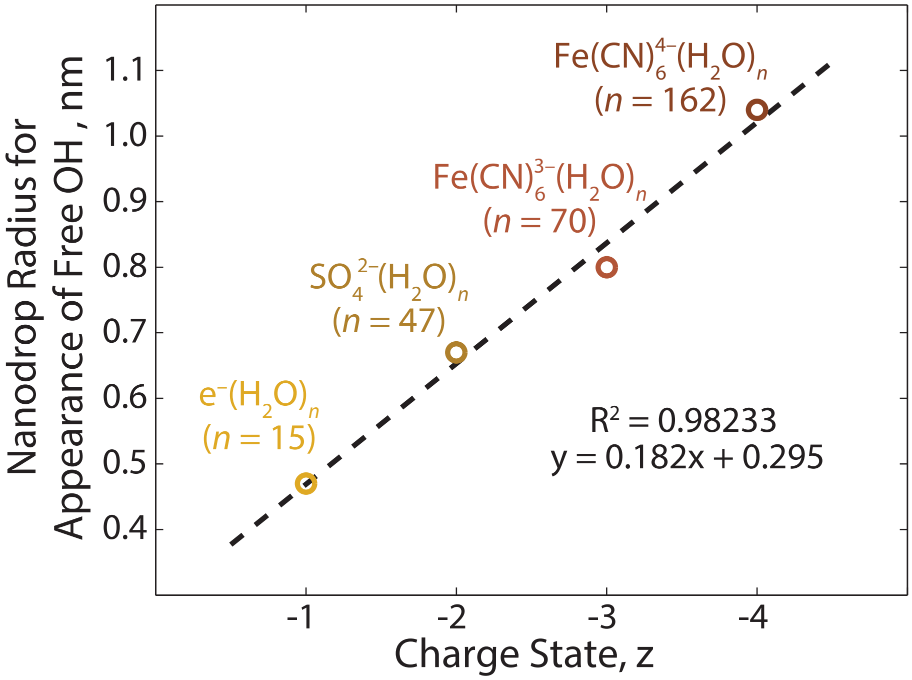

Figure 3.6: Linear relationship between the nanodrop radius for the onset of acceptor-acceptor-donor (**AAD**) water molecules at the cluster surface and corresponding anionic charge state.[21,39,63] The cluster radius is obtained from the water density assuming the nanodrops are spherical. Void space due to the ion is neglected.

In order to obtain an estimate for the radius of these clusters and the number of hydration shells, a molecular dynamics trajectory was performed for $Fe(CN)_6^{4-}(H_2O)_{160}$. A radial distribution function (Figure 3.7a) shows three full solvation shells with the onset of a fourth shell. The first shell, centered ~0.38 nm away from the ion, is the narrowest in width as a result of the strong interaction between water molecules and $Fe(CN)_6^{4-}$. The width of subsequent shells expands as the water molecules interact less strongly with the central ion and have more rotational and translational freedom in comparison to the rotationally constricted inner water molecules. Each of the shells are ∼0.25 nm away from one another, with the third shell at ∼0.87 nm the widest. The fourth shell is centered at ∼1.1 nm, where the first water molecules with the characteristic **AAD** orientation reside.

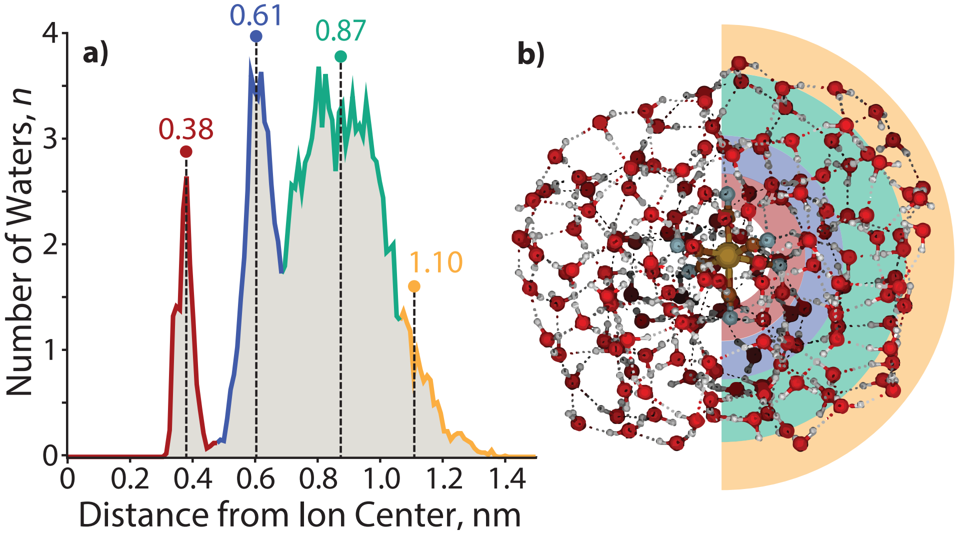

Figure 3.7: (a) Radial distribution plot illustrating the structure for solvation shells around $Fe(CN)_6^{4-}(H_2O)_{160}$. Water molecules are counted within a bin width for a radial thickness of 0.01 nm. (b) Structure of $Fe(CN)_6^{4-}(H_2O)_{160}$ taken at the end of a simulated annealing molecular dynamics trajectory. Colors are overlaid according to the edges of the corresponding solvent shell divisions provided in *a*.

A model of $Fe(CN)_6^{4-}(H_2O)_{160}$ at the end of the trajectory (Figure 3.7b) provides a cross sectional view of the hydration shells with overlaid colors based on the radial distribution function. The distance from the center of the ion to the surface of the cluster for several structures along the trajectory results in a radius of 0.96 ± 0.05 nm, which is close to the distance obtained using the density of bulk water (1.05 nm). The orientation of water molecules with respect to the solvated ion is shown in Figure 3.8a. Water molecules within the first hydration shell interact strongly with the ion and have $<\theta> \simeq 20°$. An increase in $<\theta>$ occurs until approximately 0.7 nm, which corresponds to the beginning of the third solvation shell. Although the average angle still faces inward toward the ion, water molecules in the second and third shells can hydrogen bond with a four-coordinate **AADD** motif, which enthalpically stabilizes a wider range of orientations than are possible within the first hydration shell. A value of $<\theta> \simeq 65°$ persists into the third shell until water molecules are 1.0 – 1.4 nm away from the ion. These are the outer shell surface water molecules, which are restricted in orientation due to diminished hydrogen-bonding partners. Although this is the distance where free OH water molecules begin to emerge, the average water molecule is clearly orienting inward as far as 1.4 nm from the ion with a value of $<\theta> \simeq 55°$, which is more acute with respect to the third shell as a result of surface constraints.

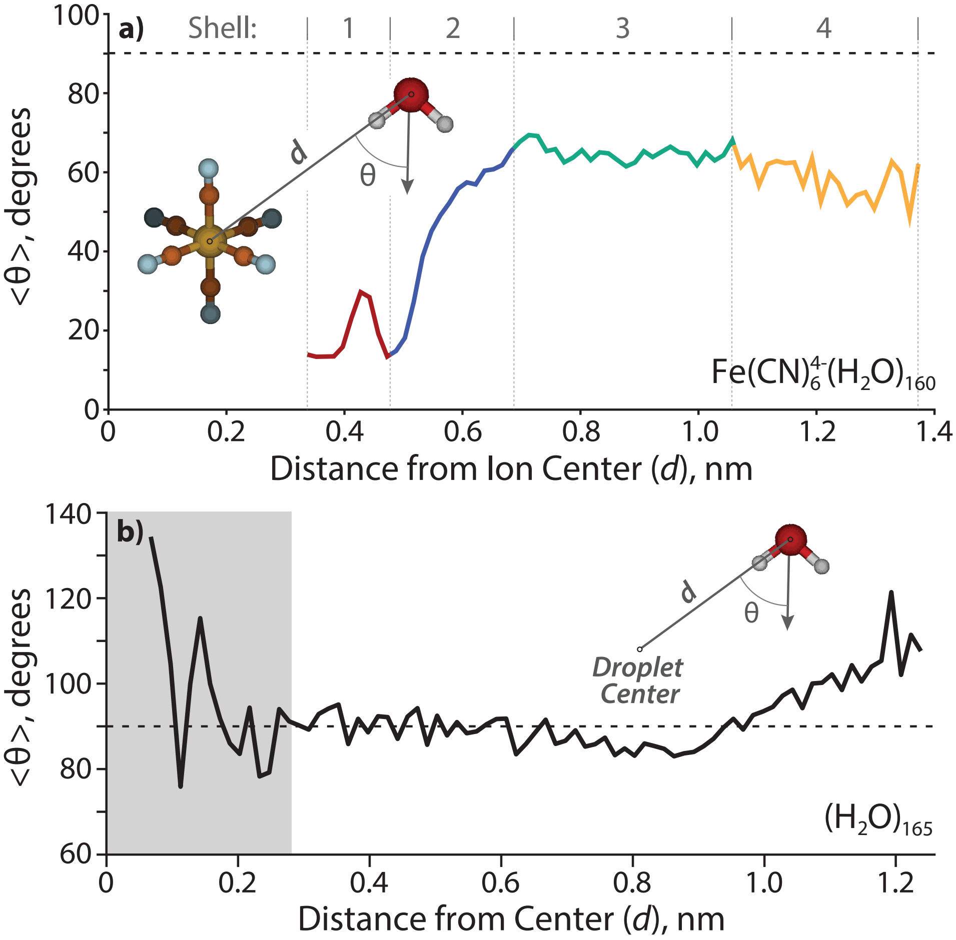

Figure 3.8: Average angle θ (depicted in insets) for water molecule orientation as a function of distance relative to (a) the solvated ion center in $\mathrm{Fe(CN)_6^{4-}(H_2O)_{160}}$ and (b) the geometric center of $\mathrm{(H_2O)_{165}}$. The horizontal dotted line corresponds to a water molecule orientation with the dipole perpendicular to the ion, $<\theta> = 90°$. Water molecules are counted within a bin width for a radial thickness of 0.015 nm. The gray box in *b* extends to 0.28 nm, which represents the average O–O distance between water molecules and therefore is not indicative of any propagating trends.

For comparison, data was also obtained for $<\theta>$ with respect to the center of a neutral nanodrop. The void space of $\mathrm{Fe(CN)_6^{4-}}$ in $\mathrm{Fe(CN)_6^{4-}(H_2O)_{160}}$ is $\simeq 5$ water molecules. Therefore, $n = 165$ was chosen in order to model a neutral nanodrop of comparable size (Figure 3.8b). Water molecules are randomly oriented ($<\theta> \simeq 90°$) up to ∼0.9 nm, where $<\theta>$ reaches a minimum of ∼85°. The water molecules between ∼1.0 – 1.24 nm are biased to face outward with respect to the center of the droplet, which is indicative of **AAD** water molecules that have a free O–H at the surface. The slight inward-facing bias between ∼0.7 – 0.95 nm is likely due to a restriction in orientation for water molecules in this shell in order to support the outward-facing motif of the surface water molecules. The furthest ion-oxygen distance reported for $Fe(CN)_6^{4-}(H_2O)_{160}$ ($d = 1.37$ nm) is slightly larger than that measured for $(H_2O)_{165}$ ($d = 1.24$ nm) as a result of $Fe(CN)_6^{4-}$ not being confined to the nanodroplet center.

3.4 Conclusion

Aqueous clusters of $Fe(CN)_6^{4-}(H_2O)_n$ with $n \geq 38$ can be formed using nESI. Ferrocyanide is the highest charge density tetraanion that has been observed in the gas phase and measurements of aqueous nanodrops containing this anion provide a direct means for investigating how water stabilizes highly charged anions. $Fe(CN)_6^{4-}(H_2O)_{38}$ is the smallest cluster size observed directly by nESI and it dissociates exclusively by electron ejection under low-energy BIRD conditions. In addition to electron ejection, clusters of size $n \geq 39$ can also dissociate by sequential loss of water molecules, which is the only dissociative pathway for clusters with $n \geq 41$. Higher-energy dissociation conditions obtained through IRPD result in the entropically-favored loss of a water molecule to form $Fe(CN)_6^{4-}(H_2O)_{37}$, which is the smallest ferrocyanide cluster observed in these experiments.

The droplet radius for $Fe(CN)_6^{4-}(H_2O)_{40}$, the largest cluster unstable to electron ejection, is ∼0.66 nm. This corresponds to a nearly complete second hydration shell and is almost twice the radius observed for the trianion ferricyanide, which undergoes electron ejection with $n \leq 8$ ($r \simeq 0.38$ nm).[21] This is a clear illustration of ion-water interactions that extend beyond the inner coordination sphere. The necessity of solvation with $n \geq 41$ is likely due to delocalization of the orbital density for valence electrons in $Fe(CN)_6^{4-}(H_2O)_n$, which must extend into a nearly complete second solvation shell. Stability obtained through ion-ion interactions results in a high propensity for ferrocyanide to form ion pairs with H^+ and K^+, which decrease the minimum solvation required for stability to electron ejection.

A free OH band in the IRPD spectrum of $Fe(CN)_6^{4-}(H_2O)_n$ appears between $n = 142$ and 162, indicating the ion-water interactions extend well beyond the second solvation shell. Remarkably, orientation of surface water molecules by the ion persists until $n \geq 162$, which is significantly larger than that observed for the ferricyanide trianion ($n \geq 70$). Based on structures from molecular modeling, clusters of size $n = 160$ have an average radius of ∼0.96 ± 0.05 nm, which extends into a fourth solvation shell. There is a linear trend between anionic charge state and cluster radii for the onset of **AAD** water molecules. Based on the single value for the Coulombic potential at the cluster surface obtained from these results, a small pentanionic species is predicted to orient water molecules up to clusters of size $n \simeq 310$, which have a radius of 1.3 nm.

The clusters in these experiments are equilibrated to cold temperatures (133 K) and the thermal motion of water molecules increases with temperature. At elevated temperatures, the entropic drive for surface water molecules to orient with free hydrogens will eventually predominate enthalpically favored hydrogen-bonding interactions. However, the perturbed water orientation observed up to nanometer length in these clusters is representative of interactions that, although diminished, will persist at warmer temperatures. These interactions are especially important in environments where water is scarce, such as in living cells and reverse micelles, and will manifest as changes to the dynamics of surrounding water molecules as well as freezing point depression.[40] Long-distance forces originating from ions may also partially account for Hofmeister and other ion-related phenomena.

3.5 References

[1] Simons, J. *J. Phys. Chem. A* **2008**, *112*, 6401–6511.

[2] Boldyrev, A. I.; Gutowski, M.; Simons, J. *Acc. Chem. Res.* **1996**, *29*, 497–502.

[3] Sverdrup, H. U.; Johnson, M. W.; Fleming, R. H. *The Oceans: Their Physics, Chemistry, and General Biology*; Prentice-Hall, Inc: New York, 1942.

[4] Hawthorne, F. C.; Krivovichev, S. V.; Burns, P. C. *Rev. Mineral. Geochem.* **2000**, *40*, 1–112.

[5] Muyzer, G.; Stams, A. J. M. *Nat. Rev. Microbiol.* **2008**, *6*, 441–454.

[6] Harris et. al., E. *Science* **2013**, *340*, 727 – 730.

[7] Chauhan, B. S. *Principles of Biochemistry and Biophysics*, 1st ed.; University Science Press: Boston, 2008.

[8] Whitehead, A.; Barrios, R.; Simons, J. *J. Chem. Phys.* **2002**, *116*, 2848–2851.

[9] Boldyrev, A. I.; Simons, J. *J. Phys. Chem.* **1994**, *98*, 2298–2300.

[10] Wang, X. B.; Wang, L. S. *Nature* **1999**, *400*, 245–248.

[11] Boxford, W. E.; Dessent, C. E. H. *Phys. Chem. Chem. Phys.* **2006**, *8*, 5151–5165.

[12] Dreuw, A.; Cederbaum, L. S. *Phys. Rev. A* **2000**, *63*, 012501.

[13] Wang, L. S.; Ding, C. F.; Wang, X. B.; Nicholas, J. B. *Phys. Rev. Lett.* **1998**, *81*, 2667–2670.

[14] Blagojevic, V.; Petrie, S.; Böhme, D. K. *Int. J. Mass. Spectrom.* **2004**, *233*, 33–37.

[15] Hartig, J.; Blom, M. M.; Hampe, O.; Kappes, M. M. *Int. J. Mass. Spectrom.* **2003**, *229*, 93–98.

[16] Yoo, H. J.; Wang, N.; Zhuang, S.; Song, H.; Håkansson, K. *J. Am. Chem. Soc.* **2011**, *133*, 16790–16793.

[17] Konermann, L.; Douglas, D. J. *J. Am. Soc. Mass Spectrom.* **1998**, *9*, 1248–1254.

[18] McLuckey, S. A.; Habibi-Goudarzi, S. *J. Am. Chem. Soc.* **1993**, *115*, 12085–12095.

[19] Schultz, J. C.; Hack, C. A.; Benner, W. H. *J. Am. Soc. Mass Spectrom.* **1998**, *9*, 305–313.

[20] Xin, Y.; Wang, X. B.; Wang, L. S. *J. Phys. Chem. A* **2002**, *106*, 7607–7616.

[21] DiTucci, M. J.; Heiles, S.; Williams, E. R. *J. Am. Chem. Soc.* **2015**, *137*, 1650 – 1657.

[22] Asmis, K. R.; Neumark, D. M. *Acc. Chem. Res.* **2012**, *45*, 43–52.

[23] Wang, X. B.; Yang, X.; Nicholas, J. B.; Wang, L. S. *Science* **2001**, *294*, 1322–1325.

[24] Wang, X. B.; Yang, X.; Nicholas, J. B.; Wang, L. S. *J. Chem. Phys.* **2003**, *119*, 3631–3640.

[25] Blades, A. T.; Kebarle, P. *J. Am. Chem. Soc.* **1994**, *116*, 10761–10766.

[26] Wong, R. L.; Williams, E. R. *J. Phys. Chem. A* **2003**, *107*, 10976–10983.

[27] Cooper, T. E.; Armentrout, P. B. *J. Phys. Chem. A* **2009**, *113*, 13742–13751.

[28] Zhang, X.; Wanigasekara, E.; Breitbach, Z. S.; Dodbiba, E.; Armstrong, D. W. *Rapid Commun. Mass Spectrom.* **2010**, *24*, 1113–1123.

[29] Bouazizi, S.; Nasr, S.; Jaîdane, N.; Bellissent-Funel, M. C. *J. Phys. Chem. B* **2006**, *110*, 23515–23523.

[30] Mason, P. E.; Cruickshank, J. M.; Neilson, G. W.; Buchanan, P. *Phys. Chem. Chem. Phys.* **2003**, *5*, 4686–4690.

[31] Böhm, F.; Sharma, V.; Schwaab, G.; Havenith, M. *Phys. Chem. Chem. Phys.* **2015**, *17*, 19582–19591.

[32] Chizhik, V. I.; Egorov, A. V.; Komolkin, A. V.; Vorontsova, A. A. *J. Mol. Liq.* **2002**, *98*, 173–182.

[33] Eiberweiser, A.; Nazet, A.; Hefter, G.; Buchner, R. *J. Phys. Chem. B* **2015**, *119*, 5270 – 5281.

[34] Du, H.; Rasaiah, J. C.; Miller, J. D. *J. Phys. Chem. B* **2007**, *111*, 209–217.

[35] Marcus, Y. *Chem. Rev.* **2009**, *109*, 1346–1370.

[36] Mancinelli, R.; Botti, A.; Bruni, F.; Ricci, M. A.; Soper, A. K. *Phys. Chem. Chem. Phys.* **2007**, *9*, 2959–2967.

[37] Pradzynski, C. C.; Dierking, C. W.; Zurheide, F.; Forck, R. M.; Buck, U.; Zeuch, T.; Xantheas, S. S. *Phys. Chem. Chem. Phys.* **2014**, *16*, 26691 – 26696.

[38] Pradzynski, C. C.; Forck, R. M.; Zeuch, T.; Slaviček, P.; Buck, U. *Science* **2012**, *337*, 1529 – 1532.

[39] O'Brien, J. T.; Prell, J. S.; Bush, M. F.; Williams, E. R. *J. Am. Chem. Soc.* **2010**, *132*, 8248–8249.

[40] Cooper, R. J.; DiTucci, M. J.; Chang, T. M.; Williams, E. R. *J. Am. Chem. Soc.* **2016**, *138*, 96–99.

[41] Rabinowitz, J. D.; Vacchino, J. F.; Beeson, C.; McConnell, H. M. *J. Am. Chem. Soc.* **1998**, *120*, 2464–2473.

[42] Davidson, D.; Welo, L. A. *J. Phys. Chem.* **1928**, *32*, 1191–1196.

[43] Faustino et al., P. J. *J. Pharm. Biomed. Anal.* **2008**, *47*, 114–125.

[44] Jang, S. C.; Hong, S. B.; Yang, H. M.; Lee, K. W.; Moon, J. K.; Seo, B. K.; Huh, Y. S.; Roh, C. *Nanomaterials* **2014**, *4*, 894 – 901.

[45] Marcus, Y. *J. Solution Chem.* **1994**, *23*, 831–848.

[46] Sando, G. M.; Zhong, Q.; Owrutsky, J. C. *J. Chem. Phys.* **2004**, *121*, 2158–2168.

[47] Yu, P.; Yang, F.; Zhao, J.; Wang, J. *J. Phys. Chem. B* **2014**, *118*, 3104–3114.

[48] Tirler, A. O.; Persson, I.; Hofer, T. S.; Rode, B. M. *Inorg. Chem.* **2015**, *54*, 10355–10341.

[49] Bush, M. F.; O'Brien, J. T.; Prell, J. S.; Saykally, R. J.; Williams, E. R. *J. Am. Chem. Soc.* **2007**, *129*, 1612–1622.

[50] Wong, R. L.; Paech, K.; Williams, E. R. *Int. J. Mass. Spectrom.* **2004**, *232*, 59–66.

[51] Prell, J. S.; O'Brien, J. T.; Williams, E. R. *J. Am. Soc. Mass Spectrom.* **2010**, *21*, 800–809.

[52] Shao et al., Y. *Phys. Chem. Chem. Phys.* **2006**, *8*, 3172–3191.

[53] Fournier et al., J. A. *Proc. Natl. Acad. Sci. USA* **2014**, *111*, 18132–18137.

[54] Cooper, R. J.; Chang, T. M.; Williams, E. R. *J. Phys. Chem. A* **2013**, *117*, 6571–6579.

[55] Canuto, S.; Coutinho, K.; Cabral, B. J. C.; Zakrzewski, V. G.; Ortiz, J. V. *J. Chem. Phys.* **2010**, *132*, 214507.

[56] Shin, J. W.; Hammer, N. I.; Diken, E. G.; Johnson, M. A.; Walters, R. S.; Jaeger, T. D.; Duncan, M. A.; Christie, R. A.; Jordan, K. D. *Science* **2004**, *304*, 1137–1140.

[57] Headrick, J. M.; Diken, E. G.; Walters, R. S.; Hammer, N. I.; Christie, R. A.; Cui, J.; Myshakin, E. M.; Duncan, M. A.; Johnson, M. A.; Jordan, K. D. *Science* **2005**, *308*, 1765–1769.

[58] Diken, E. G.; Hammer, N. I.; Johnson, M. A.; Christie, R. A.; Jordan, K. D. *J. Chem. Phys.* **2005**, *123*, 164309.

[59] Walters, R. S.; Pillai, E. D.; Duncan, M. A. *J. Am. Chem. Soc.* **2005**, *127*, 16599–16610.

[60] Fournier, J. A.; Johnson, C. J.; Wolke, C. T.; Weddle, G. H.; Wolk, A. B.; Johnson, M. A. *Science* **2014**, *344*, 1009–1012.

[61] Prell, J. S.; O'Brien, J. T.; Williams, E. R. *J. Am. Chem. Soc.* **2011**, *133*, 4810–4818.

[62] O'Brien, J. T.; Williams, E. R. *J. Am. Chem. Soc.* **2012**, *134*, 10228–10236.

[63] Hammer, N. I.; Roscioli, J. R.; Bopp, J. C.; Headrick, J. M.; Johnson, M. A. *J. Chem. Phys.* **2005**, *123*, 244311.

Chapter 4

Long Distance Ion-Water Interactions in Aqueous Sulfate Nanodrops Persist to Ambient Temperatures in the Upper Atmosphere

This chapter is reproduced with permission from:
Matthew J. DiTucci, Christiane N. Stachl, and Evan R. Williams
"Long Distance Ion-Water Interactions in Aqueous Sulfate Nanodrops
Persist to Ambient Temperatures in the Upper Atmosphere",
Manuscript in Preparation for Submission, **2017**.

4.1 Introduction

The chemistry and physics of ion-containing aqueous droplets are vital to understanding the behavior of atmospheric aerosols.[1,2] Aerosols impact global radiative forcing,[3,4] act as cloud condensation nuclei to limit the rate of droplet coalescence and suppress rainfall,[5,6] and, in high concentrations, can lead to haze pollution, which negatively impacts human health and agricultural sustainability.[7,8] Sources of atmospheric aerosols are both natural and anthropogenic, ranging from oceanic waves and wind erosion to the use of coal and other fossil fuels.[9] Stratospheric aerosol modification strategies are being considered to mitigate the increase in global temperatures *via* seeding ice clouds to increase the reflection of solar radiation and furthermore diminishing the presence of homogeneously formed cirrus clouds, which contribute negatively to climate warming.[10,11] Aerosol formation in the lower stratosphere can occur through ion-induced nucleation, in which embryonic nanometer-sized clusters act to expedite the rate of aerosol growth.[12,13] An appreciation of the fundamental interactions originating from ions in small aqueous droplets is therefore essential for accurately modeling and investigating the chemistry of atmospheric aerosols.

A property of fundamental interest concerning ion-water interactions is the length to which a water molecule can "see" an ion, *i.e.*, the distance ions structurally or dynamically perturb the hydrogen-bonding network of water molecules. Although a previous report suggests that ions act only locally to directly coordinated water molecules,[14] several opposing results have demonstrated that interactions persist into extended hydration shells.[15–27] Small-angle x-ray scattering experiments indicate an increased water molecule density with respect to bulk water surrounding SO_4^{2-} and PO_4^{3-} extending to ~2.9 and ~3.6 Å, respectfully.[28] More recently, long-distance perturbations as a result of ion-water interactions were reported using terahertz spectroscopy, which showed that tri- and tetraanionic hexacyanoferrates, $Fe(CN)_6^{3-}$ and $Fe(CN)_6^{4-}$, effect water molecule dynamics beyond the inner coordination shell.[27] An intrinsic complication with solution-phase studies of ion-water interactions is the presence of counterions, which can themselves affect the hydrogen bonding network of water molecules, form ion pairs, and otherwise shield the electrostatic interactions with water. Furthermore, the high ionic concentrations typically required for adequate signal lead to close ion-ion proximities with potentially overlapping solvation shells and ion pairing. To overcome these issues, aqueous droplet studies have emerged as a useful means to investigate the physical and chemical properties of ions while excluding influence from cosolutes in order to provide information about effects of an individual ion on the hydrogen bonding network of water molecules in the effective limit of infinite dilution.

Ion-containing aqueous clusters of $X^-(H_2O)_n$ can be readily formed *via* nanoelectrospray ionization of aqueous solutions. The structure of droplets containing SO_4^{2-} have been extensively studied between $n = 3 - 24$.[29–32] For instance, photoelectron spectroscopy of $SO_4^{2-}(H_2O)_n$ has shown that formation of water-water hydrogen bonds are favored over ion-water bonding after $n > 4$ due to sufficient shielding of the negative charges.[33] Comparison of infrared photodissociation (IRPD) spectroscopy to computational structures for $n = 6$ has revealed formation of cyclic water rings.[32] Similarly, IRPD measurements for the structure of $n = 12$, which has an enhanced abundance in the mass spectrum with respect to the neighboring hydration sizes, suggests a highly symmetrical structure is adopted with nine water molecules in the first solvation shell.[29] The lowest energy structures for the $n = 11$ and $n = 13$ clusters are described by either removal or addition of a single water molecule from the structural motif present in the especially stable $n = 12$ cluster.

Long-distance ion-water interactions in aqueous droplets can be measured as a function of size by investigating the structural orientation of surface water molecules, which preferentially orient with their dipoles facing inward as a result of interactions with the solvated anion.[23–26] Previous measurements of nanodroplets containing SO_4^{2-} show that the structure of the hydrogen bonding network is perturbed up to ~0.7 nm.[24] Further studies on the multivalent hexacyanoferrates $Fe(CN)_6^{3-}$ and $Fe(CN)_6^{4-}$ result in ion-water interactions persisting to ~0.8 and ~1.0 nm, respectfully.[25,26] These experiments were performed with the instrument cooled to 133 K in order to slow the dissociation of droplets due to rapid water molecule evaporation. However, relevant atmospheric temperatures are ~180 K for mesospheric and ~220 K for stratospheric aerosols. Therefore, a structural investigation of aqueous droplets as a function of temperature could provide information regarding their structure and stability as well as the extent of ion-water interactions within droplets that more closely resemble nascent atmospheric aerosols.

Herein, we investigate the temperature dependence of ion-water interactions in aqueous sulfate nanodrops, $SO_4^{2-}(H_2O)_n$, between $n = 30 - 55$. Mass spectral measurements reveal specific cluster sizes, n, with enhanced abundance attributed to a unique hydrogen-bonding structures that remain with temperatures elevated above ambient conditions. Remarkably, structural ion-water interactions between the solvated SO_4^{2-} and water molecules residing at the droplet surface persist up to 340 K in $n = 30$, which suggests that these long range interactions are prevalent at ambient atmospheric conditions. These experiments are the first temperature-dependent studies of extensively hydrated anions and provide new insight into fundamental intermolecular properties that exist at relevant atmospheric temperatures.

4.2 Experimental Methods

4.2.1 Mass Spectra

All experimental data were acquired using a home-built 7.0 T Fourier transform ion cyclotron resonance (FT-ICR) mass spectrometer that has been modified from an instrument described in detail elsewhere to incorporate a 7.0 T magnet.[34] Briefly, hydrated ions are formed *via* nanoelectrospray ionization (nESI) of 5 mM aqueous solutions of copper sulfate (Fischer Chemical, Fair Lawn, NJ) using Milli-Q purified water (Millipore, Billerica, MA). Solutions are loaded into borosilicate capillaries (Sutter Instrument, Novato, CA) with tips pulled to an inner diameter of ∼1 µm. The hydrated ions are formed by applying ∼700 V (relative to the entrance capillary of the mass spectrometer) to a platinum wire that is inserted into the solution. The emitter tip is positioned ∼1 mm from the heated (∼80 °C) metal entrance capillary of the mass spectrometer.

Ions are guided *via* a set of electrostatic lenses through five stages of differential pumping toward the ion cell, which is surrounded by a copper jacket.[35] The jacket is temperature-regulated to within ± 3 K using a solenoid controlled with home-built regulation software to time pulses of liquid nitrogen for cooling, or with a resistive blanket wrapped around the vacuum chamber containing the cell for heating. The copper jacket is thermalized to the set temperature for at least ∼8 h prior to data acquisition. A pulse of dry nitrogen gas is introduced during ion accumulation to bring the cell region to $\sim 2 \times 10^{-6}$ Torr, which assists in both the trapping and thermalization of ions. After ∼6 s, the cell pressure returns to $\sim 5 \times 10^{-9}$ Torr. Precursor ions are isolated using a stored waveform inverse Fourier transform excitation and can thereafter be activated by IRPD prior to detection to measure photon energy dependent dissociation kinetics for acquiring infrared spectra. A weighted average ensemble method, in which three consecutive cluster sizes are isolated, is implemented to improve the signal-to-noise ratios of these measurements.[36] This technique uses the *average* dissociation kinetics of the precursor ensemble instead of the dissociation rate of a single nanodrop size. To clearly specify an ensemble distribution versus a single nanodrop size, the notation n_e is used to represent an $n \pm 1$ ensemble, *i.e.*, $n_e = 45 \equiv n = 44 - 46$.

4.2.2 Infrared Spectroscopy

IRPD spectra between 3000 and 3800 cm^{-1} are measured using infrared photons from a tunable OPO/OPA system (LaserVision, Bellevue, WA) pumped by the 1064 nm fundamental of a Nd:YAG laser (Continuum Surelight I-10, Santa Clara, CA) operating at a 10 Hz repetition rate. Ions are irradiated between 0.25 – 1.0 s to acheive substantial, but not complete, dissociation of the precursor distribution. Using the ensemble method,[36] a first-order dissociation rate constant is calculated from the weighted average of products with respect to the initial precursor distribution. IRPD rate constants are corrected for dissociation due to the absorption of blackbody photons originating from the instrument walls by subtracting the blackbody infrared dissociation (BIRD) rate constant, which is measured separately in the absence of infrared radiation. IRPD rate constants are also corrected for frequency dependent variations in laser power.

4.3 Results and Discussion

4.3.1 Magic Number Clusters

nESI of a 5 mM aqueous copper sulfate solution produces ion-containing aqueous droplets over a broad size range (Figure 4.1). Both $SO_4^{2-}(H_2O)_n$ and $HSO_4^-(H_2O)_n$ are produced at 135 K (Figure 4.1a) and at 360 K (Figure 4.1b). The largest clusters observed at these temperatures are $n \simeq 125$ for $SO_4^{2-}(H_2O)_n$ and $n \simeq 35$ for $HSO_4^-(H_2O)_n$. The smallest clusters detected are limited by the excitation waveform conditions used in these experiments. Thermodynamic stabilities for small clusters of $SO_4^{2-}(H_2O)_n$ and $HSO_4^-(H_2O)_n$ have been extensively investigated previously.[37–40] Cluster distributions at both high and low temperatures can be shifted to larger or smaller values of n by adjusting the ion excitation waveforms, the entrance capillary temperature and potentials applied to source optics.

The relative abundances of $SO_4^{2-}(H_2O)_n$ nanodrops with $n = 24, 36, 39, 56, 58$ at low temperature (Figure 4.1a) are anomalously high relative to the neighboring hydration states. At higher temperature (Figure 4.1b), the $n = 24, 36$ and 39 clusters remain more prominent in abundance, but the $n = 56$ and 58 clusters much less so. Enhanced abundances, commonly referred to as magic number clusters (MNCs), originate from either a higher stability of the nanodrop at that size or an inherent instability of the neighboring $n + 1$ cluster. MNCs have been previously observed with a diverse range of hydrated species, including the hydrated electron,[41,42] hydrated proton,[43,44] monatomic ions,[45,46] small organic ions,[47–50] transition metal complexes[25,26] and peptides.[51] Previous photodissociation experiments and theory have revealed the presence of pentagonal dodecahedral clathrate structures leading to enhanced stability in $n = 20$ hydrates of H_3O^+, NH_4^+, Cs^+, Rb^+, and K^+.[44,46,48,49] Similar cage-like structural motifs may be responsible for the enhanced abundance of the observed $SO_4^{2-}(H_2O)_n$ MNC droplets. There are also alternating MNCs between $n = 49 - 58$ for $(H_2O)_n^-$,[41,42] $H^+(H_2O)_n$,[52] protonated amines,[43,50] and halides,[45] which alternatively suggests that $SO_4^{2-}(H_2O)_n$ clusters at $n = 56$ and 58 may originate from the inclusion of SO_4^{2-}

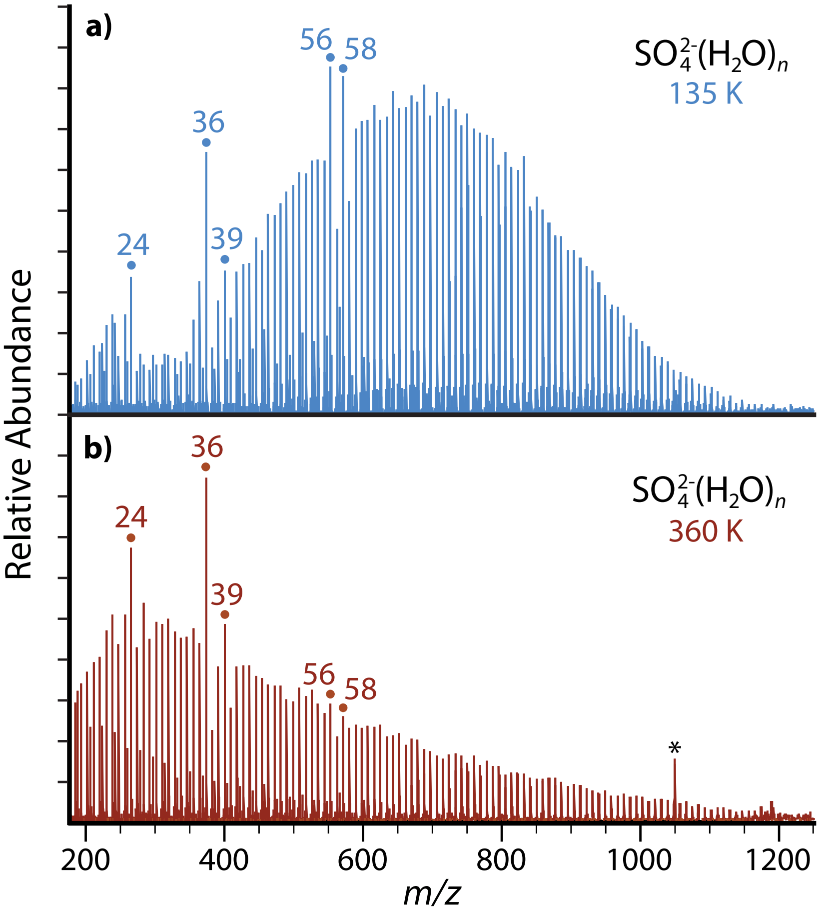

Figure 4.1: Nanoelectrospray mass spectrum acquired from 5 mM aqueous copper sulfate with the copper jacket temperature (a) cooled to 135 K or (b) elevated to 360 K. Magic number clusters of $SO_4^{2-}(H_2O)_n$ with n = 24, 36 and 39 are prominent for both temperatures. Frequency noise is labeled with an asterisk ($*$).

into similar structural motifs without significantly disrupting the enhanced structure of the hydrogen bonding network. The continued presence of MNCs with $n = 24, 36$ and 39 at high temperature in these experiments suggests these stable configurations may be relevant to nascent aerosols at ambient atmospheric temperatures.

4.3.2 Temperature-Dependence of Bonded O–H Stretches

To investigate the hydrogen bonding network and water molecule orientations as a function of temperature, IRPD spectra were acquired for $SO_4^{2-}(H_2O)_n$ with $n_e = 45$ and with the copper jacket between 135 – 215 K (Figure 4.2). The broad feature spanning ~3000 – 3650 cm^{-1} is characteristic of absorptions from hydrogen-bonded O—H stretches. This region

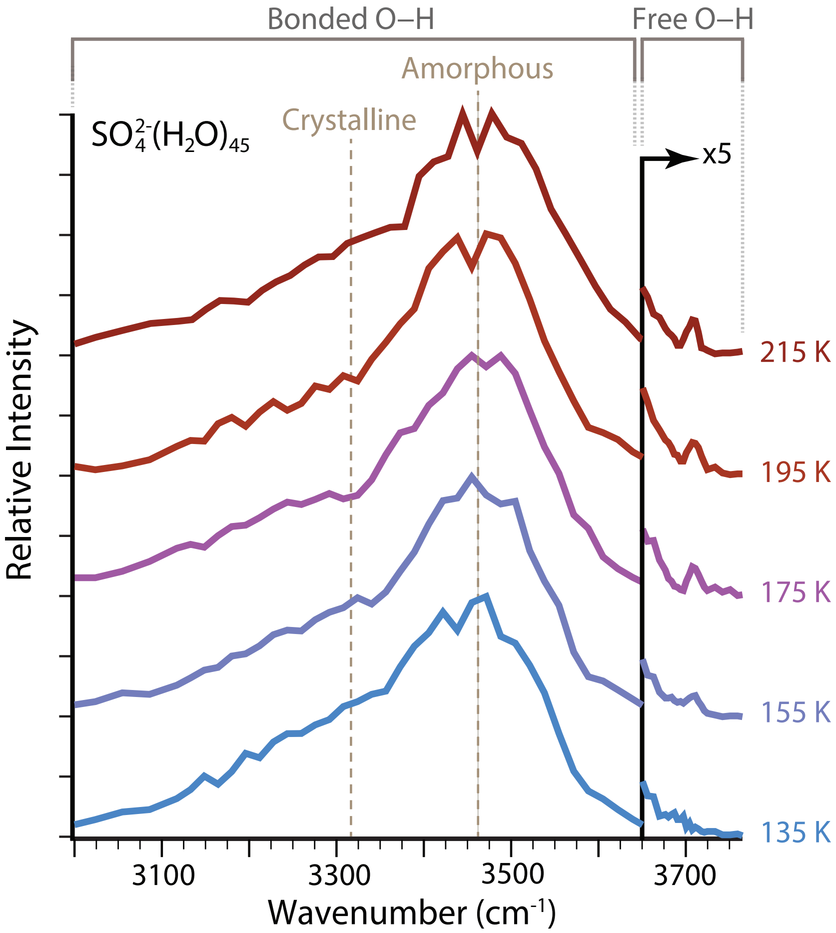

Figure 4.2: Full O—H stretching region for IRPD of $SO_4^{2-}(H_2O)_n$ with $n_e = 45$ and copper jacket temperatures thermalized between 135 – 215 K.

can be further subdivided based on the local colligative physical state of water molecules, which depends on both the number of hydrogen bonds involved and the O—H—O angles for hydrogen bonding.[53] In the bulk phase, water molecules that accept and donate two hydrogen bonds (**AADD**: acceptor-acceptor-donor-donor) in a near-optimal, *i.e.* O—H ∥ O—O, four-coordinate tetrahedral conformation, absorb low energy photons near ∼3300 cm^{-1} and are referred to as crystalline ice.[54,55] Amorphous ice, or liquid-like water, has blue-shifted hydrogen bonding oscillators at ∼3400 – 3500 cm^{-1}, in which either four-coordinate water molecules adopt less-optimal distorted tetrahedral structures than crystalline ice, or the water molecules are three-coordinate (**ADD**: acceptor-donor-donor). The relative ratios of these two regions have been explored as a function of droplet size for both neutral water and ion-containing droplets up to $n = 550$.[22,56] Although small nanodroplets with $n = 30 - 55$ do not have a discrete phase, the absorptive regions observed in bulk water can be used to describe changes in the composite structure of the hydrogen bonding network as a function of hydration.

Table 4.1: Gaussian fitting parameters for IRPD spectra of $SO_4^{2-}(H_2O)_n$ with $n_e = 45$. Parameters for amorphous and crystalline ice are given with subscripts *amor* and *crys*, respectively, for $f(x) = a \cdot exp[-((x-b)/c)^2]$. The ±% for 2σ standard error is provided as a relative percentage in parentheses following the parameter, (%).

	a_{amor}	b_{amor}	c_{amor}	a_{crys}	b_{crys}	c_{crys}
135 K	0.0787 (10)	3470 (0.1)	96.23 (7.5)	0.0570 (8.0)	3323 (0.5)	199.6 (6.3)
155 K	0.0987 (6.3)	3472 (0.1)	89.73 (5.6)	0.0571 (6.6)	3327 (0.4)	206.1 (5.1)
175 K	0.0823 (2.9)	3476 (0.1)	92.15 (3.5)	0.0467 (4.1)	3324 (0.4)	220.1 (4.6)
195 K	0.0977 (9.3)	3468 (0.1)	97.13 (7.3)	0.0425 (13)	3325 (0.8)	204.9 (9.2)
215 K	0.0794 (10)	3477 (0.1)	99.50 (8.2)	0.0436 (11)	3325 (0.8)	210.7 (8.2)

Temperature-dependence of the amorphous to crystalline hydrogen bonding ratio for $SO_4^{2-}(H_2O)_n$ with $n_e = 45$ was calculated by fitting the bonded O—H region with two Gaussian lineshapes for absorptions centered at ~3470 cm^{-1} and ~3320 cm^{-1}, respectively. Fitting parameters for these lineshapes are provided in Table 4.1. There is no systematic change in the width for these two absorptive regions across the temperature range investigated. There is a minor blue shift by $\Delta\nu = 7$ cm^{-1} from 3470 cm^{-1} to 3477 cm^{-1} for the center frequency of amorphous hydrogen bonding across the temperatures measured, while the crystalline center blue shifts from 3323 cm^{-1} to 3325 cm^{-1}, a difference of only $\Delta\nu =$ 2 cm^{-1}. The largest systematic change is the ratio of relative abundances for these two lineshapes. Using the integrated areas of the Gaussian lineshapes, the hydrogen bonding network composition for $n_e = 45$ is ~40% amorphous at 135 K and becomes less crystalline as the copper jacket temperature is elevated, which results in a monotonic increase of the amorphous contribution to ~46% at 215 K. Because the intensity of absorptive bands can depend nonlinearly on single photon absorption cross sections using IRPD,[57] these integrated bands may not represent quantitative values. However, the monotonic increase in the ratio for crystalline to amorphous bands as a function of temperature is independent of this nonlinearity. Therefore, we conclude that increased temperature leads to nanodrop structures with less optimal O—H—O angles and decreased coordination.

4.3.3 Temperature-Dependence of Long-Distance Interactions

Information about the extent of ion-water interactions between the solvated SO_4^{2-} and surface water molecules as a function of temperature can be determined from IRPD spectra of $SO_4^{2-}(H_2O)_n$. Dangling or "free" O—H stretches at the surface of the water droplet that do not participate in hydrogen bonding (**A**: acceptor, **AD**: acceptor-donor, or **AAD**: acceptor-acceptor-donor) occur between ~3650 – 3800 cm^{-1}. Water molecules in the first coordination shell orient with their hydrogen atoms facing inward toward solvated anions.[29,32]

This is due to both the Coulombic interaction between the anion and the partial positive charge of the hydrogen atoms and to hydrogen-bonding between water and the solvated anion. These interior water molecules donate both hydrogen atoms for hydrogen bonding to either the solvated anion or other water molecules (**DD**, **ADD**, or **AADD**). With subsequent solvation shells or increasing n, the distance between the anion and surface water molecules lengthens and the magnitude of interactions resulting in surface patterning diminishes. This decreasing impetus for water molecules to orient inward is eventually overcome by both the entropic drive to incorporate free O—H water molecules and the enthalpic drive to optimize hydrogen bonding at the surface as observed in neutral and cationic clusters. Therefore, the onset of spectroscopic features at ~3700 cm^{-1} measured as a function of n provides an effective distance to which the anion can strongly orient water molecules at the droplet surface.

In the IRPD spectra of $\text{SO}_4^{2-}(\text{H}_2\text{O})_n$ with $n_e = 45$ and T = 135 K (Figure 4.2), all of the spectral intensity between 3650 – 3800 cm^{-1} is attributable to the shoulder of the hydrogen-bonding feature centered at 3470 cm^{-1}, consistent with previous size-dependent experiments of SO_4^{2-} at low temperature.[24] A distinct band at ~3707 cm^{-1} emerges at 155 K and gradually increases in intensity with temperature, indicating that there are an increasing number of free O—H oscillators at the surface. Therefore, although the surface of $n_e = 45$ is composed entirely of inward doubly donating water molecules at 135 K, these nanodrops begin to incorporate free O—H water molecules at 155 K, where the free O—H reorientation becomes competitive with long distance ion-water interactions between SO_4^{2-} and the surface. It is important to note that the onset of the free O—H does not equivocate to a complete loss of interaction between the anion and surface, but rather the onset for the loss of strong *structural* orientation at the surface.

The appearance of free O—H oscillators in $\text{SO}_4^{2-}(\text{H}_2\text{O})_n$ clusters with n_e between $35 - 55$ and copper jacket temperatures between 135 – 175 K was measured (Figure 4.3). The free O—H **ADD** stretch at ~3707 cm^{-1} that is not present for $n_e = 45$ appears at $n_e = 50$, and the intensity increases for $n_e = 55$. The ion-water distance between the solvated anion and surface water molecules, which can be calculated from the density of water with the assumption that clusters are spherical, is approximately 0.71 nm for $n_e = 50$. Therefore, the strong structural influences from SO_4^{2-} extend to ~0.71 nm when the copper jacket is at 135 K. When the copper jacket temperature is increased to 155 K, the onset of the free O—H occurs with $n_e = 45$ (~0.69 nm) and therefore, the increased temperature has slightly diminished the distal extent to which SO_4^{2-} can strongly orient water molecules. Similarly, the free O—H band emerges at $n_e = 40$ (~0.66 nm) with the copper jacket at 175 K. This corresponds to a decrease of the orientation extent by ~0.03 nm for each 20 K increase for this size range.

There is no free O—H in the IRPD spectrum of $n_e = 35$ until the copper jacket has reached 295 K (Figure 4.4b). Although the free O—H emergence for clusters between $n_e = 40 - 50$ occurs within a small temperature range ($\Delta\text{T} \simeq 40$ K), the strong ion-water interactions in $n_e = 35$ structure the surface until $\Delta\text{T} \simeq 120$ K with respect to $n_e = 40$. There are MNCs in the precursor distribution of both $n_e = 35$ and 40 at $n = 36$ and 39,

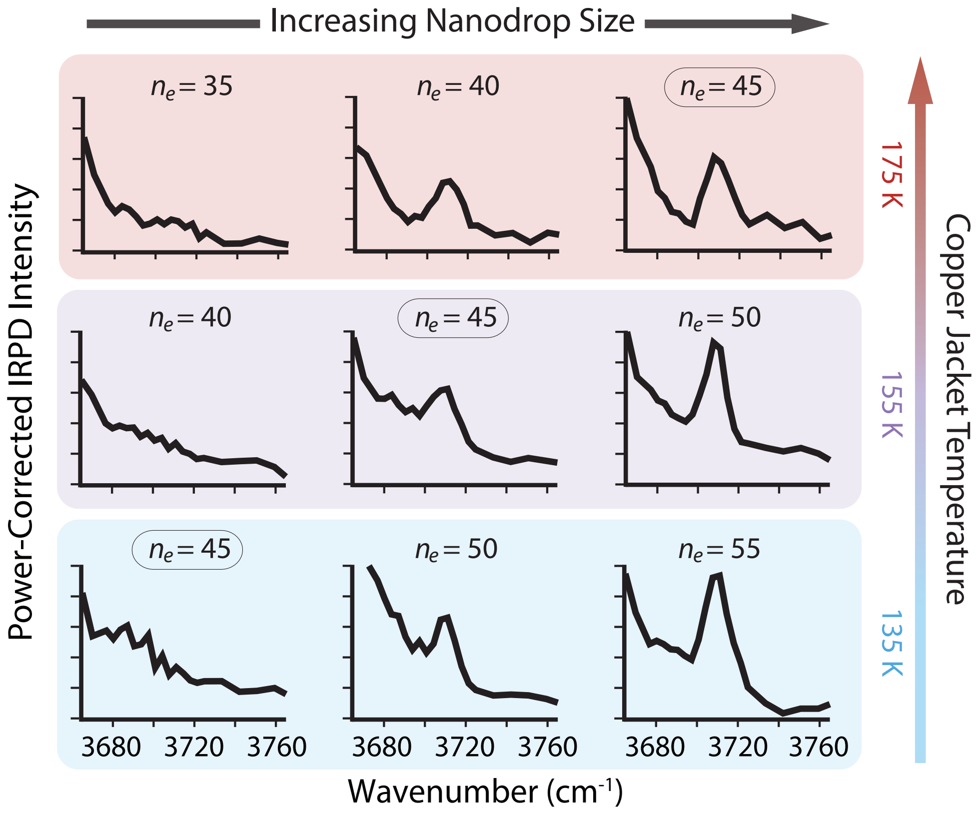

Figure 4.3: Dependence of copper jacket temperature on the appearance of the droplet free O–H band as a function of cluster size between $n_e = 30 - 55$. Within a given cluster size (see $n_e = 45$ above), increasing the temperature results in a greater abundance of the free O—H band, whereas within a static temperature, increased cluster size results in larger free O—H absorbance due to the decreased Coulombic interaction orienting the surface.

respectively. Therefore, the large temperature offset is not attributable to an anomalous stability in just one of these precursors. Instead, the increased temperature required for surface reorientation is most likely due to the decreased ion-surface distance that requires higher internal energies to overcome the strong Coulombic interactions. Remarkably, there is no free O—H band for $n_e = 30$ until the ion cell is heated to 340 K (Figure 4.4c). The approximate droplet radii for $n_e = 30$ and 35 are ~0.60 nm and ~0.63 nm, respectively. The inner coordination shell for SO_4^{2-} consists of $n \simeq 14$ water molecules.[30] Thus, the ion-water interactions reported here are each representative of long-range interactions into *at least* a second solvation shell.

There are no MNCs in the $n_e = 30$ ensemble distribution and as a result, the long-distance structural interactions at elevated temperatures observed here are not a consequence of atypical stabilities. Instead, the structural interactions present in these nanodrops are analogous

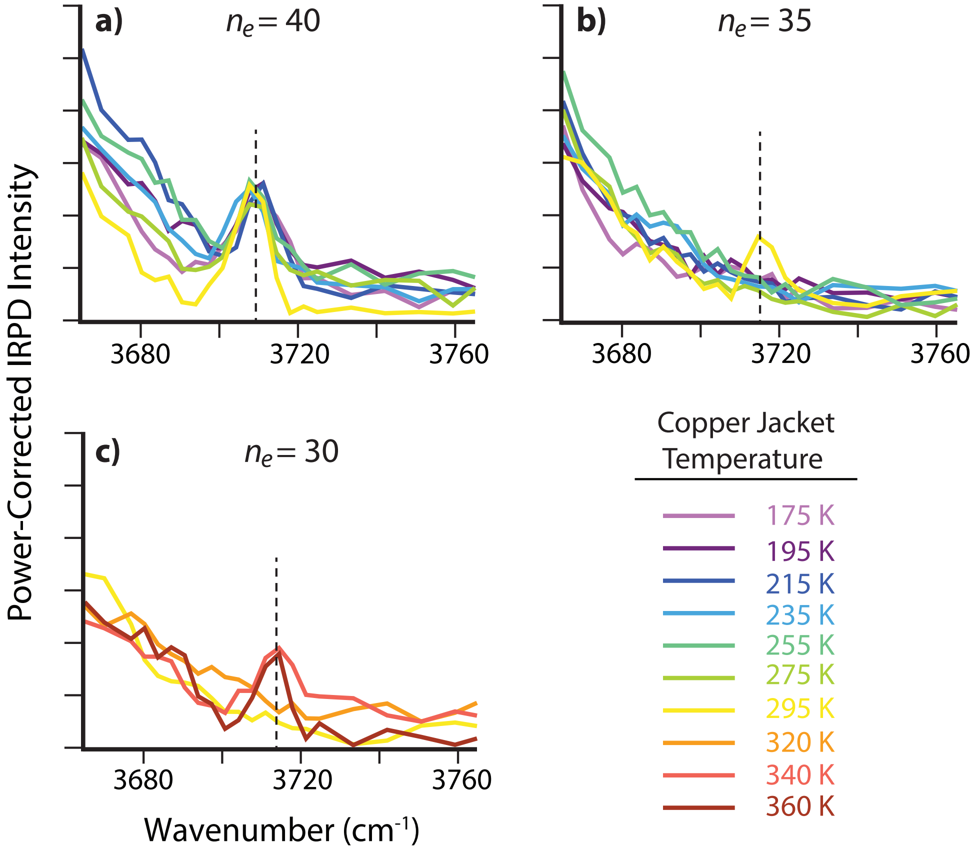

Figure 4.4: IRPD spectra of the free O–H region for $SO_4^{2-}(H_2O)_n$ with (a) $n_e = 40$, (b) $n_e = 35$ and (c) $n_e = 30$ with copper jacket temperatures between $175 - 360$ K.

to ion-water interactions in aqueous solutions at ∼0.60 nm, or roughly a second solvation shell from the anion, and provides evidence for remote structuring of water molecules beyond the inner coordination shell by dianionic species at ambient temperatures. This is consistent with a recent terahertz investigation of tri- and tetraanionic hexacyanoferrates in ambient temperature aqueous solutions that were found to *dynamically* perturb a minimum of ∼19 and ∼25 water molecules, respectively.[27] Although the low pressures in these nanodrop experiments lead to rapid evaporative cooling of the droplets, atmospheric temperatures reach as low as 180 K in the mesosphere, where the unique stability of MNCs and strong ion-water interactions beyond the inner coordination shell may aid nucleation and propagation of nascent atmospheric aerosols.

4.4 Summary and Conclusions

IRPD spectroscopy in the hydrogen bonding region between $3000 - 3800$ cm^{-1} was used to investigate the temperature dependence of ion-water interactions in aqueous $SO_4^{2-}(H_2O)_n$ droplets with instrumental temperatures between $135 - 360$ K. In this spectral region, absorption of photons at $\sim$3700 cm^{-1} is indicative of "free" O—H water molecules at the surface of the droplet that orient one O—H group outward and away from the droplet interior. The appearance of this free O—H band was measured as a function of both temperature and cluster size to determine the onset of diminished structural ion-water interactions at remote distances from the dianion. For a given cluster size, an increase in temperature results in a greater population of free O—H water molecules at the surface as a result of the entropic and enthalpic drives for surface reorientation that are able to overcome the strong Coulombic interaction with increased internal energies. As the cluster size is decreased, higher temperatures are required as a result of decreased ion-surface distances, where greater Coulombic interactions exist between the solvated ion and surface water molecules.

In contrast to solution-phase experiments, which generally require high concentrations and consequentially limit the amount of unperturbed bulk water due to excess counterions, the long distance interactions observed here using anion-containing aqueous nanodrops provide the first unambiguous evidence for remote ion-water interactions by a singular anion at temperatures relevant to Earth's atmosphere. These findings provide new insight into fundamental ion-water interactions that may contribute to favorable nucleation and propagation of nascent aerosols in the upper atmosphere. These same techniques can be used to investigate the temperature dependence of larger anion-containing droplets as well as the hydration of clustered anionic cores. Effective ion temperatures can differ from the copper jacket temperatures reported here as a result of rapid evaporative cooling of the aqueous droplets under low pressure conditions and, to a lesser extent, blackbody distributions arising from the ion cell, which can reach a higher temperature than the copper jacket *via* heat transfer through electrical connections.[35] To extract effective temperatures from steady state ion distributions, extensive modeling of the data presented here is currently underway to account for the extent of evaporative cooling in these droplets.

4.5 References

[1] McNeill, V. F. *Annu. Rev. Chem. Biomol. Eng.* **2017**, *8*, 427–444.

[2] Valsaraj, K. T., Kommalapati, R. R., Eds. *Atmospheric Aerosols: Characterization, Chemistry, Modeling, and Climate*; ACS Symposium Series; American Chemical Society, 2009; Vol. 1005.

[3] Charlson, R. J.; Schwartz, S. E.; Hales, J. M.; Cess, R. D.; Coakley, J. A.; Hansen, J. E.; Hofmann, D. J. *Science* **1992**, *255*, 423–430.

[4] Stier, P.; Seinfeld, J. H.; Kinne, S.; Boucher, O. *Atmos. Chem. Phys.* **2007**, *7*, 5237–5261.

[5] Zhang, Q.; Quan, J.; Tie, X.; Huang, M.; Ma, X. *Atmos. Environ.* **2011**, *45*, 665–672.

[6] Andreae, M. O.; Rosenfeld, D.; Artaxo, P.; Costa, A. A.; Frank, G. P.; Longo, K. M.; Silva-Dias, M. A. F. *Science* **2004**, *303*, 1337–1342.

[7] Han, X.; Guo, Q.; Liu, C.; Fu, P.; Strauss, H.; Yang, J.; Hu, J.; Wei, L.; Ren, H.; Peters, M.; Wei, R.; Tian, L. *Sci. Rep.* **2016**, *6*, 29958.

[8] Tie, X.; Huang, R. J.; Dai, W.; Cao, J.; Long, X.; Su, X.; Zhao, S.; Wang, Q.; Li, G. *Sci. Rep.* **2016**, *6*, 29612.

[9] Andreae, M. O.; Crutzen, P. J. *Science* **1997**, *276*, 1052–1058.

[10] Niemeier, U.; Tilmes, S. *Science* **2017**, *357*, 246–248.

[11] Lohmann, U.; Gasparini, B. *Science* **2017**, *357*, 248–249.

[12] Zhang, R.; Khalizov, A.; Wang, L.; Hu, M.; Xu, W. *Chem. Rev.* **2012**, *112*, 1957–2011.

[13] Lee, S.-H.; Reeves, J. M.; Wilson, J. C.; Hunton, D. E.; Viggiano, A. A.; Miller, T. M.; Ballenthin, J. O.; Lait, L. R. *Science* **2003**, *301*, 1886–1889.

[14] Omta, A. W.; Kropman, M. F.; Woutersen, S.; Bakker, H. J. *Science* **2003**, *301*, 347–349.

[15] Rudolph, W. W.; Irmer, G. *Appl. Spectrosc.* **2007**, *61*, 1312–1327.

[16] Mancinelli, R.; Botti, A.; Bruni, F.; Ricci, M. A.; Soper, A. K. *Phys. Chem. Chem. Phys.* **2007**, *9*, 2959–2967.

[17] Vovk, M. A.; Pavlova, M. S.; Chizhik, V. I.; Vorontsova, A. A. *Russ. J. Phys. Chem. A* **2011**, *85*, 1597–1602.

[18] Stangret, J.; Gampe, T. *J. Phys. Chem. A* **2002**, *106*, 5393–5402.

[19] Buchner, R. *Pure Appl. Chem.* **2008**, *80*, 1239–1252.

[20] Eiberweiser, A.; Nazet, A.; Hefter, G.; Buchner, R. *J. Phys. Chem. B* **2015**, *119*, 5270 – 5281.

[21] Böhm, F.; Sharma, V.; Schwaab, G.; Havenith, M. *Phys. Chem. Chem. Phys.* **2015**, *17*, 19582–19591.

[22] Cooper, R. J.; DiTucci, M. J.; Chang, T. M.; Williams, E. R. *J. Am. Chem. Soc.* **2016**, *138*, 96–99.

[23] O'Brien, J. T.; Williams, E. R. *J. Am. Chem. Soc.* **2012**, *134*, 10228–10236.

[24] O'Brien, J. T.; Prell, J. S.; Bush, M. F.; Williams, E. R. *J. Am. Chem. Soc.* **2010**, *132*, 8248–8249.

[25] DiTucci, M. J.; Heiles, S.; Williams, E. R. *J. Am. Chem. Soc.* **2015**, *137*, 1650 – 1657.

[26] DiTucci, M. J.; Williams, E. R. *Chem. Sci.* **2017**, *8*, 1391–1399.

[27] DiTucci, M. J.; Böhm, F.; Schwaab, G.; Williams, E. R.; Havenith, M. *Phys. Chem. Chem. Phys.* **2017**, *19*, 7297–7306.

[28] Chen, C.; Huang, C.; Waluyo, I.; Weiss, T.; Pettersson, L.; Nilsson, A. *Phys. Chem. Chem. Phys.* **2015**, *17*, 8427–8430.

[29] Thaunay, F.; Hassan, A. A.; Cooper, R. J.; Williams, E. R.; Clavaguéra, C.; Ohanessian, G. *Int. J. Mass. Spectrom.* **2017**, *418*, 15–23.

[30] Thaunay, F.; Clavaguéra, C.; Ohanessian, G. *Phys. Chem. Chem. Phys.* **2015**, *17*, 25935–25945.

[31] Zhou, J.; Ssantambrogio, G.; Brümmer, M.; Moore, D. T.; Wöste, L.; Meijer, G.; Neumark, D. M.; Asmis, K. R. *J. Chem. Phys.* **2006**, *125*, 111102.

[32] Bush, M. F.; Saykally, R. J.; Williams, E. R. *J. Am. Chem. Soc.* **2007**, *129*, 2220–2221.

[33] Wang, X. B.; Nicholas, J. B.; Wang, L. S. *J. Chem. Phys.* **2000**, *113*, 10837–10840.

[34] Bush, M. F.; O'Brien, J. T.; Prell, J. S.; Saykally, R. J.; Williams, E. R. *J. Am. Chem. Soc.* **2007**, *129*, 1612–1622.

[35] Wong, R. L.; Paech, K.; Williams, E. R. *Int. J. Mass. Spectrom.* **2004**, *232*, 59–66.

[36] Prell, J. S.; O'Brien, J. T.; Williams, E. R. *J. Am. Soc. Mass Spectrom.* **2010**, *21*, 800–809.

[37] Wong, R. L.; Williams, E. R. *J. Phys. Chem. A* **2003**, *107*, 10976–10983.

[38] Whitehead, A.; Barrios, R.; Simons, J. *J. Chem. Phys.* **2002**, *116*, 2848–2851.

[39] Xin, Y.; Wang, X. B.; Wang, L. S. *J. Phys. Chem. A* **2002**, *106*, 7607–7616.

[40] Gao, B.; Liu, Z. *J. Chem. Phys.* **2005**, *123*, 224302.

[41] Ma, L.; Majer, K.; Chirot, F.; Issendorff, B. v. *J. Chem. Phys.* **2009**, *131*, 144303.

[42] Knapp, M.; Echt, O.; Kreisle, D.; Recknagel, E. *J. Phys. Chem.* **1987**, *91*, 2601–2607.

[43] Lee, S.-W.; Freivogel, P.; Schindler, T.; Beauchamp, J. L. *J. Am. Chem. Soc.* **1998**, *120*, 11758–11765.

[44] Miyazaki, M.; Fujii, A.; Ebata, T.; Mikami, N. *Science* **2004**, *304*, 1134–1137.

[45] Chakrabarty, S.; Williams, E. R. *Phys. Chem. Chem. Phys.* **2016**, *18*, 25483–25490.

[46] Cooper, R. J.; Chang, T. M.; Williams, E. R. *J. Phys. Chem. A* **2013**, *117*, 6571–6579.

[47] Sekimoto, K.; Takayama, M. *J. Mass Spectrom.* **2011**, *46*, 50–60.

[48] Diken, E. G.; Hammer, N. I.; Johnson, M. A.; Christie, R. A.; Jordan, K. D. *J. Chem. Phys.* **2005**, *123*, 164309.

[49] Chang, T. M.; Cooper, R. J.; Williams, E. R. *J. Am. Chem. Soc.* **2013**, *135*, 14821–14830.

[50] Lee, S.-W.; Cox, H.; Goddard, W. A.; Beauchamp, J. L. *J. Am. Chem. Soc.* **2000**, *122*, 9201–9205.

[51] Rodrigez-Cruz, S. E.; Klassen, J. S.; Williams, E. R. *J. Am. Soc. Mass Spectrom.* **1999**, *10*, 958–968.

[52] Schindler, T.; Berg, C.; Niedner-Schatteburg, G.; Bondybey, V. E. *Chem. Phys. Lett.* **1996**, *250*, 301–308.

[53] Buch, V.; Devlin, J. P. *J. Chem. Phys.* **1999**, *110*, 3437–3443.

[54] Brubach, J. B.; Mermet, A.; Filabozzi, A.; Gerschel, A.; Roy, P. *J. Chem. Phys.* **2005**, *122*, 184509.

[55] D'Arrigo, G.; Maisano, G.; Mallamace, F.; Migliardo, P.; Wanderlingh, F. *J. Chem. Phys.* **1981**, *75*, 4264.

[56] Pradzynski, C. C.; Forck, R. M.; Zeuch, T.; Slaviček, P.; Buck, U. *Science* **2012**, *337*, 1529–1532.

[57] Prell, J. S.; Correra, T. C.; Chang, T. M.; Biles, J. A.; Williams, E. R. *J. Am. Chem. Soc.* **2010**, *132*, 14733–14735.

Chapter 5

Calculating the Steady State Effective Temperatures of Aqueous Sulfate Nanodrops *via* Master Equation Modeling

This chapter is reproduced with permission from:

Matthew J. DiTucci, Christiane N. Stachl, and Evan R. Williams

"Calculating the Steady State Effective Temperatures of
Aqueous Sulfate Nanodrops via Master Equation Modeling",
Manuscript in Preparation for Submission, **2017**.

5.1 Introduction

Mass spectrometric studies of aqueous ion-containing nanodrops have emerged as an effective means for measuring the physical and chemical properties of solvated ions, including hydration structure,[1,2] water molecule binding energies,[3,4] electrochemical values,[5,6] and remote ion-water interactions.[7–9] One primary goal of ion-containing droplet studies has been to relate their properties to various real-world systems, such as bulk solutions, atmospheric aerosols, and the confined environments in vesicles or reverse micelles. For instance, absolute reduction enthalpies measured *via* capture of a thermal electron have been measured as a function of droplet size and extrapolated to infinitely large droplets for relation to absolute half cell potentials in bulk solution.[6] Infrared absorption bands also approach their bulk values as droplets become increasingly larger, *e.g.*, water molecule O—H stretches at the droplet surface approach bulk sum-frequency generation values.[10,11] Recent droplet measurements have suggested remote ion-water interactions can extend one nanometer from the ion into a fourth solvation shell,[9] which is in contention with bulk phase reports that claim ions may only pattern water molecules locally.[12,13] In order to accurately relate ion-water interactions in gas-phase nanodrops to bulk solutions at room temperature or to aerosols in Earth's atmosphere, an effective temperature for the aqueous droplets must be known.

Aqueous nanodrops can rapidly lose internal energy through the evaporation of water molecules, *i.e.*, evaporative cooling, which liberates energy equivalent to the dissociation barrier as well as the kinetic energy partitioned into the departing water molecule.[14] As an example, rapid evaporative cooling of $Cu^{2+}(H_2O)_{400}$ has been modeled after deposition of internal energy *via* absorption of ultraviolet radiation.[4] Upon photoexcitation with a 193 nm photon, the droplets reach a maximum temperature of ∼550 K and quickly return to their equilibrium temperature of ∼130 K by loss of only thirteen water molecules. With respect to a thermal Boltzmann distribution of precursor ions, these evaporative events occur more rapidly at the high energy tail, where the microcanonical rate for dissociation, k_d, is much faster relative to ions with lower internal energies. Under low-pressure conditions, such as ion storage cells in mass spectrometers, energy transfer between ions *via* neutral collisions with background gas is negligible in comparison to photon emission or absorption from the surrounding blackbody field,[15] *i.e.*, $k_{coll,-1} \ll k_{rad,-1}$, where $k_{coll,-1}$ and $k_{rad,-1}$ are the rates of energy loss through neutral collisions or photon emission, respectively. This means that complexes with internal energies above the threshold for dissociation will be trapped in an activated state unless $k_{rad,-1}$ is kinetically faster than k_d. Large ions of mass ∼1.6 kDa can rapidly exchange energy with the blackbody field and therefore maintain thermal equilibrium with their surroundings.[16] However, smaller ions have radiative rates that are much slower or on the same order as k_d, which leads to a fast depletion of ion populations in the high energy tail.[17,18] Therefore, steady state precursor distributions can have average internal energies that are much cooler than their surroundings. In order to model thermal distributions for precursor ions investigated in gas-phase experiments, the microcanonical rate constants for photon absorption, $k_{rad,1}$, photon emission $k_{rad,-1}$, and dissociation, k_d, must be calculated to determine internal energy populations between ion accumulation and detection. This method is commonly referred to as master equation modeling, and has been used previously to calculate binding enthalpies from low-pressure Arrhenius values.[16,19–24]

Recent infrared photodissociation (IRPD) experiments in a low-pressure ion cell have been performed for aqueous $SO_4^{2-}(H_2O)_n$ clusters with $n = 30 - 55$ and as a function of temperature between $115 - 360$ K.[25] For $n = 45$ at 135 K, the surface of these nanodrops is populated only by inward-facing water molecules that donate two hydrogen bonds to other water molecules. By monitoring the emergence of a "free" O—H band near ∼3700 cm^{-1} as a function of temperature, the onset of diminishing structural interactions between the ion and surface can be measured unambiguously to determine the distal extent of ion-water interactions.[7–9] For instance, the free O—H band for $n = 45$ emerges at 155 K and increases in intensity with increasing temperature as the droplet surface becomes more populated with these oscillators. Remarkably, the $n = 30$ droplet, which corresponds to a distance of ∼0.6 nm from the dianion, does not have any free O—H oscillators until 340 K. However, the temperatures reported in these experiments are measured on a thermal copper jacket that surrounds the ion cell,[23] and therefore does not take into consideration the actual temperature of the ion cell or evaporative cooling of the precursor ion population.

Herein, we investigate the effective temperatures of $SO_4^{2-}(H_2O)_n$ nanodrops with $n = 30-45$ using calibrated ion cell temperatures between $186-360$ K. Extensive master equation modeling is used to fit experimentally measured rates of dissociation due to interaction with the surrounding blackbody field under low pressure conditions. We find that evaporative cooling of the $n = 30$ precursor distribution leads to only small temperature offsets of ΔT

$\simeq 20 - 40$ K for the coolest temperatures investigated, but results in significantly larger offsets when the ion cell is heated to 340 K ($\Delta\mathrm{T} \simeq 160 - 180$ K). In association with the previous IRPD measurements for droplets of this size,[25] we conclude that long range structural interactions can indeed persist to temperatures relevant to aerosols in the upper atmosphere. These experiments and associated calculations represent the first report for the effective temperature of aqueous ion-containing droplets under low pressure conditions and can be extended to other ion storage traps operating in ultra-low vacuum.

5.2 Experimental Methods

5.2.1 Mass Spectra

All mass spectral data was acquired using a home-built 7.0 T Fourier transform ion cyclotron resonance (FT-ICR) mass spectrometer that has been upgraded to incorporate the higher magnetic field strength through adaptation of a previous 2.75 T design, which is described with more detail in Bush *et al.*[26] To summarize, aqueous solutions of 5 mM copper sulfate (Fischer Chemical, Fair Lawn, NJ) prepared with Milli-Q purified water (Millipore, Billerica, MA, U.S.A.) are loaded into borosilicate capillaries (Sutter Instrument, Novato, CA) that are pulled to an inner diameter of ∼1 µm. A platinum wire in contact with the solution is held at a potential of ∼700 V, with respect to the heated (∼80 °C) entrance capillary of the instrument, to generate a broad range of hydrated ions *via* nanoelectrospray ionization (nESI). These hydrated ions are guided with electrostatic lenses and five stages of differential pumping to the ion cell, which is temperature-regulated using a surrounding copper jacket.[23] Ions are accumulated by raising a shutter mechanism preceding the ion cell for ∼8 s, during which time a pulse of dry nitrogen gas brings the cell region to 10^{-6} Torr for both thermalization and assisted trapping of the hydrated ions. The cell region is subsequently pumped down to 10^{-9} Torr over ∼6 s prior to ion detection. Precursor ions are isolated thereafter using a stored waveform inverse Fourier transform excitation.

In-house regulation software is used to trigger a solenoid to time pulses of liquid nitrogen flowing around the copper jacket for cooling the ion cell to within ± 2 K. A resistively heated blanket surrounding the magnet bore is used to elevate the ion cell above room temperature to within ± 1 K. The copper jacket is allowed to thermalize for at least ∼8 h prior to data acquisition. Reported temperatures have been calibrated for the center of the ion cell to account for thermal transfer of heat along excite and detect lines attached to the ambient flange and/or external blackbody photons entering *via* the backside $\mathrm{CaF_2}$ window.[23]

5.2.2 Blackbody Dissociation Kinetics

A stored waveform inverse Fourier transform (SWIFT) was used to isolate precursor ensembles consisting of three successive hydration sizes, $n \pm 1$, in order to significantly improve the product signal-to-noise ratio.[27] Blackbody infrared photodissociation (BIRD) kinetics were measured using a weighted average of the isolated distribution before and after a delay time of $0.25 - 1.0$ s, through which time hydrated ions absorb blackbody photons originating from the thermalized ion cell and instrument walls. This method results in an *average* rate for water molecule loss from the precursor ensemble instead of kinetics for loss from a single hydrate. To clearly specify an ensemble distribution versus a single nanodrop size, the notation n_e is used to represent an $n \pm 1$ ensemble, *i.e.* $n_e = 45 \equiv n = 44 - 46$. All experimental BIRD data, with the exception of $n_e = 30$ for temperatures between $135 - 255$ K, has been extracted from data published previously, which instead focuses on infrared photodissociation.[25]

5.2.3 Calculations

An initial geometry for $SO_4^{2-}(H_2O)_{30}$ was obtained using Desmond 3.1 (Schrödinger, Inc., Portland, OR) and simulated annealing molecular dynamics were performed as described elsewhere.[9] Briefly, an initial geometry relaxation precedes 1 ns of stochastic dynamics with 1 fs time steps at 135 K using the OPLS2005 force field. A series of 20 annealing cycles comprised of 200 ps at 195 K, linear cooling to 135 K over 300 ps, and 1 ns equilibration at 135 K are used to sample low-energy structures over an increased conformational space. Using the geometry of the lowest energy conformer, the structure was minimized and harmonic frequencies were calculated using Q-Chem 4.0 (Q-Chem, Inc., Pittsburgh, PA) at the B3LYP/LACVP++** level of theory.[28] These frequencies are used to calculate rate of photon absorption and emission as well as generate transition state (TS) frequencies for water molecule loss. For larger $SO_4^{2-}(H_2O)_n$ clusters, a scaling method is used whereby frequencies and associated intensities calculated for $n = 30$ are duplicated in evenly spaced increments to generate a final set of frequencies with the correct degrees of freedom. The TS frequencies are generated by removing a low energy hydrogen bond stretch attributed to the reactive mode and scaling five other low energy frequencies to simulate the transition of vibrational oscillators to rotational freedom of the departing water molecule.

Master equation modeling was performed using in-house software and has been elaborated more thoroughly in Price *et al.*[19] Summarily, a Boltzmann distribution with defined hydrated ion temperature is used to describe the initial thermalized population of internal energies. The distribution is divided into several energy bins with widths of 2.5 meV and the population of each bin is calculated in 1 ms time steps for $5 - 10$ s through rates of (de)population *via* photon absorption, photon emission, and water molecule loss. Energy transfer *via* collisions is not considered because these events are negligible under the experimental pressures of $< 10^{-8}$ Torr.[15] The unimolecular kinetics, k_{uni}, for population depletion are solved with matrix formalism, in which the individual rates are organized in a transport (or J) matrix. Radiative absorption of a photon, $k_{1,rad}$, results in movement of an ion to a higher energy bin, stimulated or spontaneous radiative emission, $k_{-1,rad}$, leads to movement of an ion to a lower energy bin, and water molecule loss, k_d, which is calculated using RRKM theory, results in removal of an ion from the energy bin:

$$k_{uni} = k_d \left(\frac{k_{1,rad}}{k_{-1,rad} + k_d} \right) \equiv k_{BIRD} \qquad \text{(Equation 5.1)}$$

$$k_{1,rad}(\Delta E_{i \to j} = hv) = \sum_m \rho(hv)\mathbf{B}(hv)P_i^{mhv} \qquad \text{(Equation 5.2)}$$

$$k_{-1,rad}(\Delta E_{j \to i} = hv) = \sum_m \left[\mathbf{A}(hv) + \rho(hv)\mathbf{B}(hv)\right] P_i^{mhv} \qquad \text{(Equation 5.3)}$$

$$k_d = \frac{\sigma \cdot N^{TS}(E - E_0)}{h \cdot \rho(E)} \qquad \text{(Equation 5.4)}$$

where $\rho(hv)$ is the radial energy density calculated from a Planck distribution at the set temperature, $\mathbf{A}(hv)$ and $\mathbf{B}(hv)$ are the Einstein coefficients for stimulated and spontaneous radiative processes, respectively, σ is the degeneracy of the reactive mode, and h is Planck's constant. The coefficient P_i^{mhv} includes two probability factors based on the harmonic oscillator model. This inlcudes the enhanced transmission probability, *i.e.*, absorption from vibrational level $m \to m + 1$ will be $m + 1$ times as probable as that from vibrational level $0 \to 1$, and also the occupation probability, *i.e.*, the likelihood that a vibrational state is populated. The latter factor is calculated using exact state counting,[19] which determines the ratio of possible energy configurations that favorably lead to population of m quanta occupying the v^{th} oscillator with respect to all possible energy configurations at given total energy E. Both the sum of states, $N^{TS}(E - E_0)$, which describes all energy configurations in the TS with total energy $E' = E - E_0$, and the density of states, $\rho(E)$, which defines the complex with total energy E, are also calculated with exact state counting.

5.3 Results and Discussion

5.3.1 Experimental BIRD Measurements.

The rates of water molecule loss from hydrated $SO_4^{2-}(H_2O)_n$ with n_e = 30, 35, 40, and 45 were measured with a range of ion cell temperatures thermalized between 186 − 360 K. These measured rates represent the *average* kinetics of the isolated precursors and their products using the ensemble method,[27] which was chosen instead of a single precursor due to rapid water molecule loss at elevated temperatures that results in complete dissociation of the precursor. Therefore, the reported rates are illustrative of blackbody kinetics for a specific size-regime of aqueous $SO_4^{2-}(H_2O)_n$ and not of a discrete droplet size. The population decay, $ln(P/P_0)$, as a function of time for n_e = 30 with ion cell temperatures between 194 − 261 K is plotted in Figure 5.1. The fits within a single temperature are highly linear (R^2 >

0.99) and the associated slope is used for obtaining the rate of water molecule loss, k_{BIRD}. This slope increases with temperature due to the increased absorption of blackbody photons and higher internal energies of the clusters. A summary of all blackbody dissociation rate constants measured for $n_e = 30-45$ with ion cell temperatures thermalized between 186−360 K is provided in Table 5.1.

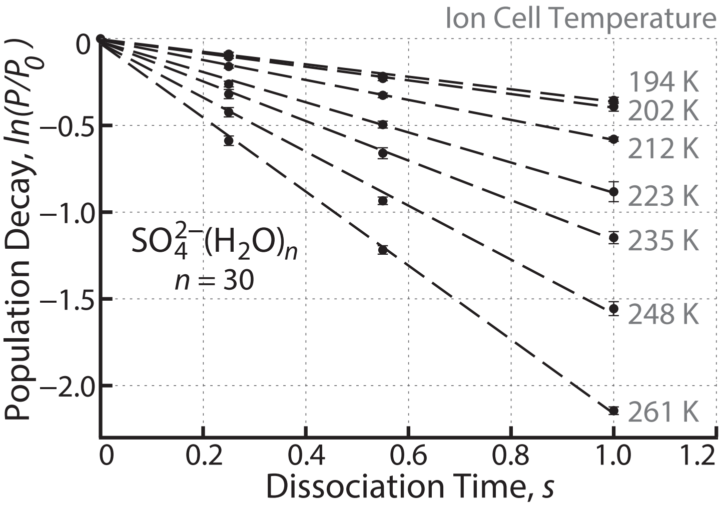

Figure 5.1: Population decay of $SO_4^{2-}(H_2O)_n$ with $n_e = 30$ and with ion cell temperatures between 194 − 261 K corresponding to 0.25 − 1.0 s of blackbody photon dissociation.

Isolated precursors $n_e = 35$ and 40 each contain an especially stable magic number cluster (MNC) in their initial distributions at $n = 36$ and 39, respectively. These MNCs are present for all temperatures measured and therefore, their enhanced stability will contribute to the measured rates for $n_e = 35$ and 40 consistently throughout the measured temperature range. These precursors can provide a useful comparison to $n_e = 30$ and 45, which do not contain MNCs in their initial distributions. Because the ensemble method is dependent on a weighted average of products, a dissociation pathway passing through MNCs for *only* the warmest temperatures can result in a non-linear temperature dependence. A large percentage of the products from $n_e = 30$ between 295 − 360 K (∼26 − 88%, respectively) pass through MNCs at $n = 24$ and 26 (Figure A.7). To avoid dissociation through these stable droplet sizes, only the temperatures between 194 − 261 K, which do not lead to water loss down to $n = 26$, are considered for the temperature-dependent kinetics of $n_e = 30$.

The natural log of blackbody dissociation kinetics, $ln(k_{BIRD})$, for $n_e = 30 - 45$ with respect to the reciprocal temperature of the ion cell is presented in an Arrhenius plot (Figure 5.2). The temperature dependence for water loss from all cluster sizes is linear ($R^2 \geq 0.94$), which shows that for a given initial precursor distribution, n_e, the measured Arrhenius slope is consistent within these temperature ranges using the ensemble method. As noted previously, the difference in slope for $n_e = 30$ with temperatures between 194 − 261 K and

Table 5.1: Blackbody dissociation rate constants for water molecule loss from $n_e = 30 - 45$ with ion cell temperatures between 186 – 360 K. Dissociation rates are given in s^{-1} and standard deviations are provided as relative percentages in parentheses, (%). Rates followed by an asterisk ($*$) have been acquired from a single time measurement, whereas all others have been calculated using the slope from four time points between 0 – 1 s dissociation.

	$n_e = 30$	$n_e = 35$	$n_e = 40$	$n_e = 45$
186 K	—	—	—	0.432* (8.1)
194 K	0.359 (4.9)	—	—	0.410 (3.8)
202 K	0.392 (2.8)	—	0.457 (3.1)	0.585 (5.5)
212 K	0.575 (2.1)	0.595 (9.8)	0.678 (9.0)	1.024 (3.7)
223 K	0.870 (3.5)	0.777 (13.2)	0.927 (1.5)	1.109 (16.0)
235 K	1.141 (2.6)	1.304 (6.5)	1.733 (4.4)	1.794 (6.6)
248 K	1.558 (3.9)	1.769* (2.2)	2.262* (3.0)	—
261 K	2.133 (2.0)	2.531* (2.0)	2.676* (1.8)	—
276 K	—	3.540* (1.4)	4.174* (0.8)	—
295 K	3.303* (1.5)	4.595* (2.1)	5.018* (0.7)	—
320 K	4.695* (4.3)	—	—	—
340 K	5.542* (0.6)	—	—	—
360 K	6.649* (0.8)	—	—	—

295 – 360 K is due to the latter dissociation pathway passing through MNCs at $n = 24$ and 26, which have slower dissociation rates. Only the temperatures between 194 – 261 K will be considered, because these more accurately describe the rate of water molecule loss from $n_e = 30$. The Arrhenius slopes are similar for $n_e = 30$ and 45 ($\Delta m = 43.9$) as well as those for $n_e = 35$ and 40 ($\Delta m = 24.1$). The Arrhenius slope is proportional to the threshold dissociation energy, E_0, required for water molecule loss and therefore, this suggests a higher internal energy is required for water evaporation from the distributions containing MNCs. These experiments are performed at the zero-pressure limit ($< 10^{-8}$ Torr), where collisions with background gas are minimal and therefore do not contribute to rapid exchange of energy between ions in the distribution.[15] As a result, the slope in this Arrhenius plot is equal to the *zero-pressure* activation energy, E_a/R, whereas the y-intercept designates the *zero-pressure* pre-exponential factor, A, which differ from the corresponding *high-pressure* values.

5.3.2 Modeling Threshold Dissociation Energies.

The corresponding *high-pressure* threshold dissociation energies and pre-exponential factors, E_0 and A^{∞}, can be extracted by fitting calculated unimolecular kinetics from master equation modeling to the measured blackbody dissociation kinetics. To fit the experimental data with modeled values, an initial Boltzmann distribution is allowed to react *via* radiative absorption and emission or water molecule evaporation using three initial ion temperatures

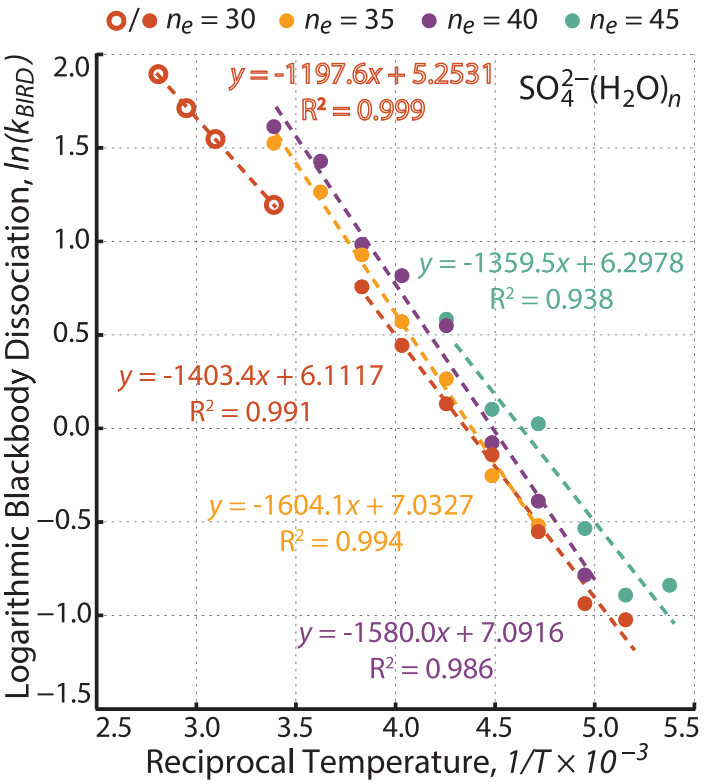

Figure 5.2: Arrhenius plot for temperature-dependent blackbody dissociation of $SO_4^{2-}(H_2O)_n$ with $n_e = 30, 35, 40, 45$. The warmest temperatures for $n_e = 30$ (open circles) have decreased slope with respect to the cooler temperatures (closed circles) due to MNCs along the dissociation pathway.

(including the highest and lowest ion cell temperatures measured) for each n_e. An example of output from master equation modeling is shown for $SO_4^{2-}(H_2O)_n$ with $n_e = 30$ using an ion cell temperature of 194 K (Figure 5.3a). At $t = 0$, the hydrated ion distribution is in thermal equilibrium with the instrument walls and is therefore modeled as a Boltzmann at 194 K.

After only 20 ms, the ion population diminishes by ∼60% and is shifted to lower energy due to rapid depletion of the high-energy tail. At the high pressure limit, background gas is present in sufficient concentration to rapidly exchange energy *via* collisions, so that ions with internal energy above a threshold dissociation are capable of quickly transferring energy instead of water evaporation. Under zero-pressure limit conditions, energy transfer is accomplished only through radiative energy processes *via* absorption or emission of a blackbody photon. For ions with mass ≥ 1.6 kDa, these radiative processes occur quickly enough to match the unimolecular kinetics, k_{uni}, observed at the high pressure limit ($k_{-1,rad} \gg k_d$).[16] However, smaller ions undergo dissociation, *e.g.* water molecule evaporation, at a rate much more quickly than radiative energy loss and as a result, ions with internal energies above

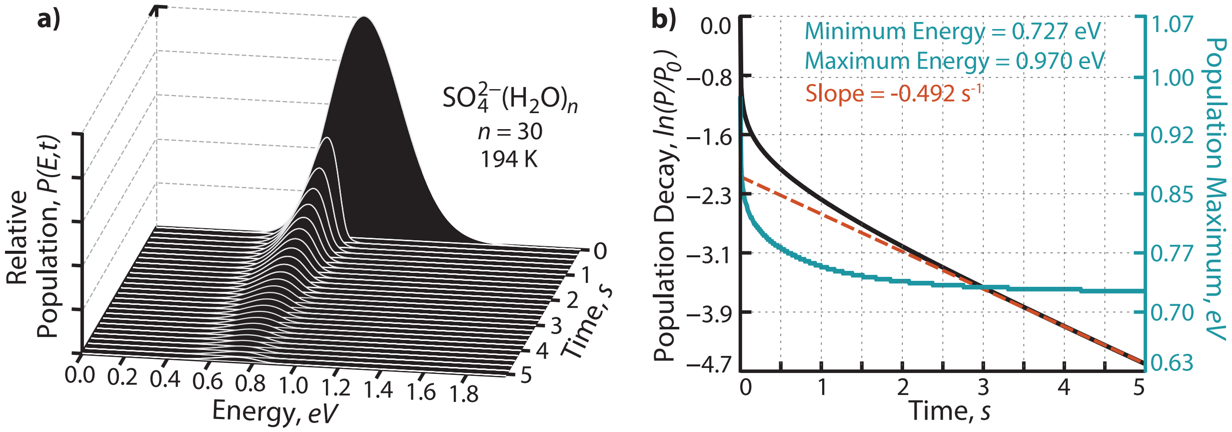

Figure 5.3: Master equation modeling output for $n_e = 30$ using parameters $\mu = 0.5$, $\log(A) = 17$, $E_0 = 0.43$ eV. (a) Relative populations with respect to energy over 5 s of reacting with blackbody photons and (b) quantitative plot of population decay (black) and most populated energy (blue) as a function of time.

the required threshold dissociation undergo rapid depletion without a sufficient means to exchange energy with the rest of the distribution ($k_{-1,rad} \ll k_d$). This results in a narrowing and decrease in average internal energy of the ion population observed in Figure 5.3a.

A quantitative plot for the population decay and maximum energy shift of the $n_e = 30$ ion distribution is presented as a function of reaction time (Figure 5.3b). The unimolecular kinetics for water molecule loss can be extracted from the slope of $ln(P/P_0)$ at a given time. Within the first 20 ms, $k_{uni} = 92.7$ s^{-1} due to the rapid depletion of the high-energy tail. This rate decreases with time until ∼3.0 s, where a steady state with $k_{uni} = 0.492$ s^{-1} is reached. At this time, the ion distribution has equilibrated with the blackbody photons at 194 K. Experimentally, the ions are not detected until ∼6 s after thermalization with nitrogen gas. Therefore, the experimentally measured ion distributions have reached a steady state and can be fitted by finding modeling parameters that result in steady state kinetics matching the k_{BIRD} values from experiment. Furthermore, the maximum energy of the distribution shifts between the initial and steady state populations ($\Delta E \simeq 0.24$ eV). This results in a population of ions that are much cooler than the thermalized distribution at $t = 0$.

The modeling parameters that affect k_{uni} include the high-pressure limit pre-exponential factor, A^∞, a transition dipole scaling factor, μ, and the threshold dissociation energy, E_0. Values of A^∞ between $10^{15} - 10^{18}$ s^{-1} correspond to entropically favored dissociations and can be used to adequately represent water molecule evaporation from a hydrated cluster.[23,29] To model radiative blackbody absorption and emission processes, harmonic frequencies were calculated using density functional theory (DFT) methods. The calculated intensities can be adjusted with a scaling factor, μ, to more accurately model the experimental radiative rates. Using a range of values for the master equation modeling parameters A^∞, μ, and

E_0, the criteria for a successful fit to the experimental temperature dependence requires the Arrhenius slope of modeled data to be within the standard error for the experimental slope, and the calculated k_{uni} rate constants must be within a factor of two of the experimental rate constants, k_{BIRD}. To fit the experimental data, values of A^∞ and μ were fixed while a range of E_0 were used to find values of k_{uni} that satisfied these fitting criteria.

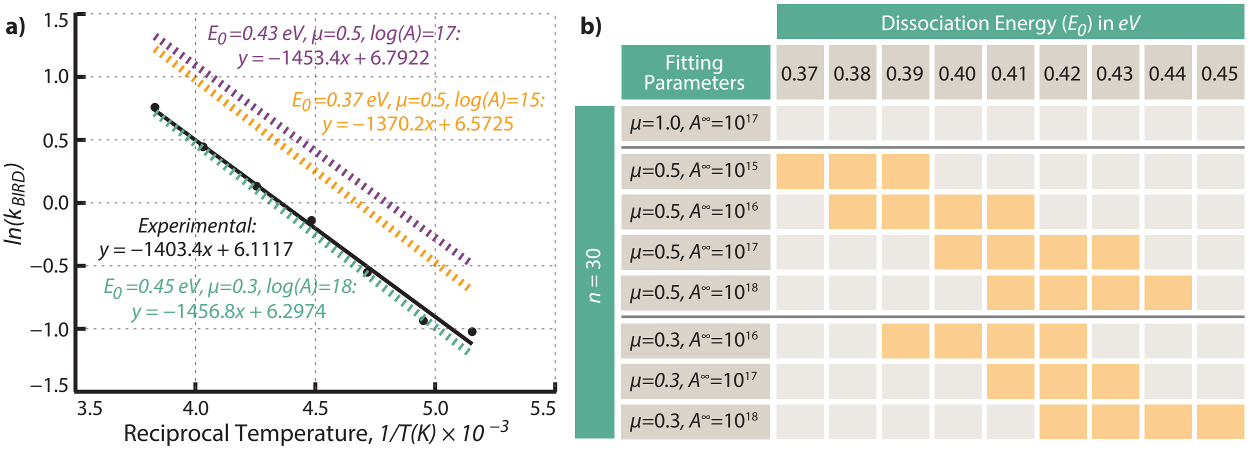

Fitting Parameters	0.37	0.38	0.39	0.40	0.41	0.42	0.43	0.44	0.45
μ=1.0, A^∞=10^{17}									
μ=0.5, A^∞=10^{15}	🟧	🟧	🟧						
μ=0.5, A^∞=10^{16}		🟧	🟧	🟧	🟧				
μ=0.5, A^∞=10^{17}				🟧	🟧	🟧	🟧		
μ=0.5, A^∞=10^{18}					🟧	🟧	🟧	🟧	
μ=0.3, A^∞=10^{16}			🟧	🟧	🟧	🟧			
μ=0.3, A^∞=10^{17}					🟧	🟧	🟧		
μ=0.3, A^∞=10^{18}						🟧	🟧	🟧	🟧

Dissociation Energy (E_0) in eV

Figure 5.4: Master equation modeling fits for $n_e = 30$ to (a) experimental Arrhenius plot with a range of fits producing the largest and smallest values of E_0 and (b) the full range of E_0 values obtained using a range of fitting parameters.

Examples of master equation modeled Arrhenius fits to the temperature dependence of $n_e = 30$ are shown in Figure 5.4a. Although the closest fit to experimental data is found using $\mu = 0.3$, those using $\mu = 0.5$ are within a factor of two with respect to experimental k_{BIRD} values. To the contrary, there are no values of A^∞ and E_0 that lead to a successful fit with unscaled $\mu = 1.0$, which suggests that DFT-calculated intensities for aqueous droplets are larger than physically measured values. The range of E_0 values that fit each set of fixed A^∞ and μ are provided in Figure 5.4b. The calculated E_0 for $n_e = 30$ is 0.41 ± 0.04 eV, with lowest values ($E_0 = 0.38 \pm 0.01$ eV) from $A^\infty = 10^{15}$ s^{-1} and $\mu = 0.5$, highest values ($E_0 = 0.435 \pm 0.015$ eV) with $A^\infty = 10^{18}$ s^{-1} and $\mu = 0.3$, and intermediate values ($E_0 = 0.415 \pm 0.015$ eV) using $A^\infty = 10^{17}$ s^{-1} and $\mu = 0.5$. The full range of E_0 derived from master equation modeling for $n_e = 35, 40$ and 45 are provided in Figure 5.5. Values of E_0 for $n_e = 35$ (0.48 ± 0.04 eV) and $n_e = 35$ (0.485 ± 0.045 eV) are comparable, while those for $n_e = 30$ and $n_e = 45$ (0.42 ± 0.06 eV) are also similar. This is likely due to the presence of MNCs in $n_e = 35$ and 40 that lead to enhanced stability and therefore larger values of E_0.

The calculated values of E_0 are comparable to experimental values measured using ultraviolet photodissociation (UVPD) of solvated dications.[4] For hydrated $M(H_2O)_n$ with M = Cu^{2+}, Co^{2+}, and Fe^{2+} and $n = 30$, the experimentally measured E_0 ranges from $0.44 - 0.46$ eV, while the same ions at $n = 40$ have $E_0 = 0.43 - 0.44$ eV. These cluster sizes are not MNCs for the divalent ions and therefore the measured E_0 values are more directly com-

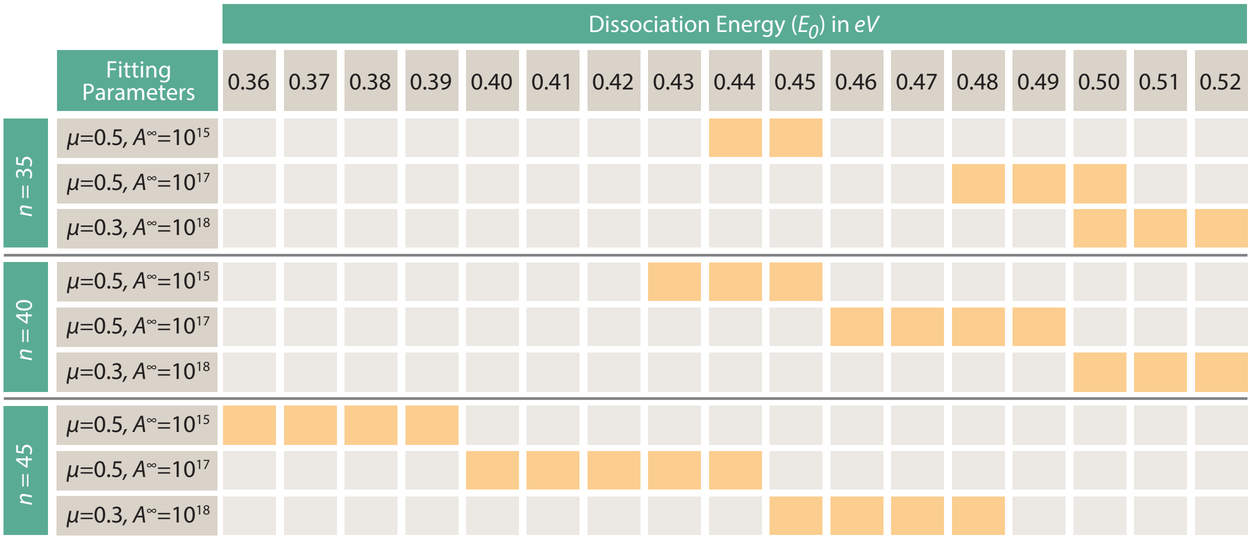

		Dissociation Energy (E_0) in eV																
	Fitting Parameters	0.36	0.37	0.38	0.39	0.40	0.41	0.42	0.43	0.44	0.45	0.46	0.47	0.48	0.49	0.50	0.51	0.52
$n = 35$	μ=0.5, A^∞=10^{15}									🟧	🟧							
	μ=0.5, A^∞=10^{17}													🟧	🟧	🟧		
	μ=0.3, A^∞=10^{18}															🟧	🟧	🟧
$n = 40$	μ=0.5, A^∞=10^{15}								🟧	🟧	🟧							
	μ=0.5, A^∞=10^{17}											🟧	🟧	🟧	🟧			
	μ=0.3, A^∞=10^{18}															🟧	🟧	🟧
$n = 45$	μ=0.5, A^∞=10^{15}	🟧	🟧	🟧	🟧													
	μ=0.5, A^∞=10^{17}					🟧	🟧	🟧	🟧	🟧								
	μ=0.3, A^∞=10^{18}										🟧	🟧	🟧	🟧				

Figure 5.5: Full range of E_0 values for a range of fitting parameters from master equation modeling of $n_e = 35$, 40, and 45.

parable to $SO_4^{2-}(H_2O)_n$ with $n_e = 30$ and 45. The measured E_0 values for dications are consistent with the upper limit of those calculated for dianions. This may be attributed to structural differences at the droplet surface, *i.e.*, the surface of cationic clusters have several dangling or "free" O–H water molecules, whereas anionic droplets of $SO_4^{2-}(H_2O)_n$ between $n = 30 - 45$ are primarily composed of inward-facing hydrogen-bonded water molecules.[25] Therefore, these structural differences may account for the lower E_0 due to a less optimal orientation of water molecules and hydrogen bonding motifs at the surface.

5.3.3 Calculating Effective Temperatures.

The effective temperatures of hydrated ions measured at the zero pressure limit are lower than the ion cell temperature due to the rapid depletion of the high-energy tail in the ion distribution. The actual ion population probed has a lower energy than the initial distribution, as shown in Figure 5.3 for $n_e = 30$ ($\Delta E \simeq 0.24$ eV). There are two potential methods for extracting an effective temperature from the change in relative population with time. First, the *Boltzmann maximum* method uses the maximum energy in the ion population during the steady state. This same maximum energy is reproduced with a Boltzmann distribution by varying the initial ion temperature. As an example, the ion distribution for $n_e = 30$ at 194 K using the parameters $A^\infty = 10^{17}$ s^{-1}, $\mu = 0.5$, and $E_0 = 0.43$ eV has a maximum at 0.73 eV at the steady state. This maximum corresponds to a Boltzmann distribution of ~165 K ($\Delta T = 29$ K).

Alternatively, the *initial kinetics* method uses the unimolecular steady state kinetics to find the temperature of a Boltzmann distribution that depletes at the same rate within the first 10 ms. For instance, $n_e = 30$ at 194 K using the parameters $A^{\infty} = 10^{17}$ s^{-1}, $\mu = 0.5$, and $E_0 = 0.43$ eV corresponds to the dissociation rate of a Boltzmann distribution at ~145 K ($\Delta T = 49$ K). Unlike the Boltzmann maximum method, using the steady state kinetics requires the dissociation rates for Bolzmann distributions at various temperatures to be calculated for each set of parameters. On average, the initial kinetics result in effective temperature values that are ~20 K cooler with respect to the Boltzmann maximum method. This is due to the fast initial depletion of the high-energy tail, which must be moved to significantly lower energies to be within the same region as the steady state distribution, *i.e.*, kinetic rates for the Boltzmann distributions found using the maxima method are faster than the rates from their associated steady state distributions.

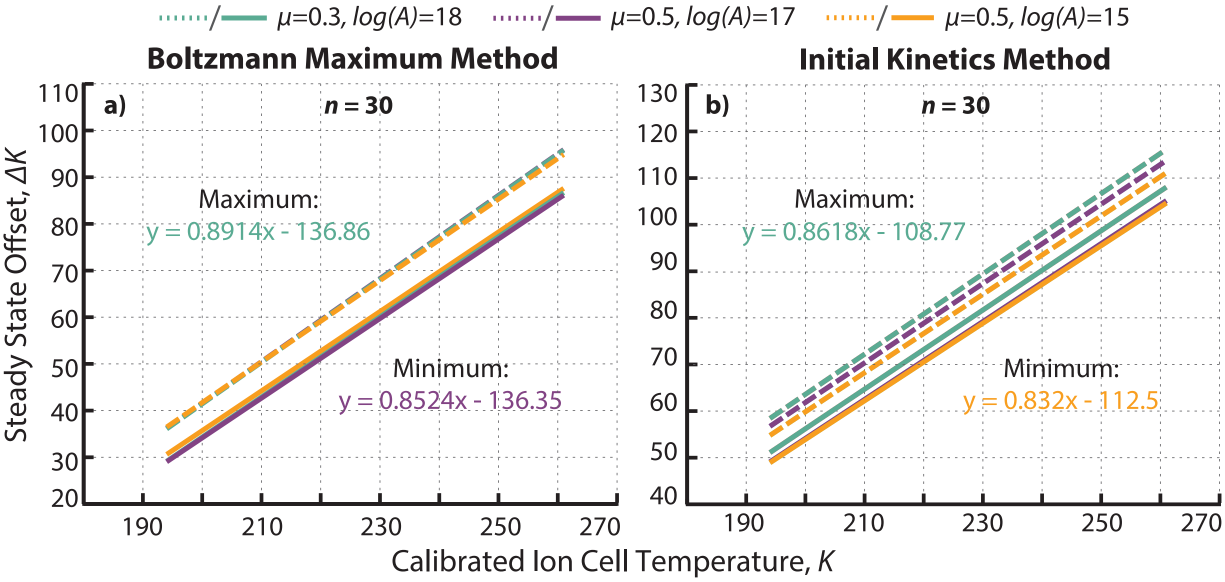

Figure 5.6: Effective temperature offsets for $n_e = 30$ as a function of ion cell temperature based on steady state distributions using (a) the Boltzmann maximum and (b) initial kinetics methods.

A summary for the offset between the effective temperature at the steady state and the thermalized temperature of the ion cell for $n_e = 30$ using three different sets of master equation modeling parameters is shown in Figure 5.6. For each set of parameters, the full range of E_0 values that meet the fitting criteria (Figures 5.4b & 5.5) are used to determine the uncertainty for calculating effective temperatures. For temperature offsets calculated using both the Boltzmann maximum method (Figure 5.6a) and the initial kinetics method (Figure 5.6b), the difference between the calculated effective temperature is ~10 K for the largest and smallest values of E_0. Higher E_0 values lead to effective temperatures that are slightly greater because the larger threshold for dissociation leads to a decrease in the depletion of the high energy tail. As an example, with an ion cell thermalized to 220 K, a $n_e = 30$ ion distribution will be ~59 K cooler once the steady state has been reached, with an effective ion temperature of 161 K using the Boltzmann maximum values.

Effective temperature offset plots for $n_e = 35, 40$, and 45 are provided in Figures A.8–A.10. The effective temperature offsets for n_e = 35 and 40 are less for a given ion cell temperature with respect to n_e = 30 and 45 due to the increased stability to dissociation imparted by the MNCs. For example, with a thermalized ion cell at 220 K, the effective temperature offsets for n_e = 35 and 40 are ΔT = 40 and 48 K, respectively, and for n_e = 30 and 45 are ΔT = 59 and 67 K, respectively (using $\mu = 0.5$, $A^{\infty} = 10^{17}$, and the largest E_0). Between n_e = 30 and 45 (no MNCs), a larger offset ($\Delta\Delta T$ = 8 K) occurs for n_e = 45 and similarly between the two MNC-containing precursors, n_e = 40 has a larger offset than n_e = 35 ($\Delta\Delta T$ = 8 K). This is potentially due to the larger radiative cross section for photon absorption from the larger droplets due to the increased vibrational degrees of freedom.

Previous infrared photodissociation experiments have revealed that long distance ion-water interactions between $SO_4^{2-}(H_2O)_n$ with n_e = 30 and the surface of the droplet persist until the ion cell temperature reaches 340 K.[25] By extrapolating the linear trend in Figure 5.6, this results in an effective ion temperature of ∼180 ± 6 K (ΔT = 160 K) or ∼162 ± 7 K (ΔT = 178 K) using the Boltzmann maximum and initial kinetics methods, respectively. These temperatures are close to that of the Earth's mesosphere and therefore, long distance *structural* interactions may be relevant to the nucleation and propagation of atmospheric aerosols. These large offsets in effective temperature illustrate the necessity of modeling the population for non-covalently bound species measured at low pressures, which will have internal energies much lower than the surrounding instrumental temperatures. In order to study gas phase droplets at elevated temperatures, the change in ion population as a function of time must be properly considered in order to probe hydrated ions of known energy distributions before reaching the lower temperature steady state population.

5.4 Summary and Conclusions

Extensive master equation modeling was used to fit experimental blackbody dissociation kinetics for aqueous $SO_4^{2-}(H_2O)_n$ nanodrops with $n_e = 30 - 45$ and ion cell temperatures between $186 - 360$ K. The modeled microcanonical unimolecular rate constants, k_{uni}, allow for thermal precursor distributions to be plotted as a function of time between isolation and detection of aqueous ion-containing droplets by mass spectrometry. Due to the low-pressure conditions used for storage in an ion cell and the radiative absorption cross sections of droplets in the size range measured, collisions with background gas are negligible and the radiative emission rates are not competitive with energy loss *via* water molecule evaporation. Therefore, rapid depletion of the high energy populations leads to steady state distributions with average internal energies that are lower than the initial thermalized distribution. We find that calculated water molecule binding energies are consistent with those measured by photoexcitation,[4] and that the threshold for water molecule evaporation increases by ∼0.06 eV in precursors with anomalous stabilities. Despite large temperature offsets, with respect to the set ion cell temperature, as large as ΔT = 178 K at 340 K, we find that ion-water interactions between solvated SO_4^{2-} and the droplet surface can extend into a second solvation shell at temperatures relevant to Earth's upper atmosphere.

In order to more accurately compare aqueous ion-containing nanodrops in the size regime between $n = 30 - 45$ to bulk solutions at room temperature, experiments must be designed such that detection times occur before thermal distributions reach a steady state with the surrounding blackbody field. As the size of the droplets increases, the microcanonical rate for water evaporation, k_d, will slowly decrease up to $n \simeq 500$, where the threshold for water evaporation reaches a constant value.[4] This decreased rate of water loss will be accompanied by increasing radiative cross sections for absorption and rates for emission, which continue to increase as a function of internal degrees of freedom and can assist in energy transfer throughout the distribution. Therefore, we expect steady state distributions will experience less evaporative cooling in increasingly larger nanodrops. The results from modeling for aqueous ion-containing droplets presented here can be directly extended to other storage traps operating at the zero-pressure limit and can be adapted to increased pressures by including rates of energy transfer *via* neutral collisions with background gas. Future experiments will explore larger droplet sizes as well as evaporative cooling in cation-containing clusters. A simple relation of effective temperature offsets to zero-pressure Arrhenius values for aqueous droplets is currently in preparation and removes the necessity of extensive modeling to approximate droplet temperatures in the gas phase.

5.5 References

[1] Thaunay, F.; Hassan, A. A.; Cooper, R. J.; Williams, E. R.; Clavaguéra, C.; Ohanessian, G. *Int. J. Mass. Spectrom.* **2017**, *418*, 15–23.

[2] Cooper, R. J.; DiTucci, M. J.; Chang, T. M.; Williams, E. R. *J. Am. Chem. Soc.* **2016**, *138*, 96–99.

[3] Nam, S. H.; Park, H. S.; Lee, M. A.; Cheong, N. R.; Song, J. K.; Park, S. M. *J. Chem. Phys.* **2007**, *126*, 224302.

[4] Heiles, S.; Cooper, R. J.; DiTucci, M. J.; Williams, E. R. *Chem. Sci.* **2017**, *8*, 2973–2982.

[5] Donald, W. A.; Williams, E. R. *Pure Appl. Chem.* **2011**, *83*, 2115–2212.

[6] Donald, W. A.; Leib, R. D.; Demireva, M.; O'Brien, J. T.; Prell, J. S.; Williams, E. R. *J. Am. Chem. Soc.* **2009**, *131*, 13328–13337.

[7] O'Brien, J. T.; Prell, J. S.; Bush, M. F.; Williams, E. R. *J. Am. Chem. Soc.* **2010**, *132*, 8248–8249.

[8] DiTucci, M. J.; Heiles, S.; Williams, E. R. *J. Am. Chem. Soc.* **2015**, *137*, 1650 – 1657.

[9] DiTucci, M. J.; Williams, E. R. *Chem. Sci.* **2017**, *8*, 1391–1399.

[10] Cooper, R. J.; O'Brien, J. T.; Chang, T. M.; Williams, E. R. *Chem. Sci.* **2017**, *8*, 5201–5213.

[11] Shen, V., Y. R. ad Ostroverkhov *Chem. Rev.* **2006**, *106*, 1140–1154.

[12] Stirnemann, G.; Wernersson, E.; Jungwirth, P.; Laage, D. *J. Am. Chem. Soc.* **2013**, *135*, 11824–11831.

[13] Omta, A. W.; Kropman, M. F.; Woutersen, S.; Bakker, H. J. *Science* **2003**, *301*, 347–349.

[14] Klots, C. E. *J. Chem. Phys.* **1985**, *83*, 5854–5860.

[15] Dunbar, R. C. *Mass Spectrom. Rev.* **2004**, *23*, 127 – 158.

[16] Price, W. D.; Williams, E. R. *J. Phys. Chem. A* **1997**, *101*, 8844–8852.

[17] Drahos, L.; Vékey, K. *J. Mass Spectrom.* **1999**, *34*, 79–84.

[18] Dunbar, R. C. *J. Phys. Chem.* **1994**, *98*, 8705–8712.

[19] Price, W. D.; Schnier, P. D.; Williams, E. R. *J. Phys. Chem. B* **1997**, *101*, 664–673.

[20] Jockush, R. A.; Williams, E. R. *J. Phys. Chem. A* **1998**, *102*, 4543–4550.

[21] Strittmatter, E. F.; Schnier, P. D.; Klassen, J. S.; Williams, E. R. *J. Am. Soc. Mass Spectrom.* **1999**, *10*, 1095–1104.

[22] Schnier, P. D.; Price, W. D.; Strittmatter, E. F.; Williams, E. R. *J. Am. Soc. Mass Spectrom.* **1997**, *8*, 771–780.

[23] Wong, R. L.; Paech, K.; Williams, E. R. *Int. J. Mass. Spectrom.* **2004**, *232*, 59–66.

[24] Dunbar, R. C.; McMahon, T. B.; Thölmann, D.; Tonner, D. S.; Salahub, D. R.; Wei, D. *J. Am. Chem. Soc.* **1995**, *117*, 12819–12825.

[25] DiTucci, M. J.; Stachl, C. N.; Williams, E. R. *Manuscript in Progress* **2017**,

[26] Bush, M. F.; O'Brien, J. T.; Prell, J. S.; Saykally, R. J.; Williams, E. R. *J. Am. Chem. Soc.* **2007**, *129*, 1612–1622.

[27] Prell, J. S.; O'Brien, J. T.; Williams, E. R. *J. Am. Soc. Mass Spectrom.* **2010**, *21*, 800–809.

[28] Shao, Y.; Molnar, L. F.; Jung, Y.; Kussmann, J.; Ochsenfeld, C.; Brown, S. T.; Gilbert, A. T. B.; Slipchenko, L. V.; et al., *Phys. Chem. Chem. Phys.* **2006**, *8*, 3172–3191.

[29] Gilbert, R. C.; Smith, S. C. *Theory of Unimolecular and Recombination Reactions*; Blackwell Scientific Publications: London, 1990.

Chapter 6

Effects of Multivalent Hexacyanoferrates and Their Ion Pairs on Water Molecule Dynamics Measured with Terahertz Spectroscopy

This chapter is reproduced with permission from:

Matthew J. DiTucci, Fabian Böhm, Gerhard Schwaab,
Evan R. Williams, and Martina Havenith

"Effects of Multivalent Hexacyanoferrates and Their Ion Pairs on Water
Molecule Dynamics Measured with Terahertz Spectroscopy",
Phys. Chem. Chem. Phys. **2017**, *19*, 7297–7306.

6.1 Introduction

Ion-water and ion-ion interactions along with the resulting dynamics of their hydration shells can influence many chemical and physical properties of aqueous solutions.[1,2] For example, ordering within the Hofmeister series, which details the propensity for salts to denature proteins, has been related to an ion's ability to pattern the hydrogen-bonding network of water molecules.[3–5] A perturbation of optimal hydrogen-bonding structure as a result of ion interaction often results in freezing point depression,[6] a phenomenon commonly exploited as highway salting in frigid weather. The formation of aerosols,[7] enzymatic functionality,[8] and effectiveness of toxic metal removal are all based on ion-water interactions that occur at the molecular level.[9] The origin of these properties can be further complicated by the presence of ion pairs.[10] As a result, our understanding of such processes is reliant on our ability to measure these fundamental intermolecular properties.

A variety of techniques have been utilized in order to probe ion-water interactions in aqueous solutions. Diffraction methods, such as x-ray and neutron scattering, map the radial density of water molecules surrounding an ion. Such studies are successful in characterizing the inner hydration shell, although measuring interactions well beyond coordinated water molecules is challenging due to a decrease in structure for subsequent shells.[11–14] Soper et al. have demonstrated water O–O distances beyond the inner hydration shell shift with respect to bulk water in NaCl and KCl solutions due to solvent electrostriction, which provides evidence for extended perturbation.[15] Extended interactions have also been measured using nuclear magnetic resonance (NMR),[16–18] vibrational,[19–21] and dielectric relaxation (DRS) spectroscopies.[22–24] For example, recent experiments by Buchner et al. suggest that the phosphate trianion, PO_4^{3-}, slows rotational dynamics of ∼39 water molecules, which constitutes a well-defined second solvation shell.[23] The dynamic motions examined with these spectroscopic methods are on the order of femtoseconds for vibrational and sub-nano to microseconds for NMR and DRS. The concerted dynamical motions of water molecules around an aqueous solute occur on the picosecond timescale.[25,26] Therefore, experiments must be capable of monitoring changes within this frequency in order to probe the variance of collective motions as a result of ion-water interactions. Recent advancements in measuring and interpreting terahertz (THz) spectra have provided new insights into ion-water interactions.[27–29] This region of the electromagnetic spectrum includes collective hydrogen bond rearrangements and concerted librational motions. Accordingly, this technique is well-suited for directly probing ion-induced dynamical changes to the hydrogen-bonding network.

Many condensed-phase species have been investigated in the THz region. Though primarily local ion-water interactions have been proposed for measurements in monatomic mono- to trivalent cations,[28,30–33] extended dynamic solvation shells have been measured for both amino acids and proteins.[34,35] For instance, the THz absorption of hydrophilic and hydrophobic amino acids, which was found to correlate with residue polarity, reveals an increase in hydrogen-bonding lifetimes up to 5 Å from the solute relative to bulk water.[34] Temperature-dependent studies with the antifreeze glycoprotein indicate an extended gradient of slowed dynamics up to $\sim 20 - 35$ Å from the solute, which potentially enables freezing-point depression in arctic-dwelling organisms.[35] No long-distance influence was reported for La^{3+} using THz spectroscopy,[32] although evidence for interactions beyond inner solvation around Fe^{3+} has been reported.[31] This discrepancy may in part be due to a difference in the propensity for forming various types of ion-pairs, i.e., solvent-shared, solvent-separated, or contact pairs,[10] which may shield the ionic charge. This leads to interest in further understanding how electrostatic influences from both singular and paired ions can affect hydrogen-bonding dynamics. However, solution-phase experiments often require high ion concentrations in order to observe signal, making it challenging to observe the effects of individual ions on water structure and dynamics at extended ranges due to overlapping solvation shells.

Gas-phase aqueous nanodrops formed by electrospray ionization (ESI) can be used to study ion-water interactions to a theoretical infinite dilution. Long-distance ion-induced structural orientations have been observed previously using infrared photodissociation (IRPD) spectroscopy.[5,6,36–38] A recent investigation of $La^{3+}(H_2O)_n$ with n up to 550 shows a delayed onset of crystallinity, i.e., freezing point depression, by ∼100 water molecules with respect to neutral nanodrops, illustrating remote ion-water interactions can extend well beyond the inner hydration shell.[6] An extended structural orientation of water molecules at the nanodrop surface has also been observed for several anions.[36–38] For instance, the absence of spectral intensity at ~3700 cm^{-1} for $SO_4^{2-}(H_2O)_n$ clusters with $n < 47$ is a result of surface water molecules orienting inward toward the solvated anion due to the interaction with the Coulombic potential.[36] For droplets of size $n \geq 47$, a new spectral peak emerges that is indicative of water molecules that are free to orient so that the O–H bond faces outward from the droplet. This marks an effective distance for the extent of ion-water interactions leading to structural effects. Recent nanodrop experiments with hexacyanoferrates revealed that structural effects can extend to nanometer distance from the ion,[37,38] but these experiments do not provide information on the perturbation of collective water molecule dynamics. Although previous condensed-phase studies have shown hexacyanoferrates perturb the inner solvation shell,[39–41] these measurements do not probe extended solvation shells and thus provide no information regarding long-range ion-induced dynamical changes. Therefore, the tri- and tetraanionic hexacyanoferrate complexes are ideal candidates for investigating how electrostatic interactions can influence water molecule dynamics within the THz region.

Hexacyanoferrates are widespread in industrial, analytical, and biological applications. They are commonly used for monitoring intracellular redox activity in living cells upon introduction of chemical stimuli and can be used to fine-tune the magnetic properties of polycrystalline materials.[42,43] $Fe(CN)_6^{3-}$ is used as a strong oxidant in chemical synthesis and $Fe(CN)_6^{4-}$ has been utilized for several processes, including citric acid production, refining wine, and tin electroplating as a result of its ability to form several insoluble heavy metal complexes.[44,45] Hexacyanoferrates are principal components in the pigment Prussian blue, $Fe_4[Fe(CN)_6]_3$, which is a constituent of zeolitic ion sieves,[46] an active ingredient for treatment of internal Cs+ and Tl+ poisoning[47] and has been considered for both energy storage and removal of radioactive Cs+ in global waters.[48,49] Results from potentiometric and spectroscopic measurements suggest that hexacyanoferrate ion-pairing contributes significantly even in dilute solutions with milimolar concentrations.[50–53] Therefore, understanding the ion-water and ion-ion interactions for these species is not only of fundamental interest, but could also guide future applications and improve currently existing techniques.

Here, the low-frequency terahertz spectra of potassium and sodium hexacyanoferrate salts are measured as a function of concentration. Subtle nonlinearities in the molar extinction spectra provide evidence for extensive ion-pairing between the cations and hexacyanoferrates, which are found to perturb the dynamics of bulk water molecules beyond the first solvation shell. The implementation of spectral subtraction and harmonic fitting uncovers unique spectral features ranging from cation hydration rattling dynamics to a cross-correlated anion-water mode. This is the first report of terahertz spectroscopy measurements of highly charged tri- and tetraanionic transition metal complexes and these data provide new insights into long-distance ion-water interactions and dynamics.

6.2 Experimental Methods

6.2.1 Materials

Aqueous solutions of $K_3Fe(CN)_6$, $K_4Fe(CN)_6{\cdot}3H_2O$ (Sigma–Aldrich Chemie GmbH, Germany) and $Na_4Fe(CN)_6{\cdot}10H_2O$ (Alfa Aesar GmbH & Co KG, Germany) with concentrations between $0.2 - 1.0$ M or up to their solubility limits (488 g/L @ 20 °C, 360 g/L @ 25 °C and 200 g/L @ 25 °C, respectively)[54] were prepared using HPLC grade ultra pure water (Thermo Electron LED GmbH, Niederelbert, Germany). Density measurements for each of the hexacyanoferrate solutions were performed using an Anton Paar DMA-58 density meter that was temperature-regulated to 20 ± 0.2 °C and were used in order to determine the concentration of water. The abundance of hydronium and hydroxide ions at these concentrations was obtained from pH measurements. The pH does not vary widely across the range of concentrations for $K_3Fe(CN)_6$ and $K_4Fe(CN)_6{\cdot}3H_2O$, and the average pH is 7.7 ± 0.2 and 9.4 ± 0.2 for the respective solutions. For all solutions, the hydroxide concentration is less than 100 µM for both hexacyanoferrate salts.

6.2.2 THz Fourier Transform Measurements

Broadband terahertz spectra were recorded between $30 - 500$ cm^{-1} using a Bruker Vertex 80V FTIR spectrometer equipped with a helium-cooled silicon bolometer (Infrared Laboratories, Tucson, AZ) for detection. For each spectrum, 128 scans were averaged using a 2 cm^{-1} resolution. Further details regarding the experimental setup are provided in Schmidt et al.[30] Samples were loaded into a custom Invar liquid cell based on the Bruker design with CVD polycrystalline diamond windows (Diamond Materials GmbH, Breisgan, Germany) of ∼500 ± 100 µM thickness, which were chosen due to the optimal transmittance over the desired frequency range. The thickness of the liquid sample is controlled with a ∼25 µm Kapton spacer. The exact thickness of the liquid sample can be determined via the Fabry-Pérot etalon effect by measuring the interference pattern of mid-infrared radiation passing through the empty cell prior to measurements. The sample thickness is expressed as $d = \mathit{\Delta} N/(2n_{air}\mathit{\Delta}\widetilde{\nu})$, where n_{air} is the refractive index of air and $\mathit{\Delta} N$ is the number of oscillations in the measured interferogram between the signal maxima for frequencies $\widetilde{\nu}_1$ and $\widetilde{\nu}_2$, for which $\mathit{\Delta}\widetilde{\nu} = (\widetilde{\nu}_2 - \widetilde{\nu}_1)$.

Prior to each sample measurement, a spectrum of pure water is recorded in order to yield the transmission intensity of water, $I_{H_2O}(\widetilde{\nu})$, which is used as a reference to remove effects of reflections within the cell. Using the Beer–Lambert law, the frequency-dependent absorption coefficient for each solution, $\alpha_{solution}(\widetilde{\nu})$, is obtained from Equation (6.1):

$$\alpha_{solution}(\widetilde{\nu}) = -\frac{1}{d}\, ln\left(\frac{I_{solution}(\widetilde{\nu})}{I_{H_2O}(\widetilde{\nu})}\right) + \alpha_{H_2O,f}(\widetilde{\nu}) \pm x \cdot \alpha_{vapor}(\widetilde{\nu}) \qquad \text{(Equation 6.1)}$$

where $I_{solution}(\widetilde{\nu})$ is the transmitted intensity of the sample solution. To avoid the reintroduction of artifacts from cell reflections, a functional form of the absorption coefficient for bulk water, $\alpha_{H_2O,f}$, was obtained by fitting temperature-dependent bulk water measurements to etalon-corrected reference spectra at 25 °C published by Bertie and Lan.[28,55] Minor fluctuations in residual water vapor were corrected by measuring a spectrum in the absence of nitrogen purging to obtain the absorption coefficient, $\alpha_{vapor}(\widetilde{\nu})$, which was scaled by x to remove contributions from vapor at ∼150.4 and 202.5 cm^{-1} (Figure A.11).

The absorption coefficient for bulk water is scaled using the concentration of water obtained from density measurements, $c_{H_2O,solution}$, and is removed from $\alpha_{solution}(\widetilde{\nu})$ in order to yield the effective ion absorption coefficient, $\alpha_{ion}^{eff}(\widetilde{\nu})$, which contains all spectral contributions from the ions and their influence on surrounding water molecules:

$$\alpha_{ion}^{eff}(\widetilde{\nu}) = \alpha_{solution}(\widetilde{\nu}) - \left(\frac{c_{H_2O,solution}}{55.409 \text{ mol L}^{-1}}\right) \cdot \alpha_{H_2O,f}(\widetilde{\nu}) \qquad \text{(Equation 6.2)}$$

Because typical water molecule frequencies and/or intensities may be shifted due to a perturbed hydrogen-bonding network in the vicinity of ions, the removal of scaled $\alpha_{H_2O,f}$ results in partial overcompensation, which manifests as a negative contribution with the lineshape of the bulk water spectrum. However, this subtraction preserves positive contributions due to intrinsic or coupled intermolecular stretching and intramolecular rattling and/or vibrations from supramolecular solvated complexes.[30,56] Therefore, the lineshape of $\alpha_{ion}^{eff}(\widetilde{\nu})$ can be described as a linear superposition of both negative overcompensation of bulk water as well as the positive inter- and extended intramolecular contributions from solvated ions.

6.3 Results and Discussion

6.3.1 Hexacyanoferrate Salt Spectra

The ionic absorption coefficients, $\alpha_{ion}^{eff}(\widetilde{\nu})$, for solutions containing $K_3Fe(CN)_6$, $K_4Fe(CN)_6$ and $Na_4Fe(CN)_6$ with a range of concentrations show positive intensity in the spectral region between $30 - 500$ cm^{-1} (Figure 6.1). Although no region of $\alpha_{ion}^{eff}(\widetilde{\nu})$ falls below zero, these spectra contain a scaled negative contribution from bulk water. Therefore, the observed intensity is due to both direct ionic contributions and also frequency-shifted intensity from the altered dynamic behavior of water molecules in this region. All three salts have similar lineshapes consisting of two low-frequency modes and a high-frequency shoulder overlapping a narrow, high-intensity band.

Both potassium salts have a peak near ∼60 cm^{-1}, whereas the lowest-energy peak for the sodium salt is blue-shifted to ∼90 cm^{-1}. Intensity in this region has previously been attributed to ionic rattling modes, i.e., the dynamic sub-picosecond motion of an ion within its inner hydration shell.[30] The frequency of this mode red shifts with increasing ion mass and broadens with ionic diameter. The mass of K^+ is larger than that of Na^+ and the first shell ion-water distance, which approximates the ionic size within the hydrogen-bonding network, is larger for K^+ (2.65 Å) than for Na^+ (2.34 Å).[2] This is consistent with an assignment of K^+

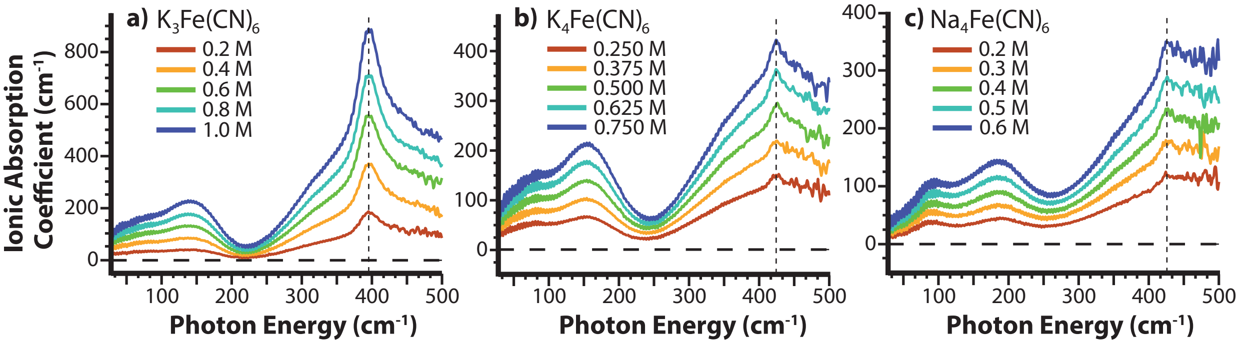

Figure 6.1: Effective ionic absorption coefficients for a range of concentrations between 0.2 – 1.0 M for aqueous solutions of (a) $K_3Fe(CN)_6$, (b) $K_4Fe(CN)_6$ and (c) $Na_4Fe(CN)_6$. The thick dotted horizonal line represents a value of $\alpha_{ion}^{eff}(\widetilde{\nu}) = 0$. A thin dotted vertical line guides the emergence of a narrow band attributed to Fe–C intramolecular stretching, which appears in the high-frequency shoulder and does not shift with concentration.

rattling to the peak near ~60 cm^{-1}, which appears broadened and less defined with respect to the blue-shifted peak at ~90 cm^{-1}, which is assigned to Na^+ rattling.

There is a narrow, high-frequency peak in the spectrum of each salt. This peak is centered at ~395 cm^{-1} for $K_3Fe(CN)_6$ and is blue-shifted to ~425 cm^{-1} for both $K_4Fe(CN)_6$ and $Na_4Fe(CN)_6$. This absorption has been assigned to the hexacyanoferrate Fe–C stretch.[57,58] The center frequency of this peak blue shifts for $Fe(CN)_6^{4-}$ with respect to $Fe(CN)_6^{3-}$ as a result of the higher π-bonding character, which results in a higher Fe–C force constant. The difference in intensities for this absorption between the two ions may be due to a lower transition dipole moment as a result of the difference in the number of *d*-electrons.[58]

The remaining low-frequency peak for solutions of $K_3Fe(CN)_6$ (~140 cm^{-1}), $K_4Fe(CN)_6$ (~155 cm^{-1}) and $Na_4Fe(CN)_6$ (~185 cm^{-1}) is not consistent with either cation identity or anionic charge state. To further investigate the origin of this low-frequency peak, the concentration dependence of $\alpha_{ion}^{eff}(\widetilde{\nu})$ was plotted (Figure 6.2) by calculating the effective ionic molar extinction, $\varepsilon_{ion}^{eff}(\widetilde{\nu})$, for each sample concentration:

$$\varepsilon_{ion}^{eff}(\widetilde{\nu}) = \frac{\alpha_{ion}^{eff}(\widetilde{\nu})}{c_{ion}} \qquad \text{(Equation 6.3)}$$

The expanded regions (Figure 6.2d-f) show that the low-frequency peaks have subtle nonlinear behavior between ~30 – 225 cm^{-1}. The cation rattling peak decreases slightly with concentration whereas the remaining low-frequency peak increases. For an aqueous two-component solution consisting of cations and anions, $\alpha_{ion}^{eff}(\widetilde{\nu})$ is expected to increase linearly with concentration, i.e., no changes in $\varepsilon_{ion}^{eff}(\widetilde{\nu})$. Deviation from linear behavior could be due to either a rearrangement in hydration motifs as a result of the confined hydrogen-bonding network with increasing solute concentration, or the result of a third component that depends nonlinearly on the solution concentration, i.e., ion association. This

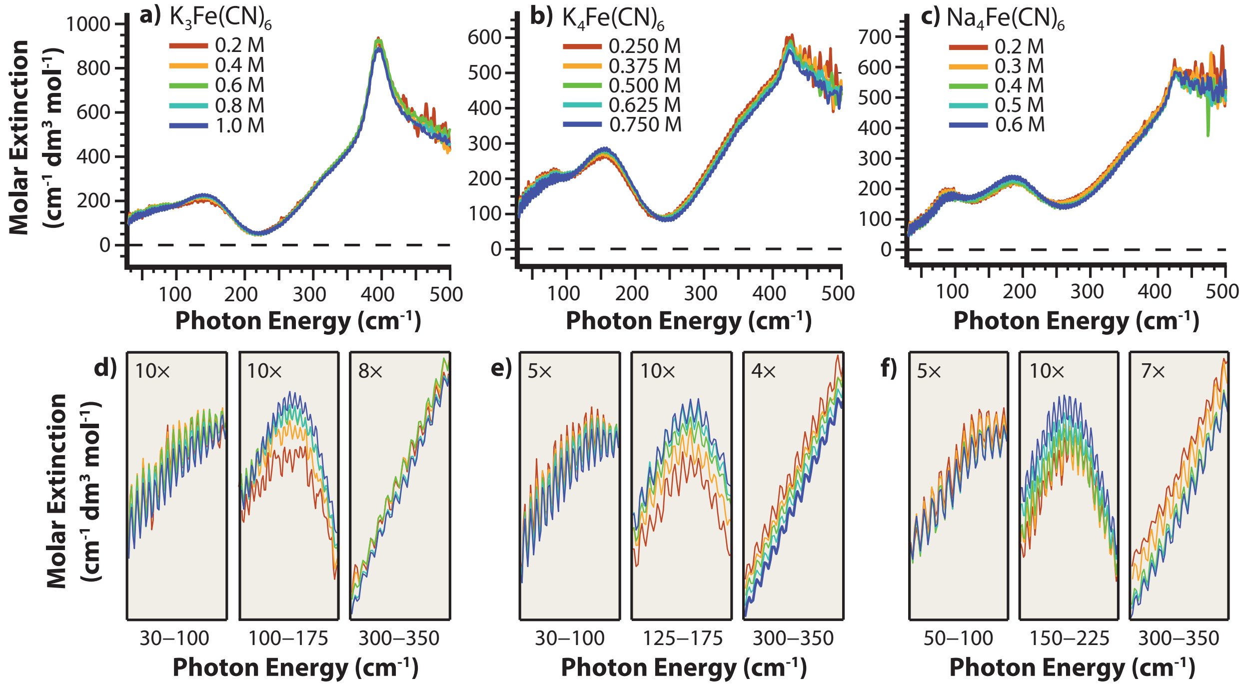

Figure 6.2: Effective ionic molar extinctions for a range of concentrations between 0.2 – 1.0 M for aqueous solutions of (a) $K_3Fe(CN)_6$, (b) $K_4Fe(CN)_6$ and (c) $Na_4Fe(CN)_6$. The expanded regions in (d) – (f) illustrate the nonlinear intensity behavior with increasing concentration. The thick dotted horizonal line represents a value of $\varepsilon_{ion}^{eff}(\widetilde{\nu}) = 0$.

spectral nonlinearity has been assigned to ion-pairing in several other salts, including Ni^{2+}, Mn^{2+}, La^{3+}, and Fe^{3+} halides.[28,31,32] The decrease in the cation rattling peak with increasing concentration is consistent with a smaller number of free K^+/Na^+ ions in solution as a result of pairing. Because the second low-frequency peak shows nonlinear behavior and increases with concentration, this band is assigned to hexacyanoferrate ion-pairing. This assignment is consistent with the strong propensity for hexacyanoferrates to form ion pairs as observed in previous potentiometric and spectroscopic measurements.[50–53] The ion association observed could be attributed to contact, solvent-shared, or solvent-separated pairs.[10] However, the present experiments do not differentiate between various types of association.

Another region for which there is concentration dependence in $\varepsilon_{ion}^{eff}(\widetilde{\nu})$ is the high-frequency shoulder near ~325 cm^{-1} (Figure 6.2a-c). Although this region is nearly linear for $K_3Fe(CN)_6$, the shoulder blue shifts with concentration for the two tetraanionic salts. This region of the bulk water spectrum is associated with the concerted librational motion of water molecules.[30,31] A shift of the librational mode to higher frequencies is consistent with a greater confinement effect experienced by the surrounding water molecules, i.e., hindered librational motions as a result of an increased interaction with solutes. The greater electrostriction expected by tetraanionic salts is likely responsible for the larger concentration-dependent shift of the high-frequency shoulder. This is also consistent with the overall blue shift of the librational shoulder for the tetraanionic salts with respect to $K_3Fe(CN)_6$.

6.3.2 Spectral Dissection

The molar extinction spectra can be further examined by subtracting the contributions from specific counterions. In order to remove the individual contributions from K^+, the $\varepsilon_{ion}^{eff}(\widetilde{\nu})$ spectrum for $K_3Fe(CN)_6$ was appropriately scaled and subtracted from $K_4Fe(CN)_6$ (Figure 6.3). Although the charge state of the anion is different for the two salts, previous results have shown that the counterion identity does not significantly affect the frequency of bands associated with contributions from a single ion.[28,31–33] As a result, the remaining residual spectra will consist only of intensity due to the solvated anion and any ion-pairing interactions, i.e., spectral absorptions that are common to both salts will be removed in the difference spectrum. Because of the order of subtraction, negative contributions are attributed to $K_3Fe(CN)_6$, which will also reduce the positive intensity associated with $K_4Fe(CN)_6$ absorptions.

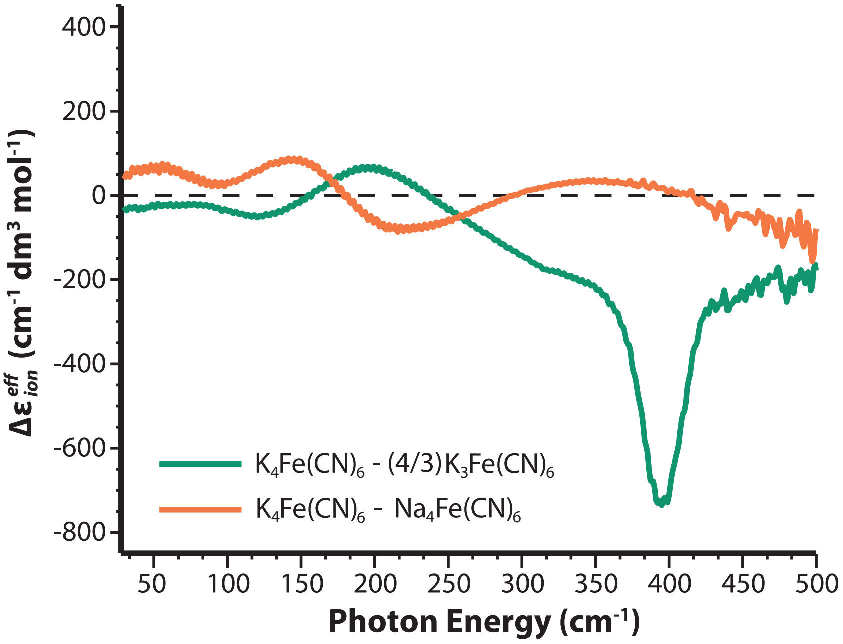

Figure 6.3: Effective ionic molar extinction difference spectra for (green) scaled $K_3Fe(CN)_6$ removed from $K_4Fe(CN)_6$ to remove spectral features from K^+ absorption and (orange) $Na_4Fe(CN)_6$ directly removed from $K_4Fe(CN)_6$ to remove spectral features from $Fe(CN)_6^{4-}$.

There is no peak at ~60 cm^{-1} in the difference spectrum, which supports its assignment to K^+ rattling. Negative and positive features at ~125 cm^{-1} and ~200 cm^{-1}, respectfully, are residuals originating from a blue shift of the second low-frequency peak in $\varepsilon_{ion}^{eff}(\widetilde{\nu})$. The presence of the residuals in this region shows that this peak is not attributable to isolated cation contributions. This shift could arise as a result of greater electrostriction to the water molecules by $\mathrm{Fe(CN)}_6^{4-}$ due to the higher charge state, which can decrease the anion-water distance and alter the water molecule dynamics. This shift could alternatively be attributed to a change in dynamics for water molecules surrounding ion-paired species $\mathrm{KFe(CN)}_6^{2-}$ and $\mathrm{KFe(CN)}_6^{3-}$. The sharp negative peak at $\sim$400 cm^{-1} is likely due to a stronger transition dipole for the metal–ligand stretch of $\mathrm{Fe(CN)}_6^{3-}$ due to the difference in number of *d*-orbital electrons.[58] A final interesting feature is the negative signal originating from the librational shoulder at $\sim$320 cm^{-1}. Negative intensity suggests the librational band is blue shifted in $\mathrm{Fe(CN)}_6^{4-}$ with respect to $\mathrm{Fe(CN)}_6^{3-}$ as expected based on the greater anionic charge state. The Coulombic potential from $\mathrm{Fe(CN)}_6^{4-}$ can influence water molecules to a greater extent than $\mathrm{Fe(CN)}_6^{3-}$ and as a result, the confinement effects are greater.[37,38] A qualitative conclusion regarding the number of water molecules which have perturbed dynamics cannot be made based on the librational shift alone. Instead, these results illustrate that the librational dynamics of the water molecules are perturbed to a greater extent in the vicinity of the tetraanionic salts.

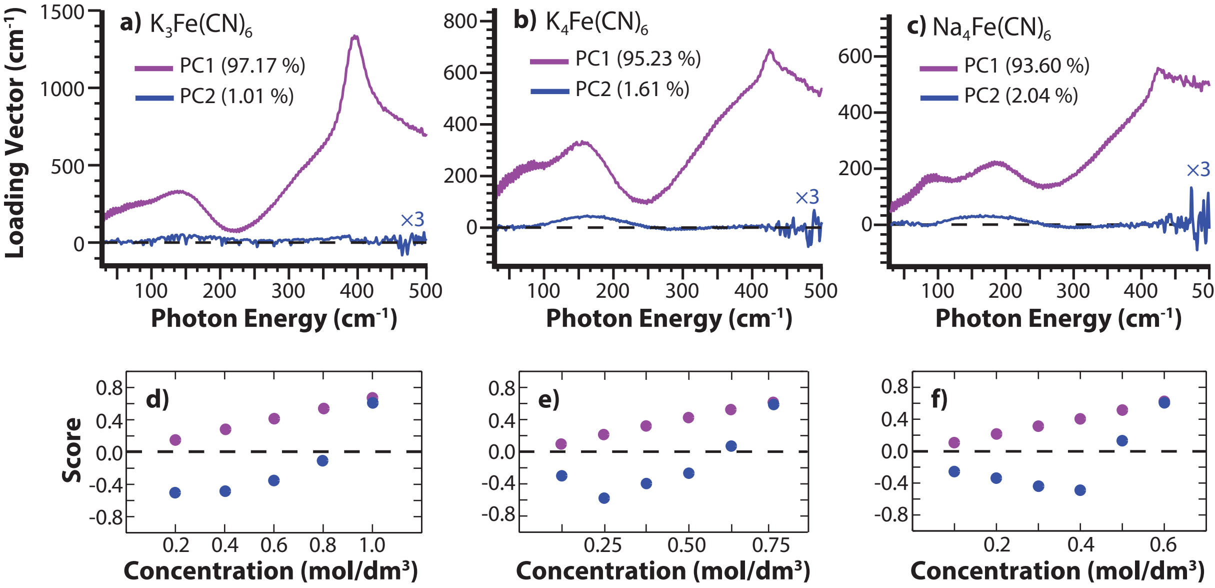

Figure 6.4: Principal component analysis for (a) $\mathrm{K_3Fe(CN)_6}$, (b) $\mathrm{K_4Fe(CN)_6}$ and (c) $\mathrm{Na_4Fe(CN)_6}$ with corresponding scores for **PC1** and **PC2** in (d) – (f). The intensity for **PC2** is expanded by 3× in order to accentuate the subtle nonlinearity from ion-pairing.

Similarly, the contributions from isolated $\mathrm{Fe(CN)}_6^{4-}$ can be removed with the difference spectra formed by subtracting $\mathrm{Na_4Fe(CN)_6}$ from $\mathrm{K_4Fe(CN)_6}$ (Figure 6.3). Inflections in the lineshape due to the $\mathrm{K^+/Na^+}$ rattling motions can be seen at $\sim$75 and $\sim$120 cm^{-1}. The high-frequency shoulder has been almost entirely removed, which either shows that the majority of intensity in this region is due to the hexacyanoferrates, or that both cations contribute similarly in this frequency range. Interestingly, a wide, positive band is centered at ~360 cm^{-1}, which could potentially result from a low-intensity peak that is overlapped by the librational shoulder and is higher in $\mathrm{K_4Fe(CN)_6}$. Finally, positive and negative peaks centered near ~145 and ~215 cm^{-1}, respectively, once again originate from a shift in the second low-frequency mode of $\varepsilon_{ion}^{eff}(\widetilde{\nu})$. If attributed only to the cations, this shift could be due to the smaller radius of $\mathrm{Na^+}$ with respect to $\mathrm{K^+}$, which also causes the shift observed for low-frequency rattling modes. However, the presence of similar residuals in this region for both difference spectra suggests that the second low-frequency peak originates neither from isolated anion nor isolated cation dynamics, but rather a third aqueous component arising from ion association. Although it is possible that the two residuals result from overlapping, separately shifting peaks that are not resolved by THz spectroscopy, the concentration dependence in this region is consistent with the nonlinearity observed previously for ion-paired solutes. Therefore, the second low-frequency peak is attributed to $\mathrm{K^+/Na^+}$ hexacyanoferrate ion-pairing.

Previous experiments have characterized concentration-dependent ion-pairing by separating the spectral contributions from isolated and paired species.[28,31,32] To separate these components for the hexacyanoferrate salts, a principle components analysis was performed on the concentration data for $\alpha_{ion}^{eff}(\widetilde{\nu})$ (Figure 6.4a-c) as described in detail previously.[28] The first principal component, **PC1**, represents the absorption data averaged over the full range of concentrations with corresponding scores (Figure 6.4d-f). The second component, **PC2**, describes nonlinear deviation relative to the average. The data for each set of salts can be almost entirely described (>95%) by summing the contributions from only these first two principal components. Although most pronounced for the tetraanionic species, all salts have a noticeable increase above baseline for **PC2** near ~150 cm^{-1} due to the nonlinearity in this region. The variance above ~400 cm^{-1} can be directly attributed to low signal as a result of strong sample absorption at these frequencies. The nonlinear component is largest for $\mathrm{Na_4Fe(CN)_6}$ with **PC2** contributing ~2%. The same analysis with $\mathrm{Mn^{2+}}$, $\mathrm{Ni^{2+}}$ and $\mathrm{Fe^{2+}}$ halide salts results in ~5% contribution from **PC2**, whereas the value for solutions of $\mathrm{Fe^{3+}}$ chloride is ~7%.[28,31] The minor extent of nonlinearity for **PC2** in the present experiments suggests that ion pairs are a significant portion of the ion population in aqueous hexacyanoferrate solutions even for concentrations as low as 200 mM, which is consistent with previous solution phase experiments that report 13% of $\mathrm{Fe(CN)_6^{3-}}$ and 46% of $\mathrm{Fe(CN)_6^{4-}}$ anions are complexed with potassium at 5 mM and 4 mM concentrations, respectively.[50–53]

6.3.3 Harmonic Fitting

In order to characterize each spectral peak and obtain an estimate for the number of water molecules perturbed by the hexacyanoferrates, the molar extinction spectra, $\varepsilon_{ion}^{eff}(\widetilde{\nu})$, for the highest concentration of each salt was fit using a set of damped harmonic oscillators:

$$\varepsilon_{DHO,i}(\widetilde{\nu}) = \frac{a_i \cdot w_i^2 \cdot \widetilde{\nu}^2}{4\pi^3 \cdot \left[\frac{\widetilde{\nu}^2 \cdot w_i^2}{\pi^2} + \left(c_i^2 + \frac{w_i^2}{4\pi^2} - \widetilde{\nu}^2\right)^2\right]} \qquad \text{(Equation 6.4)}$$

where a_i, w_i, and c_i correspond to amplitude, width, and center frequency for the damped harmonic oscillator mode, respectively, of the ith spectral component. The unperturbed center frequency for this lineshape is represented as $c_{DHO,i} = \sqrt{c_i^2 + (w_i/2\pi)^2}$, which is used throughout the following discussion. The terahertz absorption spectrum for water molecules interacting with solutes, either directly or indirectly, shifts with respect to the intrinsic frequencies of bulk water. Therefore, the concentration of water in solution, $c_{H_2O,solution}$, can be further distinguished as bulk or solvation water, where $c_{H_2O,solution} = c_{H_2O,bulk} + c_{H_2O,solvation}$. As a result, the scaled subtraction of bulk water absorption, $\alpha_{H_2O,f}(\widetilde{\nu})$, from total solution absorption, $\alpha_{solution}(\widetilde{\nu})$, in these experiments (Equation 6.2) overcompensates for the amount of bulk water actually present in solution and manifests as a negative component in the spectrum, which is modeled as a scaled bulk water extinction spectrum, $-n_{Hydration} \cdot \varepsilon_{H_2O,f}$, where $n_{Hydration}$ is the scaling factor.[28] This overcompensation is independent of transition moment strengths for absorptive modes originating from solutes or solvation water, i.e., the presence of solutes can only *diminish* the expected intensity from the lineshape of $\alpha_{H_2O,f}(\widetilde{\nu})$ by shifting the intrinsic bulk water molecule frequencies. Fitting this overcompensation can therefore effectively provide a *lower-estimate* for the number of water molecules, $n_{Hydration}$, that are perturbed from their bulk dynamic behavior as a result of ion interaction.

Both K^+ salts can be sufficiently modeled with $i = 5$ positive harmonic spectral components, but a non-physical value of $n_{Hydration} = -0.4$ is obtained for $Na_4Fe(CN)_6$ using the same model. In order to properly fit $Na_4Fe(CN)_6$ and improve the low-frequency residual for both K^+ salts (Figure A.12), one additional lineshape, which has been previously used to account for the high-frequency collective structural reorientation of water molecules in response to an external electric field, i.e., Debye relaxation,[28] was used to model all three spectra:

$$\varepsilon_{Debye}(\widetilde{\nu}) = \frac{a_0 \cdot e^{-0.00191989 \cdot \widetilde{\nu}} \cdot \widetilde{\nu}^2}{294.669 + \widetilde{\nu}^2} \qquad \text{(Equation 6.5)}$$

Further information about the fitting is discussed in detail elsewhere.[28,31] The total spectral fits for the hexacyanoferrate salts are shown in Figure 6.5 and fitting parameters from Equations 6.4 & 6.5 for each spectral component are provided in Table 6.1.

In the spectral fitting for $K_3Fe(CN)_6$ (Figure 6.5a), none of the damped harmonic parameters were restricted and therefore, the position of each component represents the best fit. In agreement with results from molar extinction and difference spectra, there is a low-frequency peak with $c_{DHO} = 73.4$ cm^{-1} that is assigned to K^+ rattling. Further spectral components consistent with the previous assignments include ion pair hydration (160.7 cm^{-1}), intramolecular Fe–C stretching (395.8 cm^{-1}) and a large shoulder from concerted librational motions

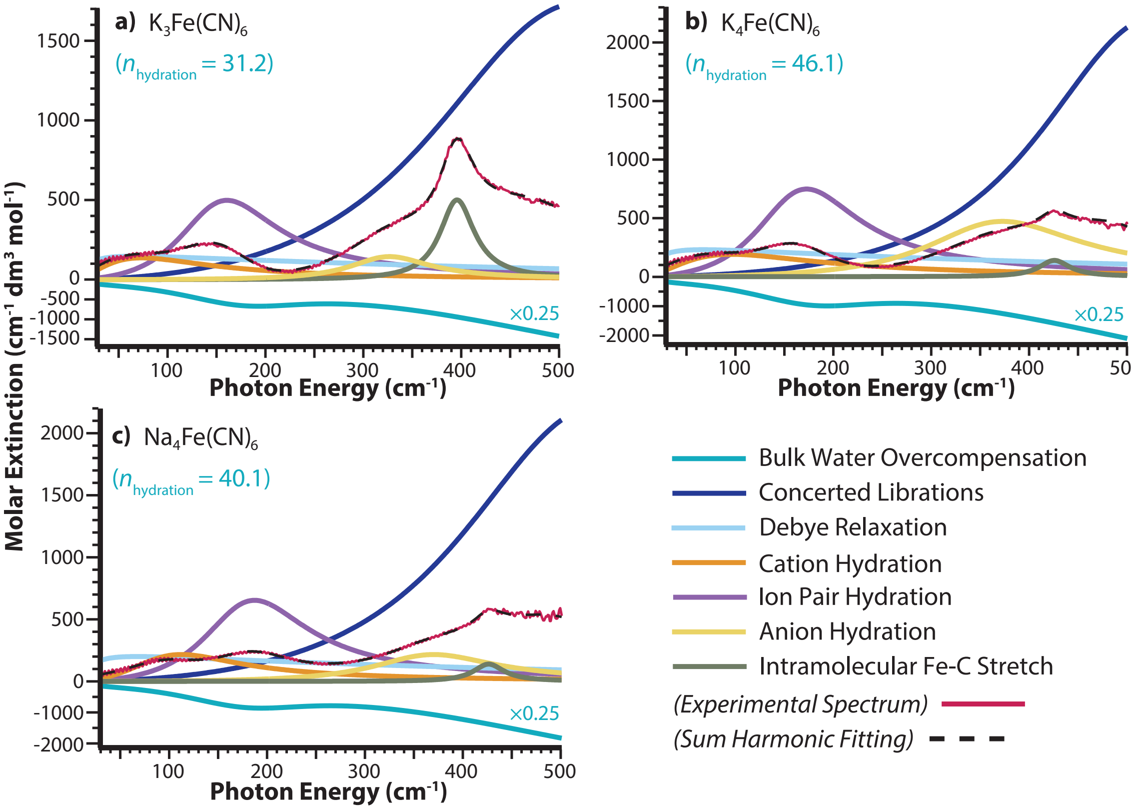

Figure 6.5: Damped harmonic fitting of $\varepsilon_{ion}^{eff}(\widetilde{\nu})$ from the highest concentration measured for (a) $K_3Fe(CN)_6$, (b) $K_4Fe(CN)_6$ and (c) $Na_4Fe(CN)_6$. The vertical axis below $\varepsilon_{ion}^{eff}(\widetilde{\nu}) = 0$ with only a negative component corresponding to bulk water overcompensation is scaled by $0.25\times$ in order to provide a closer inspection of the positive region.

(523.4 cm^{-1}). A fifth, previously unreported peak centered at 326.7 cm^{-1} is required to adequately fit the lineshape of the high-frequency shoulder. The largest residuals in the fitting below 400 cm^{-1} (where low signal due to strong absorption causes greater fluctuation) occurs in the low-frequency region below 100 cm^{-1} without the addition of a band associated with Debye relaxation (Figure A.12). In order to include $\varepsilon_{Debye}(\widetilde{\nu})$, the amplitude was increased to match the next-largest residual below 400 cm^{-1}.

Fitting $K_4Fe(CN)_6$ (Figure 6.5b) is performed by setting c_1, the damped center frequency of K^+ rattling, equal to that found for $K_3Fe(CN)_6$. All other harmonic parameters are adjusted without restriction to find the best fit. The fitting for trianionic and tetraanionic K^+ salts result in $a_1 = 1715.7$ and 2398.6 cm^{-1} dm^3 mol^{-1}, respectively, which is 571.9 and 599.6 cm^{-1} dm^3 mol^{-1} per K^+ ion. This is consistent with the near-linear behavior expected when an additional K^+ ion per mole of anion is present. A blue shift occurs for all other peaks with respect to $K_3Fe(CN)_6$. The $KFe(CN)_6^{3-}$ ion-pairing peak shifts by $\sim$11

Table 6.1: Fitting parameters for the effective ionic molar extinction of the highest measured concentration for hexacyanoferrate salts. Units are as follows: c_i (cm^{-1}), a_i (cm^{-1} dm^3 mol^{-1}) and w_i (cm^{-1}). The ±% for 2σ standard error is given in parentheses following each fitting parameter, (%). Variables that have been manually assigned in order to provide fitting consistencies between salts are marked with an asterisk, [∗].

		$K_3Fe(CN)_6$	$K_4Fe(CN)_6$	$Na_4Fe(CN)_6$
$n_{Hydration}$	Hydration Water	31.2 (16)	46.1 (6)	40.1 (5)
a_0	Debye Relaxation	178.3 [∗]	278.8 [∗]	242.2 [∗]
c_1	Cation Rattling	0.0	0.0 [∗]	86.7 (3)
a_1	Cation Rattling	1,715.7 (11)	2,398.6 (4)	2,714.8 (13)
w_1	Cation Rattling	461.3 (7)	597.3 (5)	436.7 (15)
c_2	Ion Pair Hydration	148.1 (<1)	159.2 (<1)	173.7 (1)
a_2	Ion Pair Hydration	6,257.2 (16)	9,399.8 (7)	8,207.4 (4)
w_2	Ion Pair Hydration	391.5 (7)	408.1 (3)	414.7 (3)
c_3	Anion Hydration	322.8 (<1)	359.7 (1)	361.0 (<1)
a_3	Anion Hydration	1,816.2 (13)	5,929.7 (26)	2,713.4 (32)
w_3	Anion Hydration	315.9 (9)	603.9 (10)	482.4 (16)
c_4	Fe-C Intramolecular Stretch	395.2 (<1)	425.0 (<1)	425.0 [∗]
a_4	Fe-C Intramolecular Stretch	6,292.8 (1)	1,745.1 (6)	1,745.1 [∗]
w_4	Fe-C Intramolecular Stretch	134.4 (1)	119.5 (7)	119.5 [∗]
c_5	Concerted Librational Motions	485.4 (1)	508.2 (<1)	509.5 (<1)
a_5	Concerted Librational Motions	21,872.9 (14)	27,895.3 (8)	27,902.1 (5)
w_5	Concerted Librational Motions	1,230.8 (7)	968.7 (12)	1,122.0 (9)

cm^{-1} as a result of the higher charge state. The blue shift of ∼8 cm^{-1} for the librational shoulder is attributed to the stronger nonlinear behavior of this shoulder in $K_4Fe(CN)_6$ solutions and by the negative intensity in the difference spectra comparing the two K^+ salts. The narrow Fe–C ligand stretch shifts by ∼30 cm^{-1} in agreement with previous Raman and infrared spectroscopy measurements.[57,58] Finally, the fifth additional peak required to reproduce the lineshape of the high-frequency shoulder shifts by ∼45 cm^{-1} to an unperturbed center frequency of ∼372 cm^{-1}. The amplitude for $\varepsilon_{Debye}(\widetilde{\nu})$ was adjusted until the maximum residual below 100 cm^{-1} matched the residual for the same region in the $K_3Fe(CN)_6$ fitting.

For consistency, the parameters held constant in $Na_4Fe(CN)_6$ (Figure 6.4c) are a_4, w_4, and c_4, which describe the intramolecular Fe–C stretching motion that is expected to remain the same as for $K_4Fe(CN)_6$ despite the different counterion. A blue shift occurs for both the cation rattling ($\Delta\widetilde{\nu} = 16.0$ cm^{-1}) and ion-pairing ($\Delta\widetilde{\nu} = 14.0$ cm^{-1}) bands. The former is expected from previous experiments due to the lower mass of Na^+ compared to that of K^+,[30] whereas the latter must also be attributed to cation identity and is consistent with the similar frequency shift. The high-frequency librational shoulder is extremely similar to $K_4Fe(CN)_6$ and a shift of only ∼3 cm^{-1} is observed for the fifth additional peak at 369.1

cm^{-1} used to reproduce the lineshape. This suggests that the parameters a_3, w_3, and c_3 describe anion hydration. This could be due to cross-correlation between intramolecular hexacyanoferrate modes and the fluctuating dipole of surrounding water molecules, which has been observed previously in the terahertz spectra for correlated glycine-water absorption peaks with comparable widths,[56] or to concerted water molecule modes that are infrared-inactive in the absence of ion pairs. However, the center frequency for this absorption depends more strongly on the anionic charge state than cation identity and therefore, we have assigned this peak to anion hydration. The larger value for a_3 in $K_4Fe(CN)_6$ with respect to $Na_4Fe(CN)_6$ is consistent with the wide, low-intensity band in the difference spectrum. Since the amplitude for Debye relaxation (a_0) in fitting $Na_4Fe(CN)_6$ significantly influences the amplitude of the ion-pairing peak (a_2), a_0 was adjusted until the ratio of a_2 with respect to this parameter in $K_4Fe(CN)_6$ matched their relative intensities in this region of the experimental spectra.

The scaled negative contribution due to bulk water overcompensation in these fittings results in $n_{Hydration} = 31.2$, 46.1 and 40.1 for $K_3Fe(CN)_6$, $K_4Fe(CN)_6$ and $Na_4Fe(CN)_6$, respectively. These values represent a lower-limit to the number of water molecules perturbed by the presence of ions, i.e., some minor influences may not result in observable frequency shifts in the terahertz spectrum. The value of $n_{Hydration}$ is calculated with respect to one mole of solute and therefore, the dynamics of 31.2 water molecules in total are perturbed by 3 K^+ cations and a single $Fe(CN)_6^{3-}$ anion for the $K_3Fe(CN)_6$ solution (neglecting observed contributions from ion-pairing). The number of water molecules coordinated to free Na^+ and K^+ ions is ∼5 and 6, respectively.[59–61] The smaller value of $n_{Hydration}$ for the Na^+ salt with respect to K^+ is thus consistent with Na^+ ions coordinating fewer water molecules. Although the highest concentration for each salt was used, the fitting is performed on the concentration-independent molar extinction, $\varepsilon_{ion}^{eff}(\widetilde{\nu})$. With ∼55 water molecules per mole of solute, the values of $n_{Hydration}$ reveal that some bulk water is unperturbed or experiences only minor interactions that are not observed by THz spectroscopy. Therefore, these values for $n_{Hydration}$ will not change appreciably by fitting the molar extinction from more dilute solutions.

Considering the approximate values for cation coordination, the bare hexacyanoferrates must influence at least 13.2 water molecules for $Fe(CN)_6^{3-}$ ($31.2\ H_2O - 6\ H_2O \times 3\ K^+$) and 22.1 or 20.1 water molecules for $Fe(CN)_6^{4-}$ from the K+ or Na^+ salt, respectively. However, these values intrinsically underestimate the number of water molecules influenced by the bare anions because they do not account for ion-pairing, which effectively liberates the solvation shell of one cation. For example, if we assume all anions are paired with a single cation in solution, then $KFe(CN)_6^{2-} + 2K^+$ collectively influence 31.2 water molecules. This leaves 19.2, 28.1 and 25.1 water molecules perturbed by the ion pairs $KFe(CN)_6^{2-}$, $KFe(CN)_6^{3-}$ and $NaFe(CN)_6^{3-}$, respectively. The smaller value for $NaFe(CN)_6^{3-}$ is consistent with the higher charge density of Na^+ reducing the Coulombic interaction of the complex with surrounding water molecules. Ion-pairing reduces the effective potential of the complex and results in diminished ion-water interactions. Therefore, if the majority of the population is ion-paired, then the bare hexacyanoferrates must influence an even larger number of water molecules than are calculated here for the ion pairs. Based on previous solution phase experiments,[50–53] 13% of $\mathrm{Fe(CN)}_6^{3-}$ and 46% of $\mathrm{Fe(CN)}_6^{4-}$ anions are paired with K^+ at 5 mM and 4 mM concentrations, respectively. Our highest concentrations exceed these concentrations by over 100× and therefore, we expect that ion-pairs contribute substantially in these solutions. The first solvation shell for hexacyanoferrates determined from the calculated radial distribution function of a single anion in large aqueous nanodrops and from the density of water is $\sim$13 water molecules.[38] Therefore, even the minimum values reported here represent ion-water influences that extend beyond the inner hydration shell.

6.4 Summary and Conclusions

This is the first report of the low-frequency dynamics of aqueous multivalent hexacyanoferrate salts and the surrounding water molecules using terahertz spectroscopy. Absorptions in this region include cation rattling, ion-pairing, intermolecular cross-correlations, intramolecular stretching, and concerted water molecule librational motions. These results illustrate the extended influence that high charge-density anions can have on water molecule dynamics. There is a blue shift of the absorption band attributed to ion-pairing for the tetraanionic salts with respect to $\mathrm{K_3Fe(CN)_6}$ that is consistent with a stronger confinement of water molecules in the proximity of the tetravalent anion that results in perturbed dynamical motions. There are only minor nonlinear absorptions in $\varepsilon_{ion}^{eff}(\widetilde{\nu})$ for the concentration dependence of cation rattling and ion-pairing absorptions. Although larger nonlinear changes have been reported previously for transition metal halides,[28,31] the lesser concentration dependence in the hexacyanoferrates is likely due to their high propensity for ion-pairing even at low concentrations, i.e., high ion association constants. However, these small non-linearities can still provide valuable insight into concentration-dependent interactions.

The number of water molecules with perturbed dynamics was measured by fitting a scaled negative bulk water contribution to $\varepsilon_{ion}^{eff}(\widetilde{\nu})$ for each salt. For example, an aqueous 1.0 M solution of $\mathrm{K_3Fe(CN)_6}$ consists of a single $\mathrm{Fe(CN)}_6^{3-}$ anion for every 3 K^+ and $\sim$47 water molecules, of which a minimum of $\sim$32 are perturbed by the solutes based on the scaled fitting with $-\alpha_{H_2O,f}(\widetilde{\nu})$. Nonlinearities in the ion-pairing band indicate that these solutions contain a major contribution from $\mathrm{KFe(CN)}_6^{2-}$, $\mathrm{KFe(CN)}_6^{3-}$ and $\mathrm{NaFe(CN)}_6^{3-}$ ion pairs, which independently perturb the dynamics of 19.2, 28.1 and 25.1 water molecules, respectively, in their vicinity. These values represent a lower estimate, because further contributions from free K^+ and Na^+ ions may also act to effectively shield the anionic influence at further distances and minor long-distance influences may not be apparent in the THz spectrum. With the large number of variables for fitting, another physically-consistent set of parameters may fit the data set to an equal or better extent. However, the current parameters provide a self-consistent fit and are in agreement with assignments from previous results.

A shift for solution absorptions in the terahertz region with respect to bulk water is attributable to a change in the collective *dynamics* of water molecules in the vicinity of solutes. This differs from the characteristics of these same isolated anions inside aqueous nanodrops probed in previous experiments, where *structural* changes of remote water molecules reflect the distal extent of ions influencing water molecule orientation. Although $Fe(CN)_6^{4-}$ was previously found to structurally orient water molecules into the fourth solvation shell of aqueous nanodrops,[38] the temperature of these droplets is colder than the room temperature solutions probed in the present study and therefore, we might expect the influences of the ion on water structure and dynamics observed in nanodrops to be slightly diminished. Furthermore, the ion-pairing and shielding by counterions in solution reduces the effective charge of these complexes at the high concentrations used in these THz experiments and as a result, the number of water molecules perturbed is expected to be lower than in an effectively infinitely dilute solution of $Fe(CN)_6^{3-}$ or $Fe(CN)_6^{4-}$ without cations. However, both experiments reveal ion-water interactions that persist beyond the inner hydration shell. Observation of these extended interactions provides insight into how ions can influence water molecules in confined regions, such as cellular fluids, reverse micelles and nanopourous materials.

6.5 References

[1] Collins, K. D.; Neilson, W., George; Enderby, J. E. *Biophys. Chem.* **2007**, *128*, 95–104.

[2] Marcus, Y. *Chem. Rev.* **2009**, *109*, 1346–1370.

[3] Scott, J. N.; Nucci, V., Nathaniel; Vanderkooi, J. M. *J. Phys. Chem. A* **2008**, *112*, 10939–10948.

[4] Song, J.; Kang, T. H.; Kim, M. W.; Han, S. *Phys. Chem. Chem. Phys.* **2015**, *17*, 8306–8322.

[5] O'Brien, J. T.; Williams, E. R. *J. Am. Chem. Soc.* **2012**, *134*, 10228–10236.

[6] Cooper, R. J.; DiTucci, M. J.; Chang, T. M.; Williams, E. R. *J. Am. Chem. Soc.* **2016**, *138*, 96–99.

[7] Enghoff, M. B.; Svensmark, H. *Atmos. Chem. Phys.* **2008**, *8*, 4911–4923.

[8] Ball, P. *Nature* **2011**, *478*, 467–468.

[9] Fu, F.; Wang, Q. *J. Environ. Manage.* **2011**, *92*, 407–418.

[10] Marcus, Y.; Hefter, G. *Chem. Rev.* **2006**, *106*, 4585–4621.

[11] Mancinelli, R.; Botti, A.; Bruni, F.; Ricci, M. A. *J. Phys. Chem. B* **2007**, *111*, 13570–13577.

[12] Sonderholm, L.; Skanthakumar, S.; Wilson, R. E. *J. Phys. Chem. A* **2009**, *113*, 6391–6397.

[13] Pestova, O. N.; Kostikov, Y. P.; Khripun, M. K. *Russ. J. Appl. Chem.* **2004**, *77*, 1066–1069.

[14] Mason, P. E.; Cruickshank, J. M.; Neilson, G. W.; Buchanan, P. *Phys. Chem. Chem. Phys.* **2003**, *5*, 4686–4690.

[15] Mancinelli, R.; Botti, A.; Bruni, F.; Ricci, M. A.; Soper, A. K. *Phys. Chem. Chem. Phys.* **2007**, *9*, 2959–2967.

[16] Bleuzen, A.; Foglia, F.; Furet, E.; Helm, L.; Merbach, A. E.; Weber, J. *J. Am. Chem. Soc.* **1996**, *118*, 12777–12787.

[17] Vovk, M. A.; Pavlova, M. S.; Chizhik, V. I.; Vorontsova, A. A. *Russ. J. Phys. Chem. A* **2011**, *85*, 1597–1602.

[18] Chizhik, V. I. *Mol. Phys.* **1997**, *90*, 653–659.

[19] Rudolph, W. W.; Irmer, G. *Appl. Spectrosc.* **2007**, *61*, 1312–1327.

[20] Bergström, P.-Å.; Lindgren, J. *J. Phys. Chem.* **1991**, *95*, 7650–7655.

[21] Stangret, J.; Gampe, T. *J. Phys. Chem. A* **2002**, *106*, 5393–5402.

[22] Buchner, R. *Pure Appl. Chem.* **2008**, *80*, 1239–1252.

[23] Eiberweiser, A.; Nazet, A.; Hefter, G.; Buchner, R. *J. Phys. Chem. B* **2015**, *119*, 5270 – 5281.

[24] Jia, G.-Z.; Liu, S.; Liu, F.-H.; Liu, J.-C. *J. Dispersion Sci. Technol.* **2016**, 1–5.

[25] Russo, D.; Hura, G.; Head-Gordon, T. *Biophys. J.* **2004**, *86*, 1852–1862.

[26] Moilanen, D. E.; Wong, D.; Rosenfeld, D. E.; Fenn, E. E.; Fayer, M. D. *Proc. Natl. Acad. Sci. USA* **2009**, *106*, 375–380.

[27] Heyden, M.; Sun, J.; Funkner, S.; Mathias, G.; Forbert, H.; Havenith, M.; Marx, D. *Proc. Natl. Acad. Sci. USA* **2010**, *107*, 12068–12073.

[28] Sharma, V.; Böhm, F.; Schwaab, G.; Havenith, M. *Phys. Chem. Chem. Phys.* **2014**, *16*, 25101–25110.

[29] Bründermann, E.; Born, B.; Funkner, S.; Krüger, M.; Havenith, M. *Proc. SPIE* **2009**, *7215*, 72150E.

[30] Schmidt, D. A.; Birer, Ö.; Funkner, S.; Born, B. P.; Gnanasekaran, R.; Schwaab, G. W.; Leitner, D. M.; Havenith, M. *J. Am. Chem. Soc.* **2009**, *131*, 18512–18517.

[31] Böhm, F.; Sharma, V.; Schwaab, G.; Havenith, M. *Phys. Chem. Chem. Phys.* **2015**, *17*, 19582–19591.

[32] Sharma, V.; Böhm, F.; Seitz, M.; Schwaab, G.; Havenith, M. *Phys. Chem. Chem. Phys.* **2013**, *15*, 8383–8391.

[33] Funkner, S.; Niehues, G.; Schmidt, D. A.; Heyden, M.; Schwaab, G.; Callahan, K. M.; Tobias, D. J.; Havenith, M. *J. Am. Chem. Soc.* **2012**, *134*, 1030–1035.

[34] Niehues, G.; Heyden, M.; Schmidt, D. A.; Havenith, M. *Faraday Discuss.* **2011**, *150*, 193–207.

[35] Ebbinghaus, S.; Meister, K.; Born, B.; DeVries, A. L.; Gruebele, M.; Havenith, M. *J. Am. Chem. Soc.* **2010**, *132*, 12210–12211.

[36] O'Brien, J. T.; Prell, J. S.; Bush, M. F.; Williams, E. R. *J. Am. Chem. Soc.* **2010**, *132*, 8248–8249.

[37] DiTucci, M. J.; Heiles, S.; Williams, E. R. *J. Am. Chem. Soc.* **2015**, *137*, 1650 – 1657.

[38] DiTucci, M. J.; Williams, E. R. *Chem. Sci.* **2017**, *8*, 1391–1399.

[39] Marcus, Y. *J. Solution Chem.* **1994**, *23*, 831–848.

[40] Sando, G. M.; Zhong, Q.; Owrutsky, J. C. *J. Chem. Phys.* **2004**, *121*, 2158–2168.

[41] Yu, P.; Yang, F.; Zhao, J.; Wang, J. *J. Phys. Chem. B* **2014**, *118*, 3104–3114.

[42] Kumar, A.; Yusuf, S. M. *Phys. Rev. B* **2007**, *75*, 224419.

[43] Rabinowitz, J. D.; Vacchino, J. F.; Beeson, C.; McConnell, H. M. *J. Am. Chem. Soc.* **1998**, *120*, 2464–2473.

[44] Wang, P. G.; Xian, M.; Tang, X.; Wu, X.; Wen, Z.; Cai, T.; Janczuk, A. J. *Chem. Rev.* **2002**, *102*, 1091–1134.

[45] Gail, E.; Gos, S.; Kulzer, R.; Lorösch, J.; Rubo, A.; Sauer, M.; Kellens, R.; Reddy, J.; Steier, N.; Hasenpusch, W. *"Cyano Compounds, Inorganic", Ullmann's Encyclopedia of Industrial Chemistry, Electronic Release*; Wiley-VCH, Weinheim, 2012.

[46] Pyrasch, M.; Toutianoush, A.; Jin, W.; Schnepf, J.; Tieke, B. *Chem. Mater.* **2003**, *15*, 245–254.

[47] Faustino, P. J. et al. *J. Pharm. Biomed. Anal.* **2008**, *47*, 114 –125.

[48] Neff, V. D. *J. Electrochem. Sci. Technol.* **1985**, *132*, 1382–1384.

[49] Jang, S. C.; Hong, S. B.; Yang, H. M.; Lee, K. W.; Moon, J. K.; Seo, B. K.; Huh, Y. S.; Roh, C. *Nanomaterials* **2014**, *4*, 894 – 901.

[50] Eaton, W. A.; George, P.; Hanania, G. I. H. *J. Phys. Chem.* **1967**, *71*, 2016–2021.

[51] Hanania, G. I. H.; Irvine, D. H.; Eaton, W. A.; George, P. *J. Phys. Chem.* **1967**, *71*, 2022–2030.

[52] Kolthoff, I. M.; Tomsicek, W. J. *J. Phys. Chem.* **1934**, *39*, 945–954.

[53] Cohen, S. R.; Plane, R. A. *J. Phys. Chem.* **1957**, *61*, 1096–1100.

[54] Haynes, W. M., Ed. *"Physical Constants of Organic Compounds", in CRC Handbook of Chemistry and Physics*, 97th ed.; CRC Press/Taylor & Francis: Boca Raton, FL, 2017.

[55] Bertie, J. E.; Lan, Z. *Appl. Spectrosc.* **1996**, *50*, 1047–1057.

[56] Sun, J.; Niehues, G.; Forbert, H.; Decka, D.; Schwaab, G.; Marx, D.; Havenith, M. *J. Am. Chem. Soc.* **2014**, *136*, 5031–5038.

[57] Griffith, W. P.; Turner, G. T. *J. Chem. Soc. A* **1970**, 858–862.

[58] Jones, L. H. *Inorg. Chem.* **1963**, *2*, 777–780.

[59] Soper, A. K.; Weckström, K. *Biophys. Chem.* **2006**, *124*, 180–191.

[60] Bucher, D.; Guidoni, L.; Carlioni, P.; Rothlisberger, U. *Biophys. J.* **2010**, *98*, 47–49.

[61] Skipper, N. T.; Neilson, G. W. *J. Phys.: Condens. Matter* **1989**, *1*, 4141–4154.

Chapter 7

Conclusion

7.1 Summary and Future Directions

This collection of research has provided unique insight into ion-water interactions that lead to stabilities in multivalent anions as well as remote structural and dynamic perturbations to water molecules beyond the inner coordination shell. Many of these observations are made possible by utilization of a home-built FT-ICR mass spectrometer that guides nESI generated ion-containing nanodroplets from the heated inlet capillary to the storage cell using "soft" electrostatic optics, *i.e.* omission of multipolar radio frequency ion traps preceding the ion cell avoids excessive excitation of the aqueous droplets, which leads to larger droplet sizes than observed with their inclusion. Studying the chemical and physical properties of solvated ions in aqueous nanodroplets overcomes many of the shortcomings present in the condensed phase, where the high concentrations required for adequate signal result in very little bulk water and an abundance of counterions. Furthermore, the recent advancement of data analysis techniques for FT-THz spectroscopy has resulted in unique methods for discerning remote dynamic ion-water interactions. Despite a continued debate that ion-water interactions are only local,[1–3] we have presented unambiguous evidence for second shell solvation required for the intrinsic stability of tetravalent $\mathrm{Fe(CN)_6^{4-}}$ (Chapter 3),[4] remote structural perturbations in the surface structure of water molecules in aqueous nanodroplets into a fourth solvation shell at nanometer distance (Chapters 2 & 3),[4,5] second shell ion-induced structuring in droplets at temperatures relevant to Earth's upper atmosphere (Chapters 4 & 5),[6] and dynamic perturbations to water molecules beyond the inner solvation shell of solution-phase hexacyanoferrates at room temperature (Chapter 6).[7]

With the exception of MCA stabilities in Chapters 2 & 3, the primary focus of these experiments has been to probe how the presence of ions can lead to measurable changes in solvating water molecules. Although this approach is necessary for understanding the extent to which ions can influence their environments, we can conversely ask how the presence of water molecules can lead to measurable changes in the solvated ions. This question cannot be easily answered using IRPD in the O—H stretching region between $\sim 2800 - 4000\ \mathrm{cm^{-1}}$, because as nanodroplets become increasingly larger, so too does the absorption cross section for hydrogen-bonded O—H oscillators, whose intensity obfuscates intramolecular information concerning the solvated ions. Understanding the effective concentrations for which ion pairs transition between direct contact, shared solvent, or multilayer solvent-separated pairs is challenging because the majority of condensed phase techniques cannot differentiate between these different pairing motifs.[8–10] However, future IRPD experiments for nanodroplets containing ion pairs can utilize mid-infrared radiation in the region between ∼800 − 2800 cm^{-1}, corresponding to N—H bends, N=O stretches, and C=O stretches, which each have absorption cross sections that are comparable to the free and bonded O—H intensities reported in this body of work. Because these oscillators are sensitive to their local environments, mid-IRPD spectra can be measured as a function of nanodroplet hydration size to observe N=O frequency shifts in $\mathrm{Pb}^{2+}\mathrm{NO}_3^-$ and $\mathrm{Sr}^{2+}\mathrm{NO}_3^-$ and compared with calculated harmonic spectra to determine transitions between different pairing motifs. These experiments can be performed with a simple modification to our current OPO/OPA system by installation of a AgGaSe_2 crystal, through which the current output can undergo difference frequency generation to produce photons between ∼800 − 2800 cm^{-1}.[11–13]

The extensive master equation modeling performed to determine effective temperatures of $\mathrm{SO}_4^{2-}(\mathrm{H}_2\mathrm{O})_n$ between $n = 30-45$ (Chapter 5) can be easily extended to larger droplet sizes as well as cation-containing nanodroplets. Preliminary results in the size regime between $n = 30 - 45$ have suggested a relation between the low-pressure Arrhenius slope and the extent of evaporative cooling. This approach can potentially provide a means for estimating effective droplet temperatures without the need to perform extensive modeling. To improve the robustness of this model, larger droplet sizes must be investigated along with a variety of solvated ions with varying charge states. Furthermore, the range of values used for the high-pressure pre-exponential factor, A^{∞}, can potentially be narrowed by using the measured E_0 values for cations in previous photoexcitation experiments.[14] This approach can lower the uncertainty in modeling the effective temperatures of ion-containing nanodroplets.

Whereas droplets stored in the ion cell of a mass spectrometer undergo rapid evaporative cooling that requires modeling of thermal precursor distributions, the associated THz experiments (Chapter 6), which revealed long-distance dynamic interactions at room temperature, can be extended to nanodroplets generated under ambient conditions. A broadband THz beam positioned perpendicular to a macrospray ESI emitter can be used to probe the dynamics of water molecules confined in droplets. Absorption as a function of droplet size can be measured by varying the distance of the THz beam from the emitter tip and initial droplet sizes can be estimated based on the emitter diameter.[15] We expect sufficient attenuation can be achieved if the beam passes through ∼25 µm cumulative sample length (neglecting void space between droplets),[7] which can be increased by using a larger diameter ESI emitter. These experiments can be performed with and without ions in order to investigate dynamic changes as a result of the ionic influences. In addition to the results provided here, a wealth of information is left to be explored through aqueous nanodroplet experiments, which will continue to provide fruitful molecular-level insight into ion-water interactions.

7.2 References

[1] Stirnemann, G.; Wernersson, E.; Jungwirth, P.; Laage, D. *J. Am. Chem. Soc.* **2013**, *135*, 11824–11831.

[2] Omta, A. W.; Kropman, M. F.; Woutersen, S.; Bakker, H. J. *Science* **2003**, *301*, 347–349.

[3] Okur, H. I.; Hladílková, J.; Rembert, K. B.; Cho, Y.; Heyda, J.; Dzubiella, J.; Cremer, P. S.; Jungwirth, P. *J. Phys. Chem. B* **2017**, *121*, 1997–2014.

[4] DiTucci, M. J.; Williams, E. R. *Chem. Sci.* **2017**, *8*, 1391–1399.

[5] DiTucci, M. J.; Heiles, S.; Williams, E. R. *J. Am. Chem. Soc.* **2015**, *137*, 1650 – 1657.

[6] DiTucci, M. J.; Stachl, C. N.; Williams, E. R. *Manuscript in Progress* **2017**,

[7] DiTucci, M. J.; Böhm, F.; Schwaab, G.; Williams, E. R.; Havenith, M. *Phys. Chem. Chem. Phys.* **2017**, *19*, 7297–7306.

[8] Bračko, S.; Špan, J. *Dyes Pigm.* **2000**, *45*, 97–102.

[9] Petrauskas, V.; Maximowitsch, E.; Matulis, D. *J. Phys. Chem. B* **2015**, *119*, 12164–12171.

[10] Tretyakov, D. O.; Prisiazhnyl, V. D.; Gafurov, M. M.; Rabadanov, K. S.; Kirillov, S. A. *J. Chem. Eng. Data* **2010**, *55*, 1958–1964.

[11] Gerhards, M.; Unterberg, C.; Gerlach, A. *Phys. Chem. Chem. Phys.* **2002**, *4*, 5563–5565.

[12] Stearns, J. A.; Das, A.; Zwier, T. S. *Phys. Chem. Chem. Phys.* **2004**, *6*, 2605–2610.

[13] Diken, E. G.; Headrick, J. M.; Roscioli, J. R.; Bopp, J. C.; Johnson, M. A.; McCoy, A. B.; Huang, X.; Carter, S.; Bowman, J. M. *J. Phys. Chem. A* **2005**, *109*, 571–575.

[14] Heiles, S.; Cooper, R. J.; DiTucci, M. J.; Williams, E. R. *Chem. Sci.* **2017**, *8*, 2973–2982.

[15] Susa, A. C.; Xia, Z.; Williams, E. R. *Anal. Chem.* **2017**, *89*, 3116–3122.

Appendix A

Supplementary Figures

The figures in this appendix are reproduced with permission from:

Matthew J. DiTucci, Sven Heiles, and Evan R. Williams

"Role of Water in Stabilizing Ferricyanide Trianion and Ion-Induced Effects to the Hydrogen Bonding Water Network at Long Distance", *J. Am. Chem. Soc.* **2015**, *137*, 1650–1657.

Matthew J. DiTucci and Evan R. Williams

"Nanometer Patterning of Water by Tetraanionic Ferrocyanide Stabilized in Aqueous Nanodrops", *Chem. Sci.* **2017**, *8*, 1391–1399.

Matthew J. DiTucci, Christiane N. Stachl, and Evan R. Williams

"Calculating the Steady State Effective Temperatures of Aqueous Sulfate Nanodrops via Master Equation Modeling", *Manuscript in Preparation for Submission,* **2017**.

Matthew J. DiTucci, Fabian Böhm, Gerhard Schwaab,
Evan R. Williams, and Martina Havenith

"Effects of Multivalent Hexacyanoferrates and Their Ion Pairs on Water Molecule Dynamics Measured with Terahertz Spectroscopy", *Phys. Chem. Chem. Phys.* **2017**, *19*, 7297–7306.

A.0.1 Additional Figures for Chapter 2

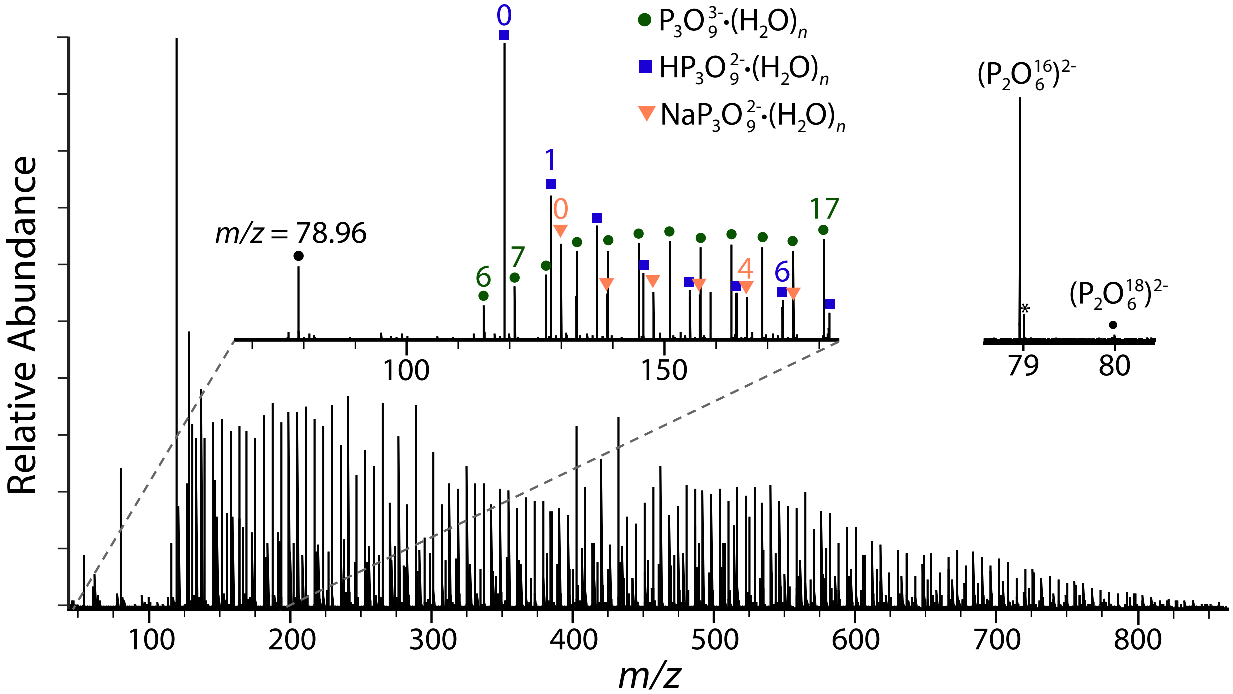

Figure A.1: A nESI mass spectrum obtained from 5 mM aqueous solution of $Na_3P_3O_9$ showing formation of $P_3O_9^{3-}(H_2O)_n$ with $n \geq 6$ using the same experimental conditions as those used to produce similar size $Fe(CN)_6^{3-}(H_2O)_n$. Insets show expanded low m/z region and the peak at $m/z = 78.96$, which corresponds to $P_2O_6^{2-}$. Frequency noise is labeled with an asterisk ($*$).

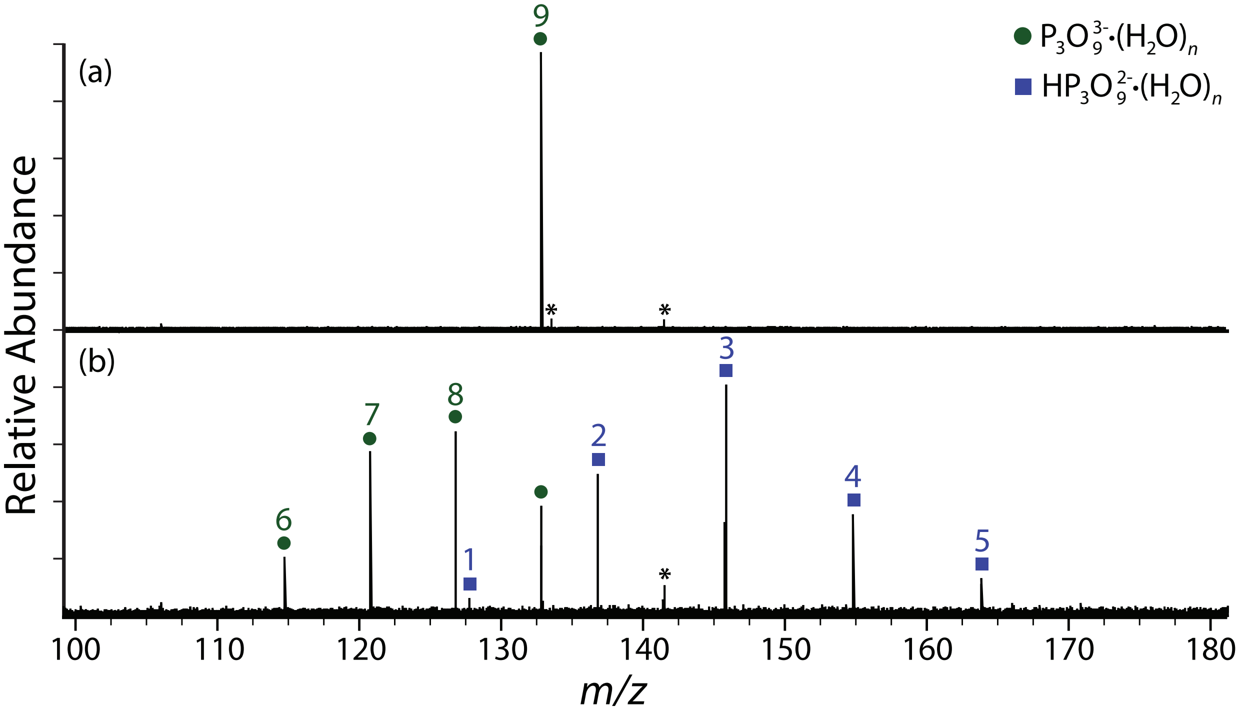

Figure A.2: nESI of a 5 mM aqueous solution of $Na_3P_3O_9$ to produce $P_3O_9^{3-}(H_2O)_n$ with $n \geq 6$ showing (a) isolated $P_3O_9^{3-}(H_2O)_9$ and (b) infrared dissociation of this ion at 3438 cm^{-1} for 60 s showing product ions $HP_3O_9^{2-}(H_2O)_{1-5}$ formed by a charge separation process corresponding to loss of $OH^-(H_2O)_y$.

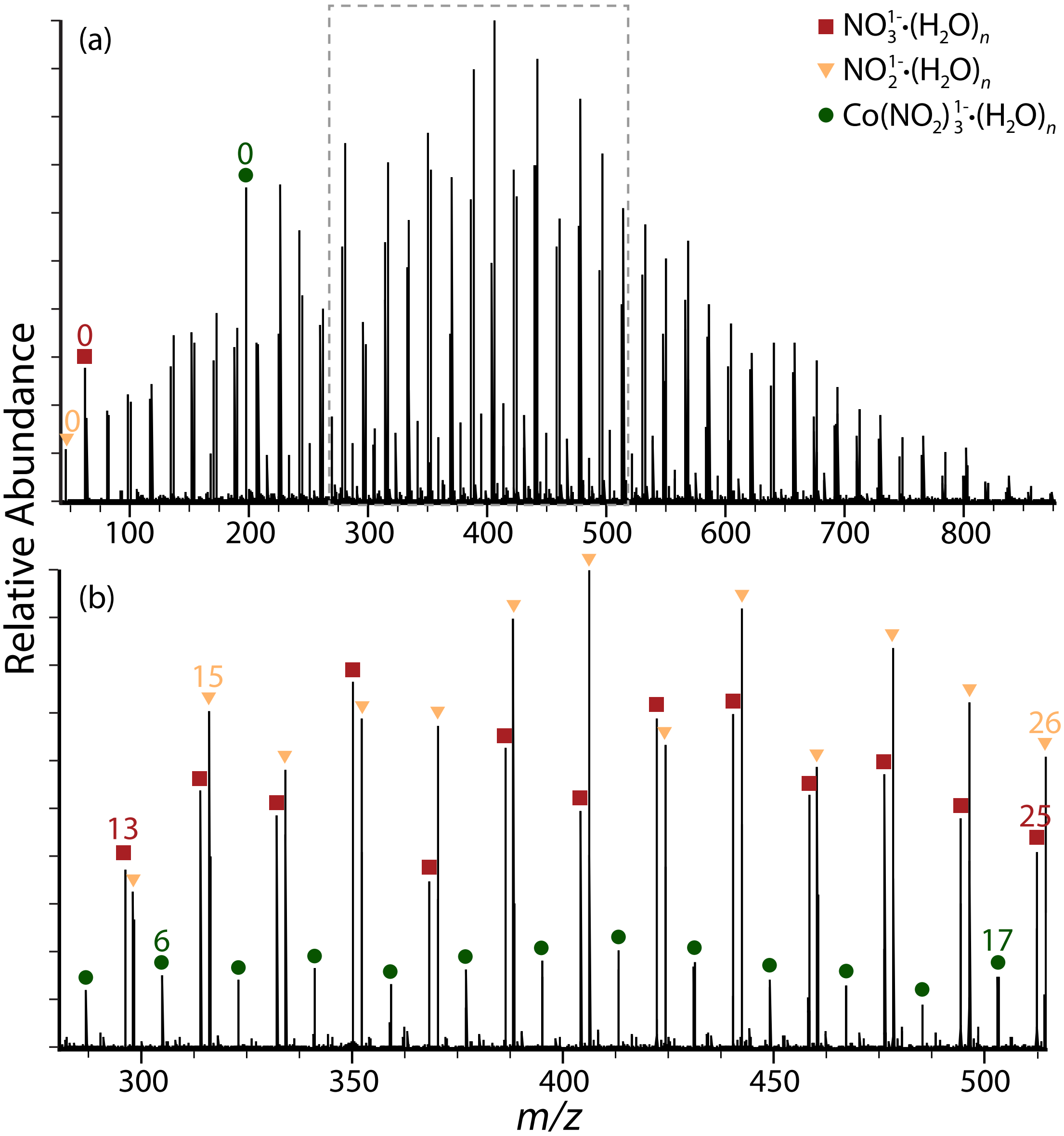

Figure A.3: nESI mass spectra obtained from 5 mM aqueous solution of $Na_3Co(NO_2)_6$ measured with the same experimental conditions used to generate similar size $Fe(CN)_6^{3-}(H_2O)_n$.

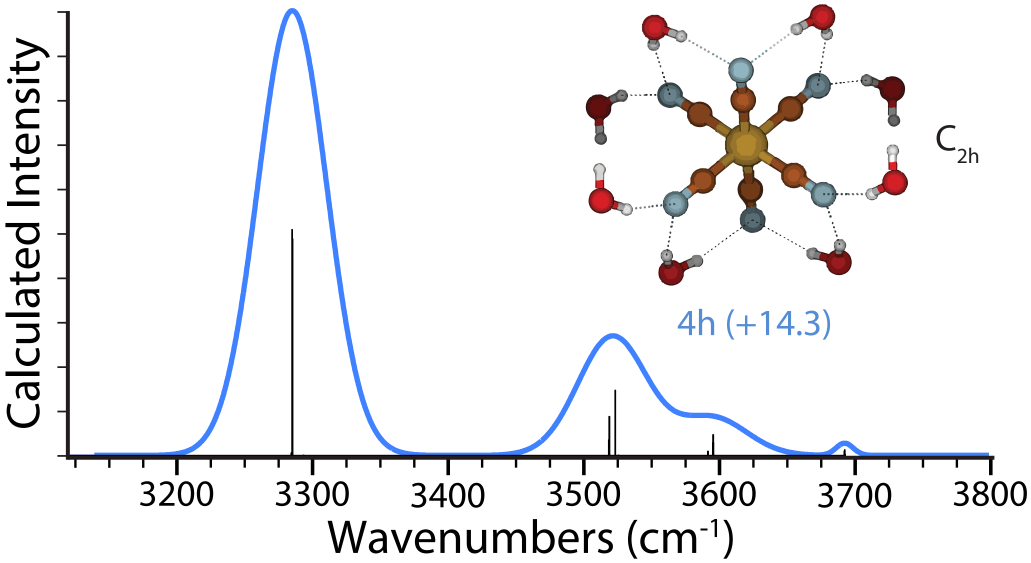

Figure A.4: Calculated spectrum for structure **4h** at the B3LYP/LACVP++** level. This structure originates from a configurational change during MP2/VTZ optimization of structure **4d** from B3LYP/LACVP++**. Gibbs free energy (in kJ/mol at 133 K) relative to the lowest-energy structure **4b** (Figure 2.4) is inset with value from MP2/VTZ. The point group for this structure is listed to the right.

A.0.2 Additional Figures for Chapter 3

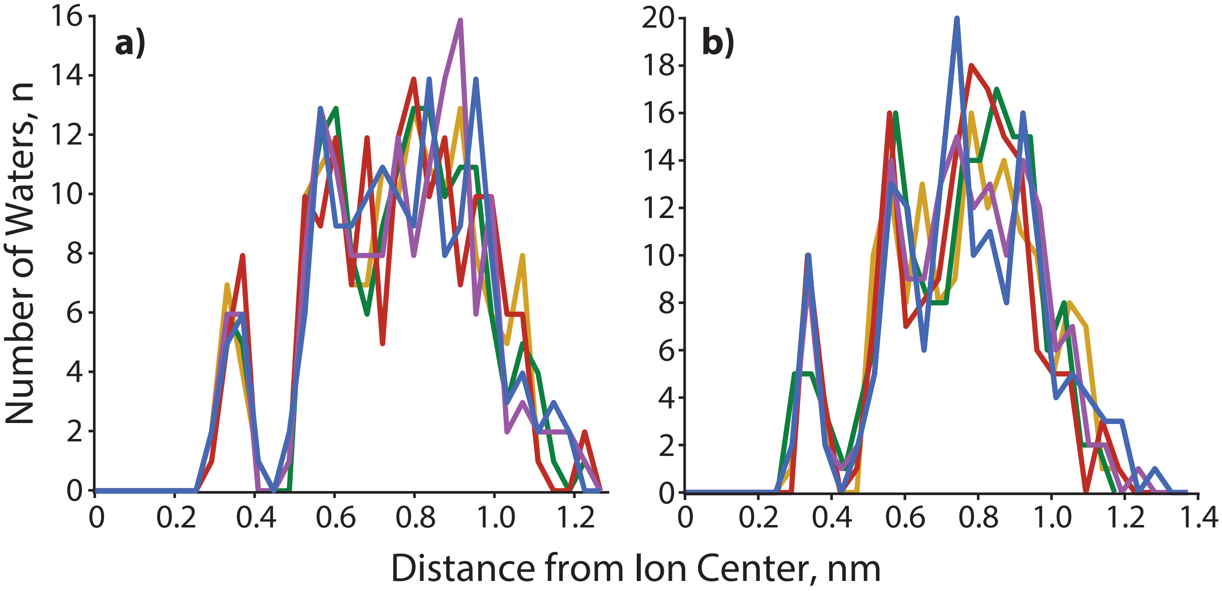

Figure A.5: Comparison of the radial distribution functions for five individual structures of $Fe(CN)_6^{4-}(H_2O)_{160}$, each plotted as a different color and taken from (a) 20 ps separations within the final 1 ns of a single annealing cycle and (b) the final structure within the last 1 ns of five separate annealing cycles. These plots illustrate that although the RMS displacement of a single water molecule at 133 K during the last 1 ns of a single cycle is $\sim 0.78 \pm 0.24$ Å, there is still an appreciable change to the overall nanodrop within this 20 ps timescale. The use of a simulated annealing cycle increases the RMS displacement for a single water molecule to $\sim 10.07 \pm 1.95$ Å, which indicates the potential energy of the system is sufficient to overcome local minima and exchange water molecules between hydration shells. The structure of a fourth solvation shell is apparent in the single distributions, which were used to calculate an average center of ~1.10 nm (Figure 3.7).

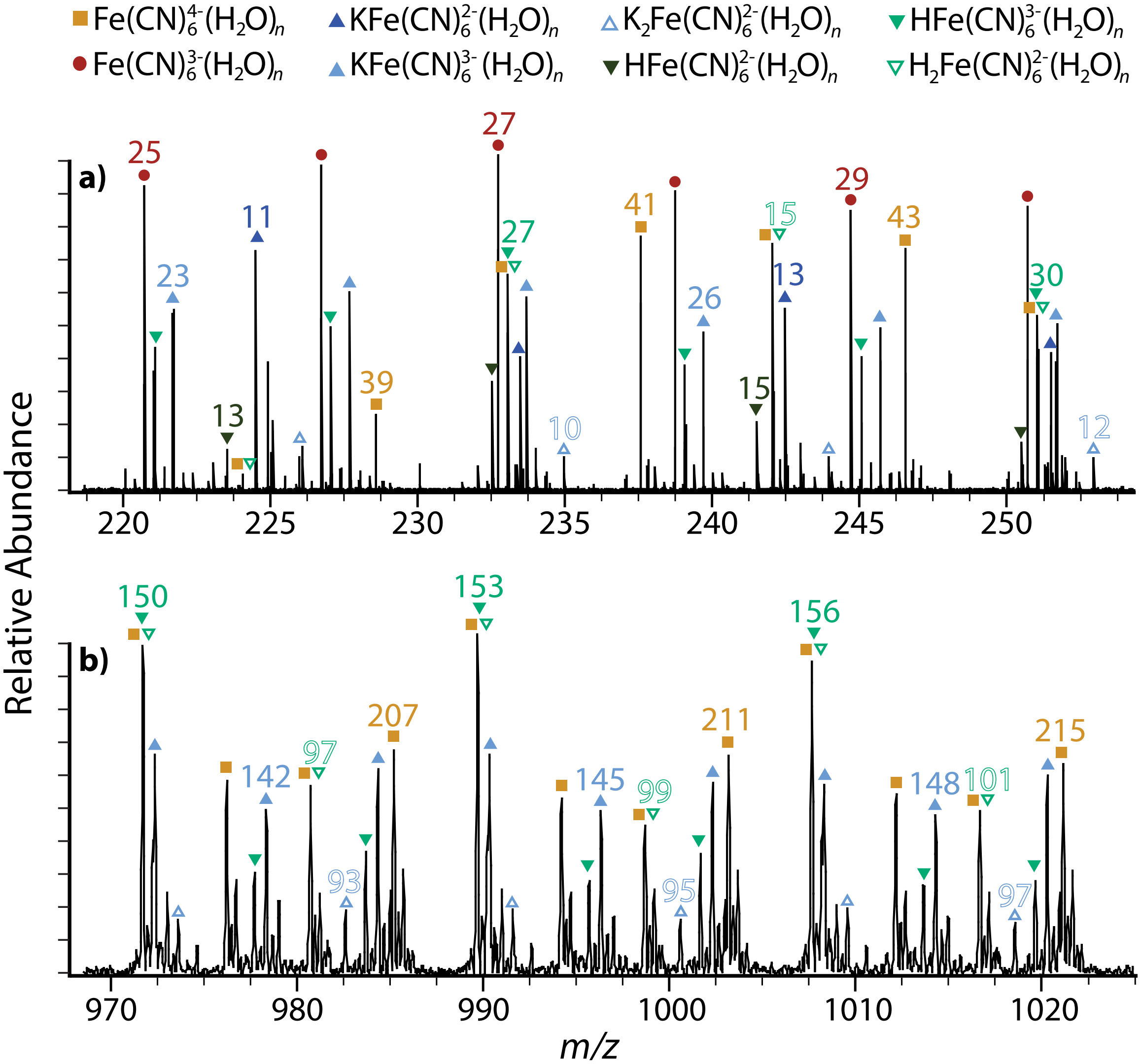

Figure A.6: Expanded regions from Figure 1 are shown to illustrate (a) the onset of ferrocyanide clusters and (b) the absence of trianion ferricyanide and associated adducts at large cluster sizes. Overlapping peaks are present for every second ferrocyanide cluster size with $H_2Fe(CN)_6^{2-}(H_2O)_n$ and every fourth ferrocyanide cluster size with $HFe(CN)_6^{3-}(H_2O)_n$.

A.0.3 Additional Figures for Chapter 5

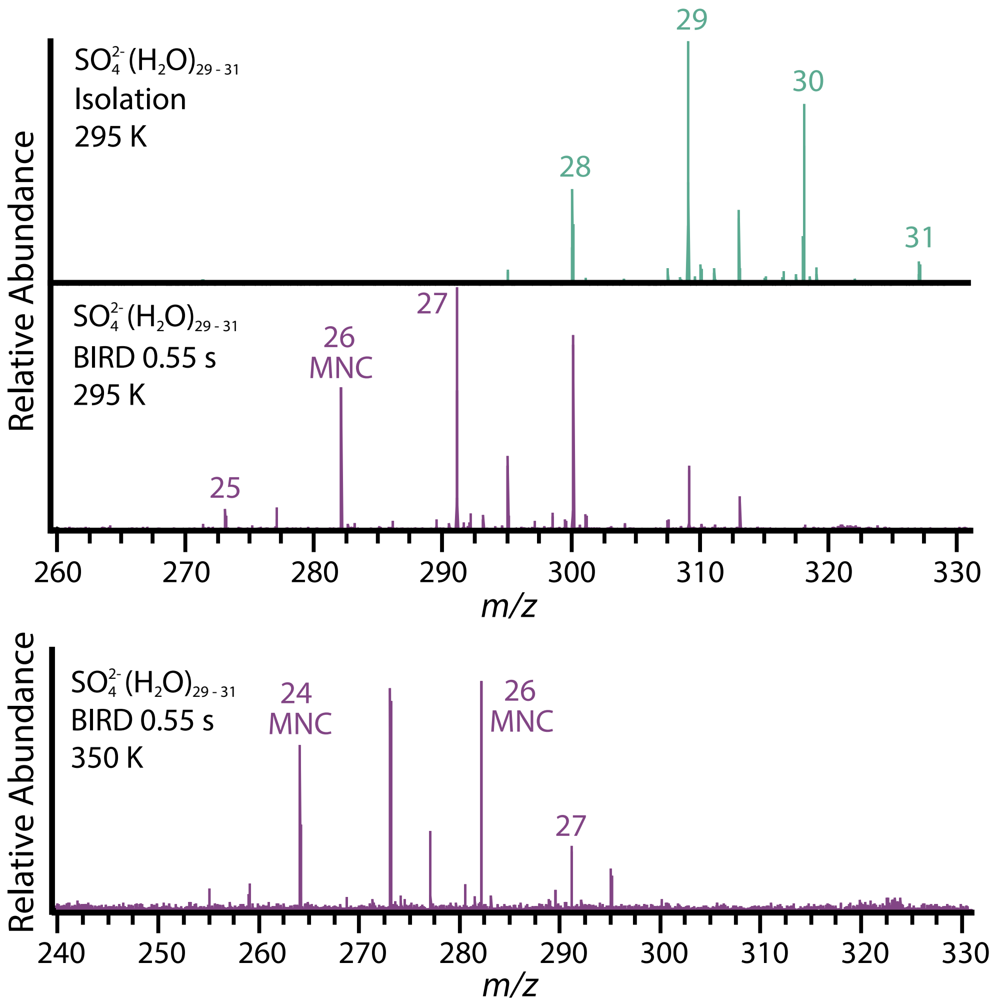

Figure A.7: Mass spectra for (a) isolation of $n_e = 30$, (b) blackbody dissociation at 295 K for 0.55 s, and (c) blackbody dissociation at 350 K for 0.55 s.

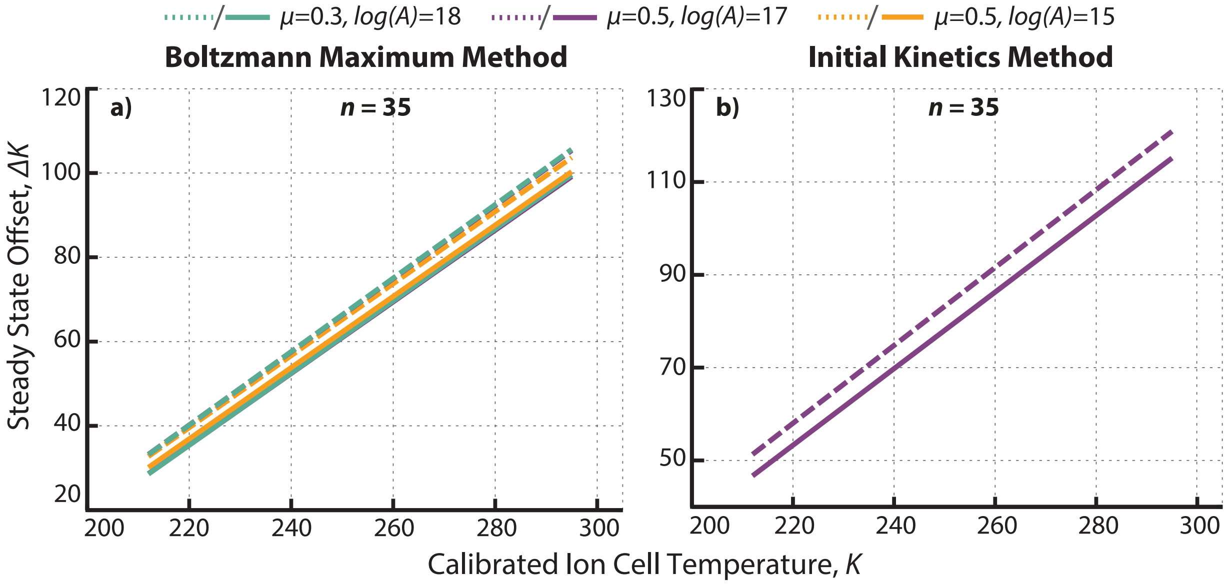

Figure A.8: Effective temperature offsets for $n_e = 35$ as a function of ion cell temperature based on steady state distributions using (a) the Boltzmann maximum and (b) initial kinetics methods.

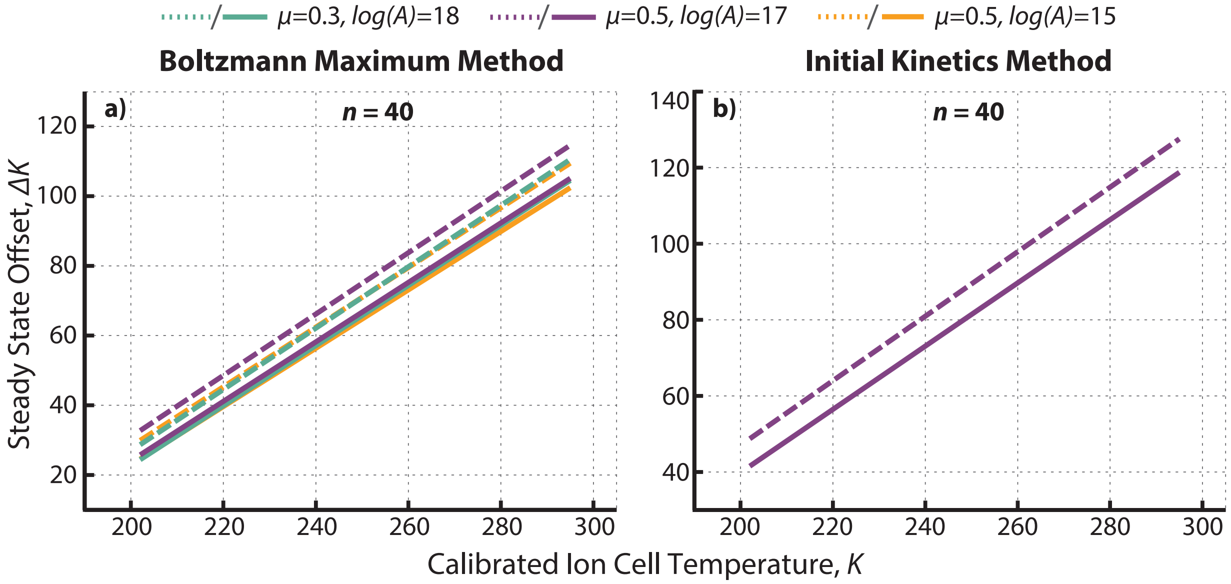

Figure A.9: Effective temperature offsets for $n_e = 40$ as a function of ion cell temperature based on steady state distributions using (a) the Boltzmann maximum and (b) initial kinetics methods.

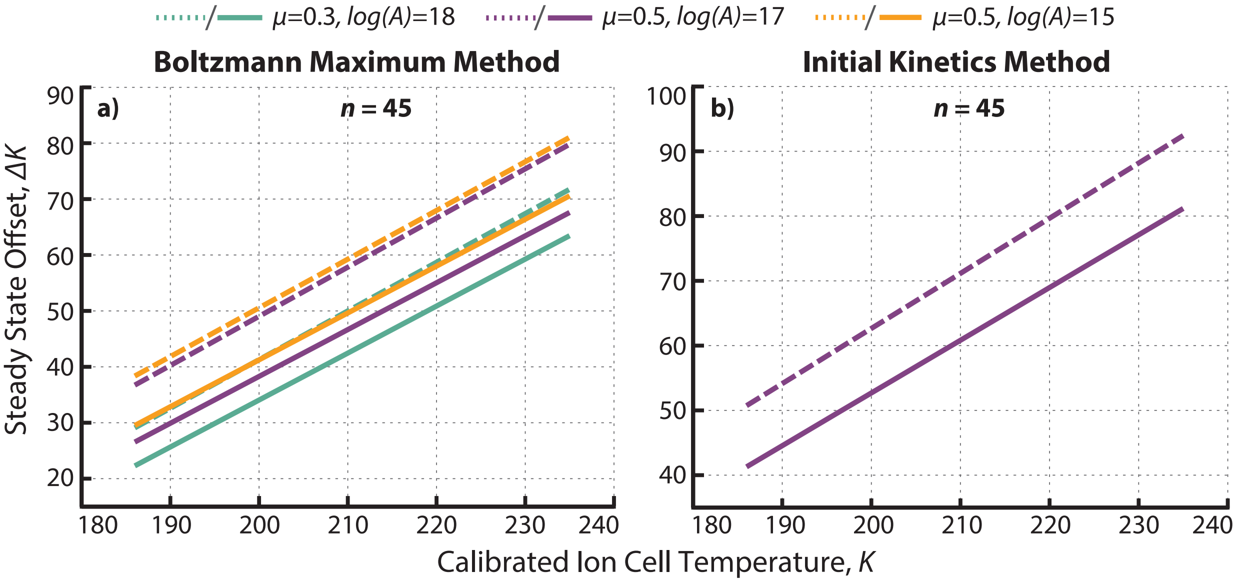

Figure A.10: Effective temperature offsets for $n_e = 45$ as a function of ion cell temperature based on steady state distributions using (a) the Boltzmann maximum and (b) initial kinetics methods.

A.0.4 Additional Figures for Chapter 6

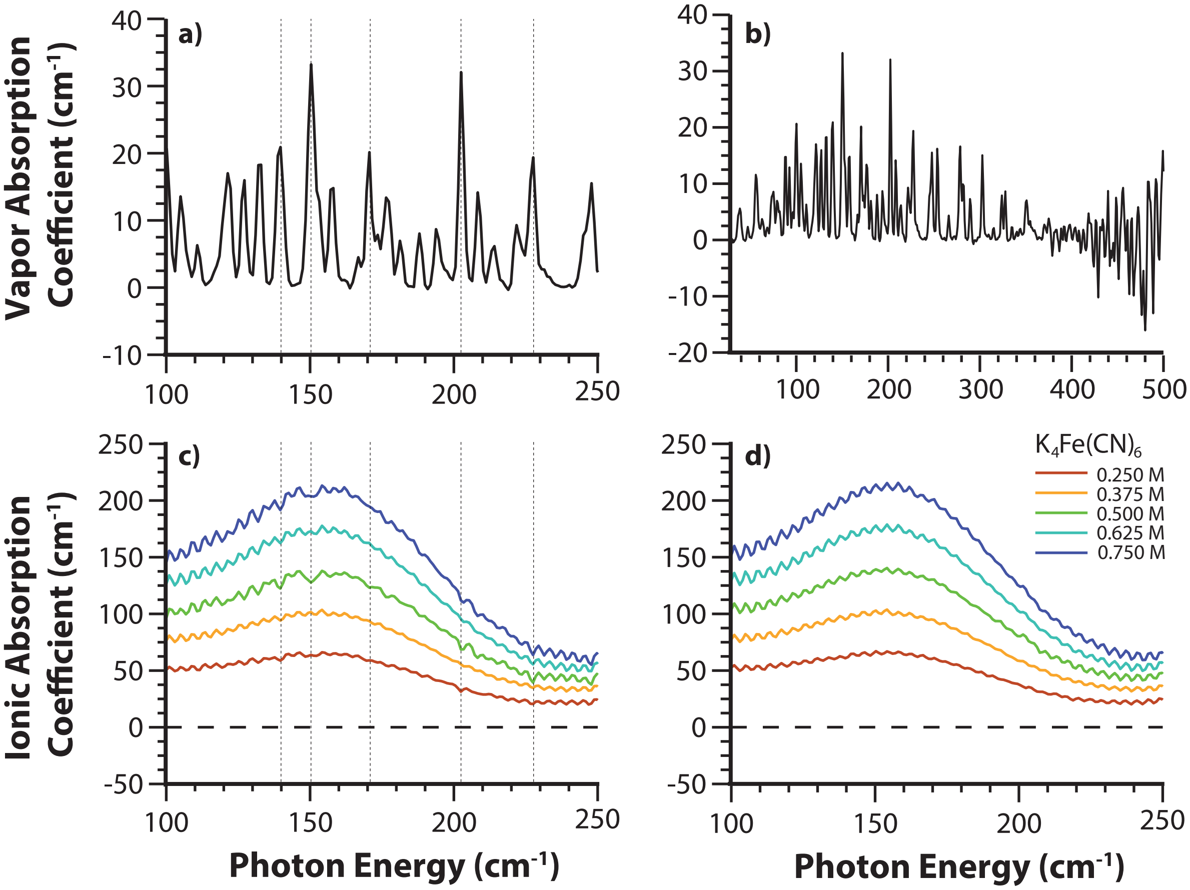

Figure A.11: Illustration of the procedure for subtraction of (a,b) the vapor absorption coefficient from (b) the effective ion absorption coefficient to produce (c) the vapor-corrected absorption coefficient for $K_4Fe(CN)_6$. Slight fluctuations in *c*, such as those at ∼150.4 and 202.5 cm^{-1}, are removed with this scaled vapor removal, which smooths the lineshape for an improved spectral fitting. Vertical dotted lines in *a* and *c* show regions of high intensity in the vapor spectrum correspond to regions with the highest fluctuation in the non-corrected absorption coefficient spectrum.

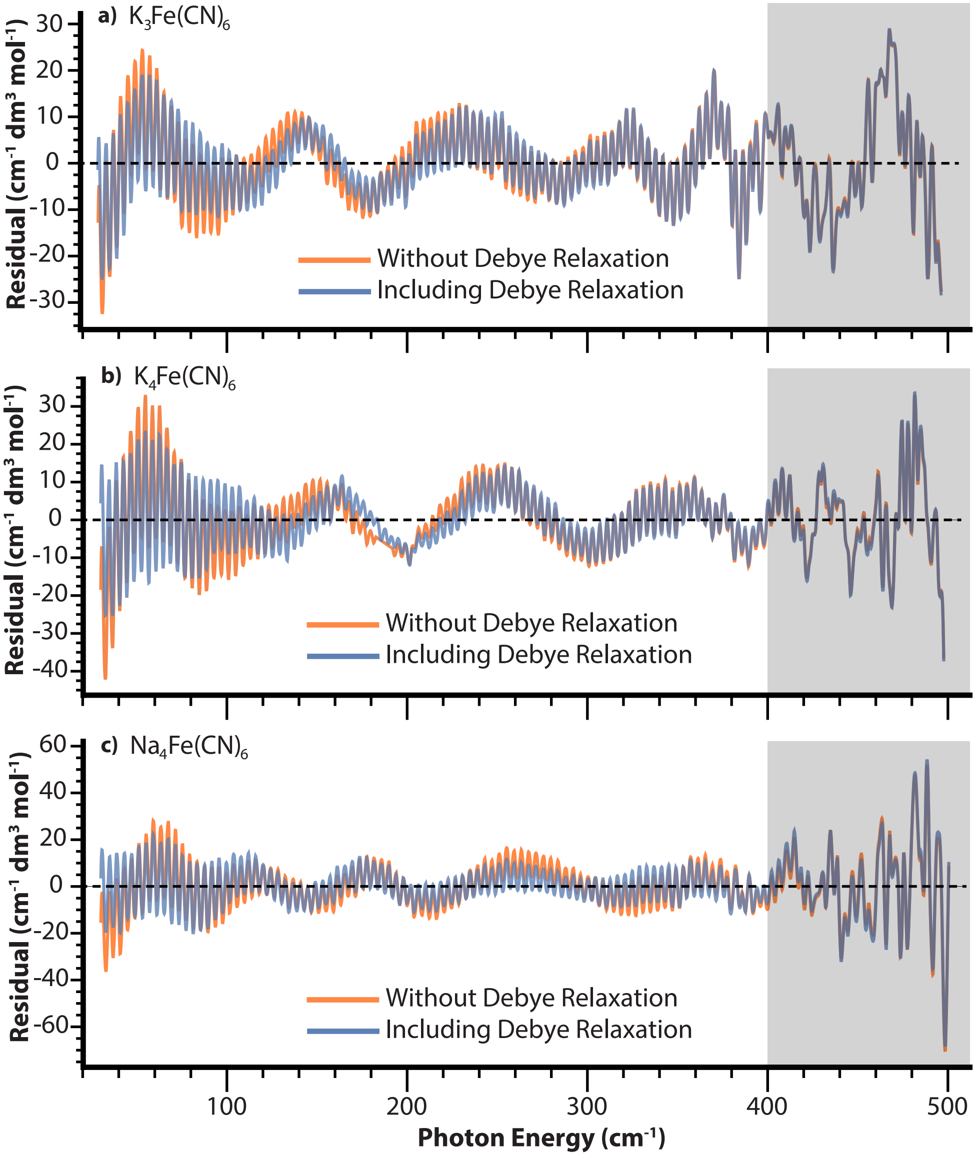

Figure A.12: Illustration of the residuals resulting from damped harmonic fits of the extinction coefficients without (orange) and with (blue) using the low-frequency Debye relaxation mode, $\varepsilon_{Debye}(\widetilde{\nu})$. This component was first manually added until the low-frequency region matched the largest residual below 400 cm^{-1} (where laser saturation begins to result in variance) for (a) $K_3Fe(CN)_6$, which resulted in an increase of ~6 water molecules for $n_{Hydration}$. Addition of $\varepsilon_{Debye}(\widetilde{\nu})$ in (b) $K_4Fe(CN)_6$ was increased until the residual matched that for a in this region. Only minor addition of $\varepsilon_{Debye}(\widetilde{\nu})$ was required for the same residual in the low-frequency region of (c) $Na_4Fe(CN)_6$ and further addition did not largely benefit the residual. The amplitude of the ion-pairing peak (a_2) is sensitive to the chosen amplitude for $\varepsilon_{Debye}(\widetilde{\nu})$, and was therefore adjusted until a_2 was ~85 % of the same peak in $K_4Fe(CN)_6$, which is consistent with this region of $\varepsilon_{ion}^{eff}(\widetilde{\nu})$ for $Na_4Fe(CN)_6$ versus $K_4Fe(CN)_6$.